Micropumps for Liquid Transport inside Biomimetic and Microfabricated Devices

Dissertation

zur Erlangung des Grades

des Doktors der Ingenieurwissenschaften

der Naturwissenschaftlich-Technische Fakultät

der Universität des Saarlandes

von

Wenming Wu

Saarbrücken

2016

Tag des Kolloquiums: 02. 12. 2016

Dekanin/Dekan: Univ.-Prof. Dr. Guido Kickelbick

Mitglieder des
Prüfungsausschusses:

Vorsitzender: Prof. Dr. Andreas Schütze
Gutachter: Prof. Dr. Andreas Manz
Prof. Dr. Georg Frey
Akademischer Mitarbeiter: Dr. Haibin Gao

Bitte unterschrieben als Einzelblatt einreichen
und in die Arbeit eingebunden, ebenfalls unterschrieben.

Eidesstattliche Versicherung

Hiermit versichere ich an Eides statt, dass ich die vorliegende Arbeit selbstständig und ohne Benutzung anderer als der angegebenen Hilfsmittel angefertigt habe. Die aus anderen Quellen oder indirekt übernommenen Daten und Konzepte sind unter Angabe der Quelle gekennzeichnet. Die Arbeit wurde bisher weder im In- noch im Ausland in gleicher oder ähnlicher Form in einem Verfahren zur Erlangung eines akademischen Grades vorgelegt.

Ort, Datum

_____

Unterschrift

_____

Table of contents

Acknowledgment

This thesis could not be successfully finished without the help of several individuals and groups across the world.

First and mostly important, I would like to express my sincere gratitude to my supervisor, Prof. Andreas Manz, who is reckoned as the leader of microfluidic academia, for hosting and supervising me. It mainly depended on so numerous discussions with him on my thesis subjects, as well as so much help from him in my daily life as an Asian student in Germany, my PhD projects can be successfully finished in time.

Also I want to sincerely thank my previous colleagues, including Prof. Nae Yoon Lee of Gachon University (Korea) and Dr. Kieu The Loan Trinh, etc. My cooperation with them also contributes partially to my thesis.

Prof. Rosanne M. Guijt (University of Tasmania, Australia), Dr. Yuliya E. Silina, and Dr. Marcus Koch (INM-Leibniz Institute for New Materials, Germany) have helped me in my projects, too. I'm grateful for their work.

I also would like to thank my colleagues, including Dr. Matthias O. Altmeyer, Dr. Jungtae Kim and Ms. Xiangping Li for giving the feedback comment of my draft thesis.

The sincere thank also goes to Prof. Leon Abelmann (Netherland), as well other colleagues of Kist Europe, for their help on me during last several years.

I gratefully acknowledge the Chinese Ministry of Education for awarding me "the scholarship for best level Chinese overseas PhD student" in 24. 02. 2016, and committees of CBMS and MicroTAS for awarding me "CBMS Student/Young Researcher Grant" in 02. 10. 2015.

I want to give my grateful thank to my wife Jinhua Yin, as well as my parents for their constant support and encourage on me.

Abbreviations

AFM	Atomic force microscopy
µTAS	micro Total Analysis System
POC	Point-Of-Care
PDMS	polydimethylsiloxane
XPS	X-ray photoelectron spectroscopy
PMMA	polymethylmethacrylate
PC	polycarbonate
PVC	polyvinylchloride
PCR	polymerase chain reaction
2.5D	2.5-dimensional
3D	3-dimensional
HS-GC-MS	Headspace gas chromatography mass spectrometry
MEMS	Microelectromechanical Systems
LOC	lab-on-a-chip
CNC	Computerized Numerical Control

Abstract

The micropump is one of the most important parts of micro Total Analysis Systems. In this thesis, three types of pumps, (syringe pump, capillary pump and diffusion pump) are utilized for microfluidic transport inside biomimetic and microfabricated devices. It's confirmed that syringe pump can be efficient access in fluidic transport for wide range of microdevices, such as the 3D helical silicone tubing microreactor containing smooth channel surface, the Y-structured microchannel containing grooved-shaped sidewall, and PDMS/Polymer microchips microfabricated from photolithography, qualified for accurate flow rate control, microdroplet formation and multi-phage flow, anticorrosive assay and leakage test, etc. In addition, another two types of self-activated micropumps: the capillary micropump and the diffusion micropump are also applied for liquid transport through different microdevices in this thesis. It's found here that, the capillary micropump can be efficient approach for self-activated liquid transport inside 2.5D microchip for potential Point of Care applications, while the diffusion micropump can produce much more homogeneous flow than previously reported. The microfluidic transport properties of the diffusion micropump in biomimetic microdevice and 3D helix tubing microdevice is also characterized. Compared with the mainstream of traditional micropumps, I find diffusion micropump displays unique superiority in integrating a lot of advantages altogether, including much smaller size, dramatically simple structure, free of external power consumption, simple fabricating procedure, strong micro fluidic transportation ability, homogeneous flowing velocity over long distance, resistant to adverse external condition like high temperature, easiness of microdevice integration and much lower price.

Abstrakt

Die Mikropumpe ist eines der wichtigsten Komponenten eines miniaturisierten totalen Analysensystems. In dieser Arbeit werden drei Arten von Pumpen, Spritzenpumpe, Kapillarität und Diffusionspumpe beschrieben und angewandt für mikrofluidischen Transport in biomimetischen und mikrofabrizierten Strukturen. Es wird gezeigt, dass Spritzenpumpen für verschiedenartige mikrofluidische Chips eingesetzt werden können, zum Beispiel für den 3-dimensionalen verschlungenen Reaktor aus Silikonschlauch, für den Y-förmigen Reaktor mit steilen Seitenwänden, und photolithographischen Mikrochips aus PDMS-Polymer, mit kontrolliertem Durchfluss, für die Formung von Tröpfchen und für Mehrphasen-Fluss, für Antikorrosions-Test und Leck-Test, etc. Ausserdem werden in dieser Dissertation zwei weitere Typen von autonomen Pumpen eingesetzt: die Kapillarität und die Diffusions-Mikropumpe. Es stellte sich heraus, dass Pumpen durch Kapillarkraft in 2.5-dimesnsionalen Mikrochips für zukünftige klinische Anwendungen verwendet werden können, während die Diffusionspumpe einen weit gleichmäßigeren Fluss erzielt als bisher beschrieben. Mikrofluidische Transporteigenschaften der Diffusionspumpe in biomimetischen Strukturen und in 3-dimensionalen verschlungenen Strukturen werden beschrieben. Ich denke, im Vergleich zu den meisten herkömmlichen Mikropumpen zeigt die Diffusionspumpe klare Vorteile, sie ist klein, einfach gebaut, benötigt keine externe Stromversorgung, ist einfach herzustellen, funktioniert einwandfrei über längere Strecken, ist pulsationsfrei, ist unabhängig von äußeren Einflüssen wie hohe Temperatur, kann einfach integriert werden und zu niedrigerem Preis.

摘要

微型泵是微型全分析系统最重要的组成部分之一。基于微机电系统（MEMS）的第一个的微型泵在 20 世纪 80 年代被提出，之后，不同致动机制的十几不同种类型的微型泵已被开发出来。在本论文中，三种微泵: 注射泵，毛细管泵和气体扩散泵被应用于包括仿生学芯片在内的不同类型的微加工设备内的微流体输送。本文证实了注射泵可以在广泛的微型器件实现流体高效输送，例如，在光滑内表面微通道的 3D 螺旋硅胶管微反应器, 开槽形内侧壁的 Y 型结构微通道，以及通过光刻法制备的 PDMS /聚合物微芯片中实现精确的流量控制，微液滴和多相微流体的形成，防腐试验和泄漏试验等。但注射器微型泵难以被集成到微型器件，并且需要消耗外部能量。作为补充，两个自发微型泵：毛细管微型泵和气体扩散微型泵也在本文中被应用于不同的微器件的液体输送。本文发现，毛细管微泵可以在 2.5D 的芯片内部实现流速随时间减慢的自发的输送液体，为医疗点位检测提供了潜在解决途径；而气体扩散微型泵可以产生较为均匀的流动，且稳定性高于先前在 2D 聚合物型微芯片中的报道。除此之外，本文还将气体扩散微型泵应用于仿生学微型设备和三维螺旋管道微设备中的微流体输运。与传统的微型泵相比，我们发现扩散微泵集众多优势于一身：包括极小的体积，结构简单，无外功耗，无复杂制造工艺，长距离的均匀流速，在高温下的卓越输送能力， 以及较低的成本。

1 Introduction

Micropumps play a crucial role in microfluidic transportation systems and have been the interests of wide range research projects during last 20 years. In the 1980s, Jan Smits and Harald Van Lintel developed the first genuine MEMS micropumps driving fluid in the micro scale systems through piezoelectrics.[1,2] After that, lots of micropumps have been developed based on different actuation mechanisms. A summary of traditional micropumps developed during last twenty years will be firstly clarified here. Traditional micropumps can be classified into two groups--- "mechanical micropumps" and "nonmechanical micropumps".

1.1 Mechanical micropumps (State of the art)

The first so-called "mechanical micropumps" use the oscillatory or rotational movement of mechanical parts to displace fluidic or gas. Mechanical pumps can be further subdivided into several categories. Syringe pump is the mostly widely used mechanical pump in "lab on chip" systems nowadays. It generally consists of a piston to provide smooth flow.[3-5] Rotary pump[6] and peristaltic pump[7] are another two forms of mechanical pumps which sometimes may replace syringe pump for transporting microfluidic. Besides these commercially available pumps, some other mechanical pumps have also been developed over the last twenty years. Piezoelectric micropumps[8-11] use piezoelectric actuation to drive the flowing of microfluidic. During last several decades, even if extensive micropump research has been done on piezo-driven micropumps with varying valve types, geometries and fabrication technologies, all piezoelectric actuators are employed in a similar manner.[12] Through the significant shape changes of certain piezoelectric materials like lead zirconate titanate (PZT), piezoelectric pumping effect is realized. When the PZT is deflected away from the channel, its inner pressure becomes lower and thus fluid is drawn into it. Conversely, when the PZT disk is bent into the channel, its inner pressure becomes higher and thus pushes fluid out.

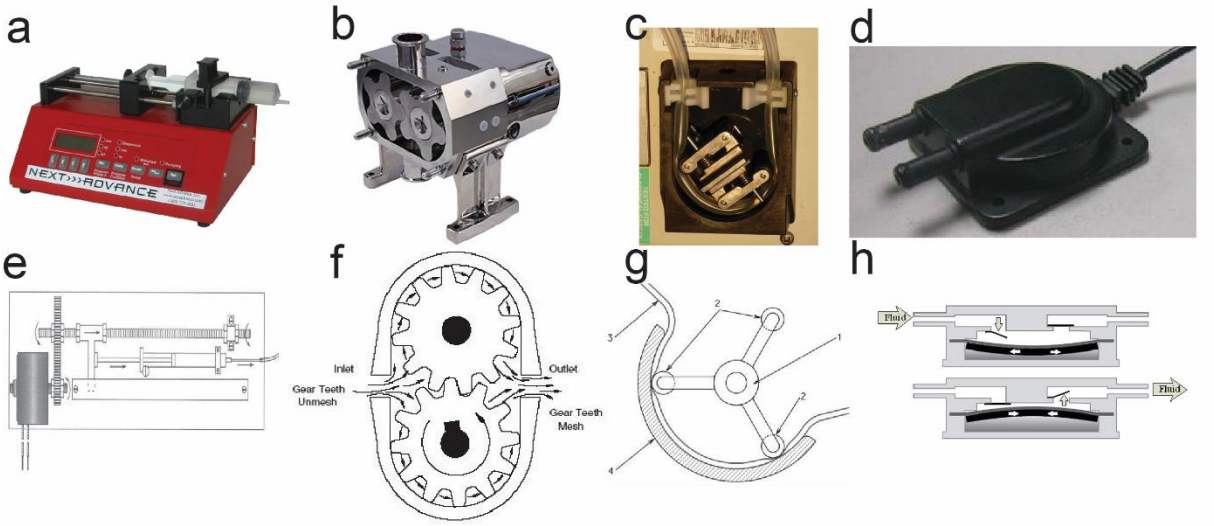

Figure. 1 Mechanical micropumps. (a) - （d） Real photos of syringe pump, rotary pump, peristaltic pump and piezoelectric pump. (e) - （h） Working mechanisms of syringe pump, rotary pump, peristaltic pump and piezoelectric pump.

Besides aforementioned mechanical pumps, the pneumatic micropump is another kind of micropump which has been intensively studied recently.[13-16] Pneumatic micropump is generally initiated and ceased based on sequentially vibrating elastic microvalves mainly consisted of thin PDMS membrane, and can be applied to both semicircular and rectangular channels. In contrast with other off-chip mechanical pumps, the pneumatic micropump can be easily integrated into the microdevice, and thus, has aroused big interest ever since it's developed in 2000. As shown in Figure 2, fluid volume displacement in the microchannel is produced, through actuating these microvalves in series. Similarly, thermopneumatic micropumps also relies in membrane motion to drive microfluidic, but a thermal expansion mechanism is realized through the direct heating of secondary working fluid or air in a separate chamber to cause an expansion pressure of gas.[29-31] The microdevice integrating pneumatic or thermopneumatic pump is 3-layer, containing fluidic channel and air channel.

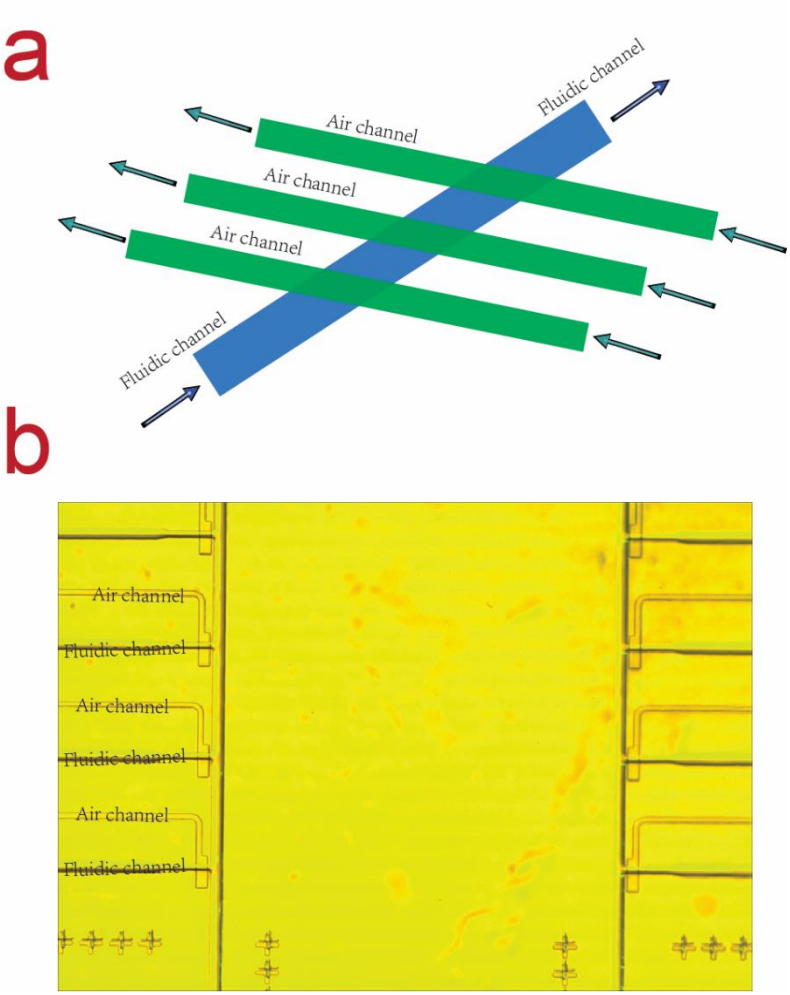

Figure. 2 a) Schematic mechanism of pneumatic pump automated by sequential open and close of microvalve (redrawn from "Science, 2000, 288, 113"). b) The image of 3-layer microdevice, with fluidic channel and air channel.

1.2 Nonmechanical micropumps

The second so-called "nonmechanical micropumps" transport fluid without any moving components. A variety of interaction phenomenon has been utilized to generate motivation pressure of the flow.

1.2.1 External-power driven pump (State of the art)

Electroosmotic micropumps use the electroosmotic flow (EOF) [17,18] to obtain bulk motion of electrolytic liquid immersing porous material, capillary, membrane or microchannel with charged walls. When a DC electric potential is applied between

the electrodes, a high force will act on the electrical ions in the double electric layer nearby microchannel walls, causing the movement of electrolyte fluid. So the prerequisite for the electroosmotic pump is the presence of immobilized surface charges in contact with liquid. Electrokinetic micropumps[19-22] and electrophoresis pumps[23,24] use an electric field to move charged particles or molecules in microchannels. Similar to the electroosmosis pump, the prerequisite for the electrokinetic micropump and electrophoresis pump is the electronic constituents inside the liquid, but this time the electronic constituents turn to the charged particles or macromolecules. In addition to its wide application in capillary electrophoresis, electrophoresis pump has been widely applied for DNA separation through agarose gel to determine fragment size and intensity.

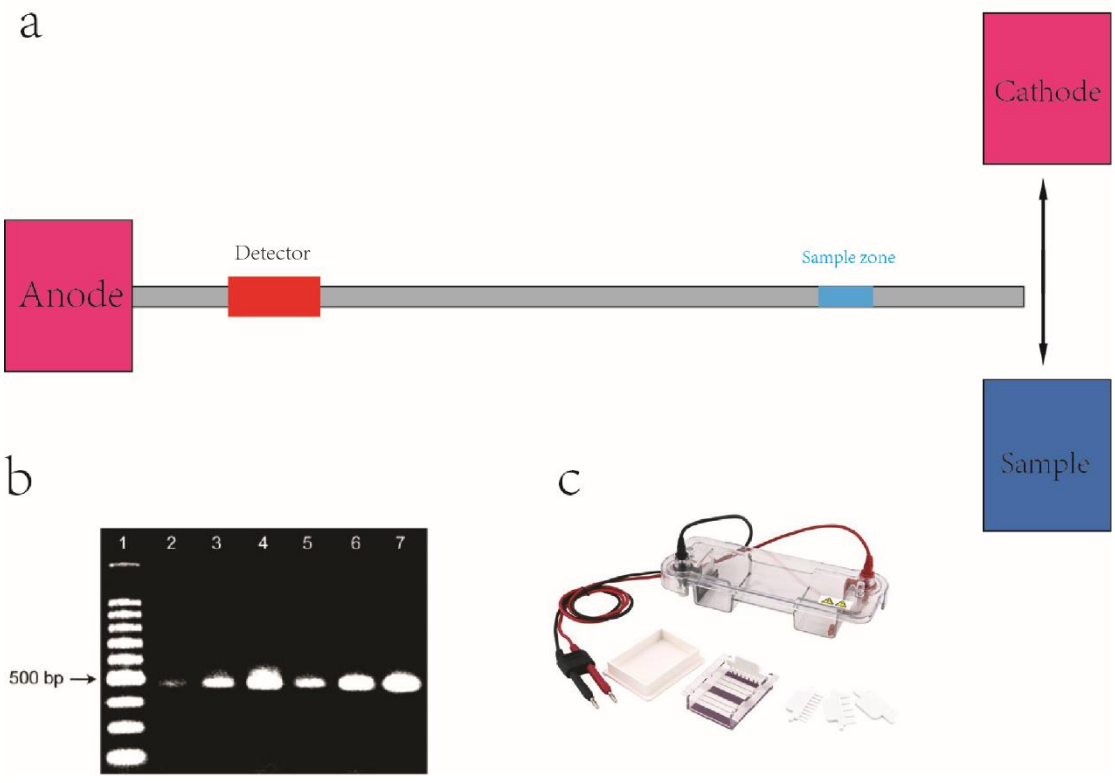

Figure. 3 (a) Schematic diagram of capillary electrophoresis. (b) Agarose Electrophoresis can be applied to separate DNA fragments depending on size difference. Lane 1 shows DNA bands for 100 bp DNA size marker. Lanes 2–7 show six amplification results obtained using plasmid vector, pGEM-3Zf(+), as templates. Reprinted from (Wu et al., Analyst, 2011, 136, 2287) (c) Real photo of electrophoresis device.

Magnetohydrodynamic (MHD) micropumps use Lorentz force to automate the flow of electrolytic liquid or motion of charged molecules within the channel.[25-28] In the presence of a perpendicular magnetic field oriented in an angle of 90° to current direction and microchannel axis, the Lorentz force is produced when an electric current is applied across conducting solution in channel and act onto the ionic current of the aqueous solution to induce a fluid flow.

The Lorentz force on charged molecule, particle or fluidic plug, can be calculated to be:

$$F_l = qvB$$

Wherein, F_l is Lorentz force, B is the magnetic field, q and v are the electric quantity and velocity of charged molecule, particle or fluidic plug.

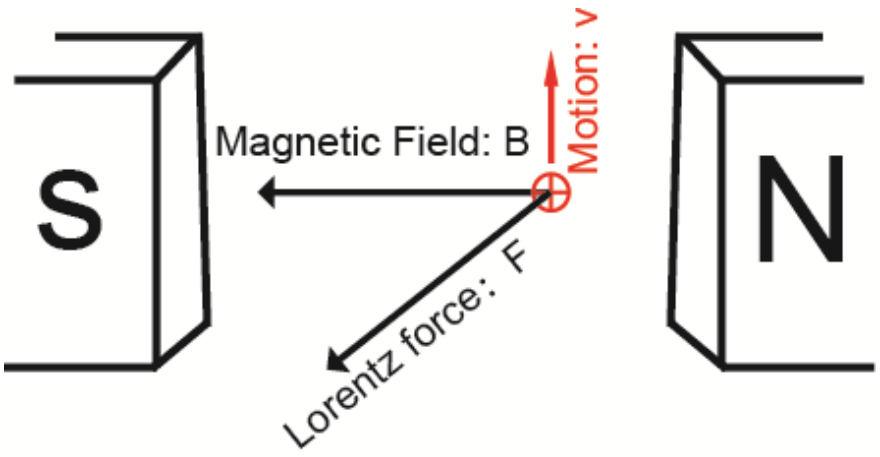

Figure. 4 Lorentz force on the charged particle or molecule.

Different from above several micropumps which are directly initiated by electric field, evaporation micropumps use another driving force as the actuation power of microfluidic in a microchannel. Through electrochemically generated bubbles inside the primary working fluid as an actuation force, electrolyzation can be applied to produce expansion pressure. Micropumps using this mechanism sometimes are referred as the 'bubble' micropumps or 'electrochemical' micropumps.[32-35] In addition, magnetic micropumps use magnetic force to simply

and quickly automate ferrofluidicliquids.[36,37] An permanent magnetic or an electromagnet can be used to produce the magnetic field on the microdevice. Through current change of the electromagnet, the magnetic liquids or particles will respond to the variable electromagnetic forces and move correspondingly. Acoustic micropump is another form of nonmechanical micropumps developed just about ten years ago.[38,39] It uses external acoustic field to generate and excite the bubbles inside the microdevice. Based on the growth and collapse of bubbles, such acoustic actuation allows for directed pumping of fluid in simple microchannels without any mechanical moving parts. All above micropumps are initiated through consumption of external power.

1.2.2 Traditional self–activated pumps (State of the art)

In order to get rid of external power for fluidic transport, some other micropumps have been developed, too. Capillary micropump is one typical representative of self-activated micropumps. It utilizes capillary force to spontaneously transport small volume of fluid that's in contact with microchannel surface.[40-42]

Capillary tension effect can be represented by the following equation,

$$h = 2\gamma\, cos\theta/\rho g r$$

wherein h is liquid height inside vertical capillary tube, γ is surface tension, θ is liquid contact angle, ρ is liquid density, g is gravity, r is radius of capillary tube.

As shown in Figure 5, for the three capillary tubes inserted inside the liquid, the liquid heights are is different. Because $r_1 < r_2 < r_3$, the liquid height in three tubes are $h_3 < h_2 < h_1$, depending on above equation.

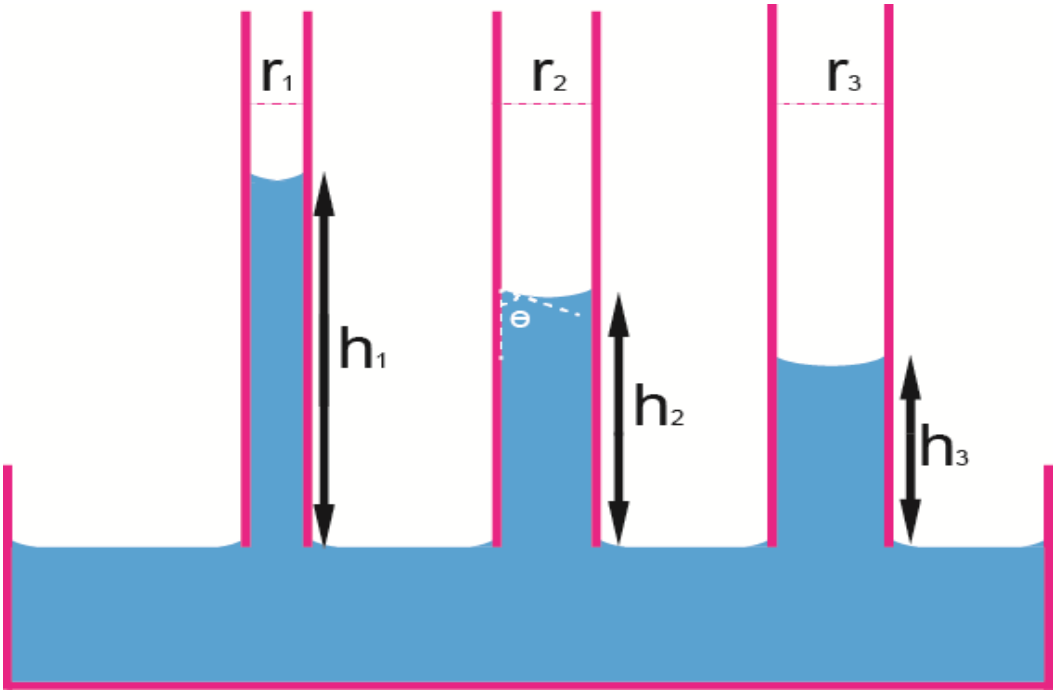

Figure. 5 Schematic diagram of capillary tension effect.

Above phenomenon explains the mechanism of capillary pump. The surface tension results in pressure difference across the liquid-air interface, which is the automation force of capillary micropump. Through the interplay between the liquid's surface tension and the microchannel surface, the spontaneous flow is maintained in the direction that minimizes the free energies between the fluid and solid interface. The capillary pressure *Pc* can be calculated by the following equation:

$$Pc = 2\gamma\, cos\theta / r$$

Depending on this equation, we can see the capillary pressure increases as channel surface tension increases.

Several years ago, another kind of sucking effect is reported simply by putting the PDMS microfluidic chip in one vacuumized container. Then spontaneous flow inside PDMS capillary channel is easily caused and applied in one commercial significant micro Total Analysis Systems (μTAS) to separate the plasma from the blood.[43] "Paper-based microfluidics" can be another alternative capillary-pumping method of traditional micropumps for transporting liquids without the existence

of external forces, and thus has attracted more and more interests recent years for some commercial or clinic application purposes.[44]

In addition, hydrostatic pump has also been introduced by utilizing hydrostatic pressure to automate the liquid flow. For such pump, a vertical tube is connected to the microchannel, which can produce hydrostatic pressure on the liquid. Hydrostatic pressure can be represented by the following equation:

$$P_h = \rho g h$$

Wherein, P_h is hydrostatic pressure, ρ is liquid density, g is gravity, h is liquid height inside the vertical tube.

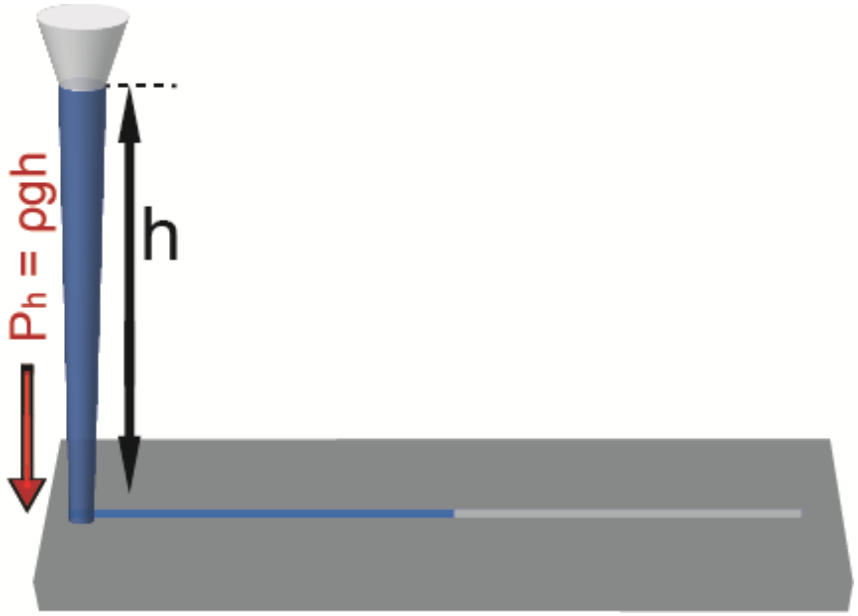

Figure. 6 Schematic diagram of hydrostatic pump.

As shown in Figure 6, a controllable pressure can be produced on the microchannel, by controlling liquid intensity and height. Despite the dramatic achievements in developing different types of micropumps for fluidic transport, the commercial significance of traditional micropumps has become one main bottleneck of this whole area.[45,46] In 2003, commercial availability of micropump was announced rely on piezoelectric actuation and incorporating passive check valves.[47]

1.2. 3 Diffusion pump for single channel

In previous works,[48,49] a new nontraditional micropump (called as "diffusion micropump") was raised and studied, without any fabricating step or any laborious assembly operation. This new kind of micropump doesn't belong to the framework of any traditional micropumps as illustrated in previous dialogues.

Figure. 7 shows schematic illustrations for the sample injection mechanism proposed in "diffusion micropump". Briefly, air pressure throughout the entire microfluidic conduit is the same before introducing sample plug into the microdevice. After the sample introduction to the inlet tube of microchip, the sample plug separates the fluidic conduit into two parts, wherein larger amounts of air-molecules permeate through anterior part of sample plug which is the gas-permeable surface of fluidic conduit, than the posterior part of sample plug which is gas-impermeable plastic syringe, and thus, causes a relatively higher internal pressure in the posterior end than the anterior part of sample plug, automating for the sample movement.

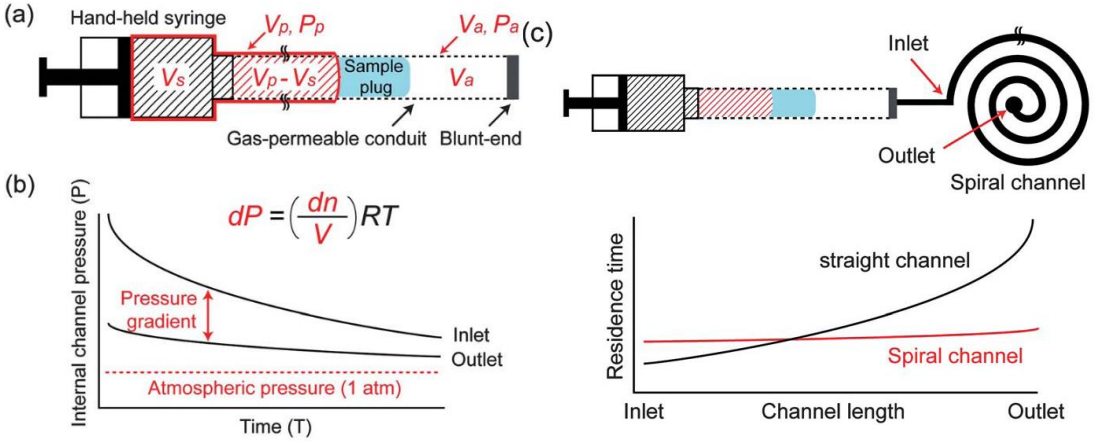

Figure. 7 (a) A schematic illustration demonstrating a new concept for sample injection employing a highly gas-permeable fluidic conduit coupled with a hand-held plastic syringe filled with compressed air. Vs, Vp, and Va represent the volumes of air contained in syringe, in the posterior end of the sample plug, and the anterior end of the sample plug, respectively. Pp and Pa represent the air pressures in the posterior and anterior ends of the sample plug, respectively. The equation, dP = (dn/V) RT, is derived from the ideal gas law, PV = nRT. (b) A schematic graph demonstrating a gradual reduction in the pressure gradient formed by the pressure difference in the inlet and the outlet of the fluidic conduit.

(c) A schematic illustration showing a spiral microchannel coupled with a hand-held plastic syringe and a schematic graph comparing the sample residence time inside a straight and spiral channels. Taken from (Wu *et al.,* Analyst, 2012, 137, 983).

Air diffusion from inside the microdevice to ambient environment automate the liquid flow. As a result, if the microdevice is placed inside water bath, more and air bubbles can be seen on the device surface as the time passes, as shown in Figure 8.

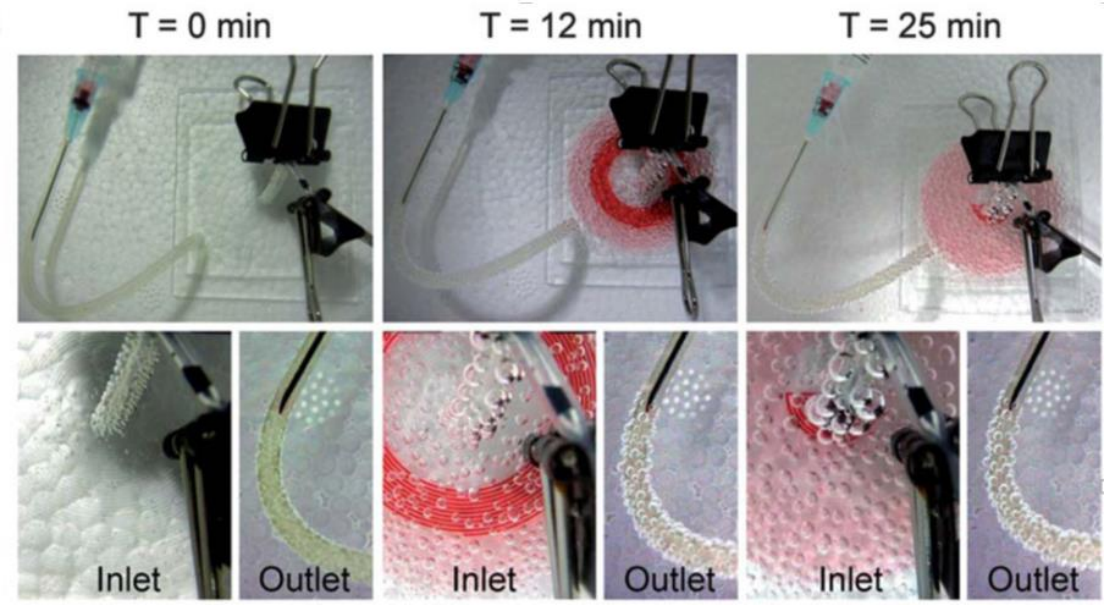

Figure. 8 Series of photos demonstrating the generation of air bubbles taking place simultaneously with the flow of the red ink plug inside a spiral microchannel at 0, 12, and 25 min after the pressurization of the air inside the fluidic conduit. Taken from (Wu *et al.,* Analyst, 2012, 137, 983).

In order to reveal its superiority, the diffusion micropump is also utilized for micro continuous PCR. The conditions of micro continuous PCR is more complicated than most other chemical or biological process inside microfluidic chip. The complicated and extreme reaction conditions of micro continuous PCR, include high denaturing temperature of 95 degrees which requires a strong micropump resistant to high temperature overcoming bubbles, total sample transporting channel length of over 2 meters which require a powerful micropump with persistent motivating ability, and homogeneous retention time for each amplification cycle which requires one stable micropumping. For example, it's impossible to inject PCR

sample into PDMS-Glass microchannel just by syringe pump. As shown in Figure 9 d ~ e, a lot of air bubbles come out if syringe pump is applied for ink transport. In contrast, the air bubbles can be eliminated if the mineral oil is utilized to sandwich either the red ink (Figure 9 d ~ e) or the PCR sample (Figure 9 a ~ c).

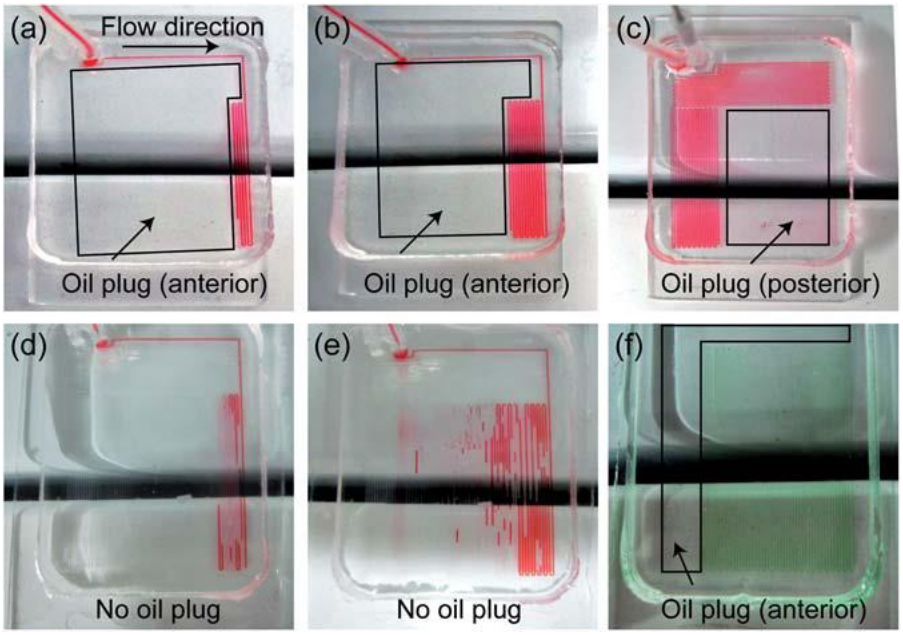

Figure. 9 Bubble elimination when paraffin oil plugs are employed both in the anterior and posterior of the ink plug. (d–e) Bubble generation when paraffin oil plugs are not employed. (f) Bubble elimination when real sample was encapsulated with paraffin oil plugs both in the anterior and posterior of the sample. Green-colored buffer was utilized for visual effect.

But if diffusion pump is applied for sample transport through PDMS-Glass device, as shown in Figure 10, there are very little air bubbles coming out without the assistance of mineral oil. It verifies the diffusion micropump can provides not only stable flow over long distance but also steady flow endurable to high temperature.

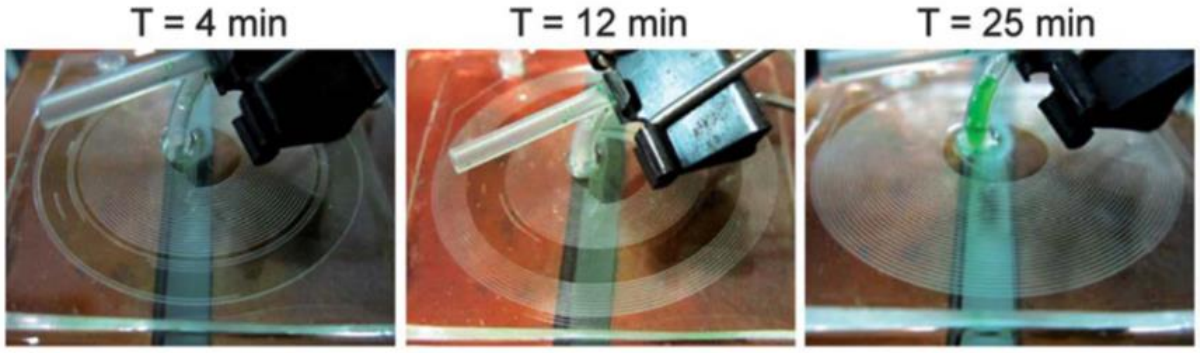

Figure. 10 Flow of the real sample solution inside a spiral microchannel in a time dependent manner under a heated condition, measured at 4, 12, and 25 min.

Without external energy consumption or complicated constituent components, the diffusion micropump makes the overall size much smaller than mechanical pumps like syringe pump. Figure 11 compares the sizes of the overall systems needed to operate the microdevice by diffusion micropump (a) and syringe pump (b) for performing on-chip flow-through PCRs. The diffusion micropump system requires neither tailor-made heating blocks nor expensive syringe pumps, but simply requires a single hot plate and disposable plastic syringes, with simplified operation and facile reactions.

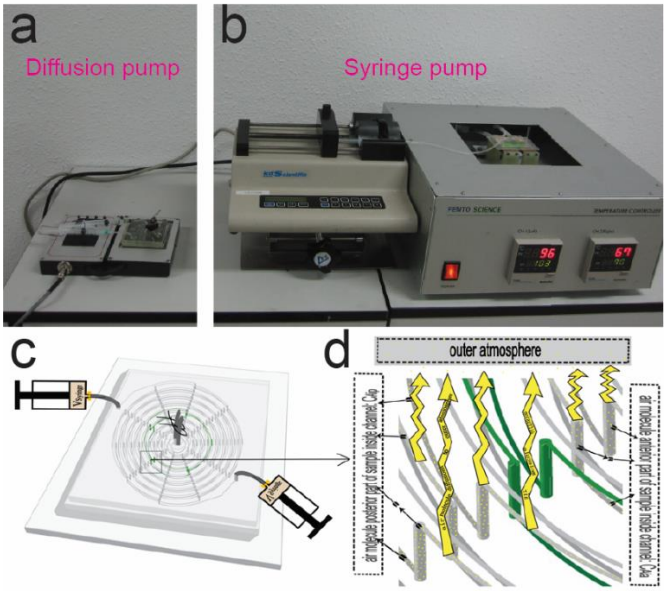

Figure. 11 Overall systems needed to operate PDMS microdevices proposed by (a) diffusion pump and (b) syringe pump. The automation mechanism of two-layer microdevice (c) is indicated in (d). Taken from (Wu et al., Sensors and Actuators B: Chemical, 2013, 181, 756) with modification.

The successful result of diffusion micropump in realizing PCR displays its advantages on enduring high temperature, durable liquid driving strength and high flowing stability. In contrast with aforementioned micropumps, the diffusion pump displays a lot of advantages including much smaller size, free of external energy driven, simple fabricating procedure, strong micro fluidic transportation

ability, homogeneous flowing velocity over long distance, resistant to adverse external condition like high temperature, easiness of μTAS integration and much lower price.

1.2. 4 Diffusion pump for bio-inspired microvasculature (this work)

In previous works[48,49, 40~44] the self-powered autonomous flow is applied to simple topological microsystem: one-directional segmented-linear microchannel connecting only one inlet and one outlet.

In contrast, leaf inspired microsystem is consisted of very complicated microvascular networks interconnecting multiple inlets and outlets, which has totally different microstructural topology with aforementioned microsystems. Noticeably, water transport in real leaves totally depends on self-activated micropumping without power consumption, similar to self-powered micropumps as I introduced before. Inspired by these post, I innovate the biomimetic PDMS leaves for self-powered autonomous flow in PDMS leaves, which can also prove the successful manufacture of microchannels from real leaf without leakage.

As clarified by Figure 12a, "transpiration theory"[50,51] is the most widely accepted theory to explain self-powered water-pumping inside plants. Transpiration is the loss of water from a plant in the form of vapor. This theory believe that vapor-molecules diffuse from inside the leaves into outside atmosphere through stomata, reducing hydrodynamic potential in leaf. In contrast, few stomata are located in stipe, and thus, vapor molecule's diffusion in stipe is negligible as compared with leaf. As a result, hydrodynamic potential can be considered as constant in stipe. Because vapor diffusion only reduces hydrodynamic potential in leaf but doesn't decrease hydrodynamic potential in stipe, a pressure gradient forms between stipe and leaf, and pushes liquid autonomously flowing from stipe to leaf after vapor-molecules' diffusion. Similarly, the air-molecules' diffusion only occurs in PDMS leaves and negligible in syringe.

Specialized to the self-powered flow inside PDMS leaves, both inlet tube and disposable syringe can be considered as gas-impermeable because syringe material is PP and impermeable to air molecules, but PDMS leaves are considered to be gas-permeable. As a result, gas permeability in the posterior part of the sample plug could be considered negligible, while air molecules could be rendered to only diffuse from two surfaces of PDMS leaves to the atmosphere. Due to the permeability of PDMS leaves, the pressurized air captured inside biomimetic microvasculature diffused through the artificial leaves, causing decreased pressure and continuous flow towards biomimetic micro-vascular network from syringe. The ideal gas law is represented as follows:

$$PV=nRT$$

wherein P is the pressure of syringe, V is the volume, n is the amounts air molecules inside syringe, T is the Kelvin temperature, and R is the gas constant.

Because syringe is impermeable to air molecules, n can be reckoned to maintain constant in above equation. Because syringe volume was several hundred times of the pipette combined with microvascular networks, air volume V inside gas-tight syringe could also be considered constant. Besides, R and T are also constant in above equation, so P is concluded to be constant during ink filling to PDMS leaves. After the red ink flowed through the inlet tube and reaches the biomimetic networks of the PDMS leaves, pressure of the posterior part is maintained (by pushing the piston from the 4.3 mL mark to the 3.2 mL mark on the syringe) to be 2.57 atm, but pressure of the anterior part keeps decreasing due to continuous air-molecules' diffusion. As a result, red ink can finally fill in whole microvascular networks of PDMS leaves, as shown in Figure 12b. From above discussion, I can see air pressure throughout the entire PDMS leaves was the same before sample plug flowing into the inlet tube. After sample is introduced to the inlet tube, the sample plug separated the fluidic conduit into two parts, wherein air molecules only permeated through anterior part (PDMS leaves) but not at the posterior part (syringe), and thus, causes lower pressure at the anterior part than posterior part.

It can be reckoned that only hydrodynamic potential of PDMS leaves reduces, and hydrodynamic potential of syringe doesn't decrease, similar to real leaf.

Based in aforementioned discussion, it can be seen that even if self-powered flow through real leaf and PDMS leaf differ with specialized type of diffusional gas-molecules (it is air-molecules' diffusion in PDMS leaf, but vapor-molecules' diffusion in real leaf), they share the same gas-molecules' diffusion (from inside PDMS/real leaf into atmosphere) mediated pumping mechanism on same microvascular geometry. Mostly important, the liquid flux in both cases can be represented by the following equation:

$$Q = V_d$$

wherein Q is liquid flux, while V_d is diffusion volume (per minute) of vapor-molecule or gas-molecule through the real leaf or PDMS leaf.

As a result, gas-diffusion mediated overall hydraulic pressure gradient imposed on same microvascular geometry in both PDMS leaves and real leaves result in similar hydrodynamic flux through microvascular networks. So nature inspired PDMS leaves as introduced here, can provide Lab-on-a-chip platform for hydrodynamic flux analysis inside veinal microvasculature of natural leaf, as an alternative of conventional approaches.

As also proofed by Figure 12b, after the fluid totally fill in the all microvascular networks, lots of air bubbles are distributed evenly on the backside of PDMS leaf, confirming air-molecule diffusing form pressured PDMS leaves into ambient atmosphere after autonomous flow.

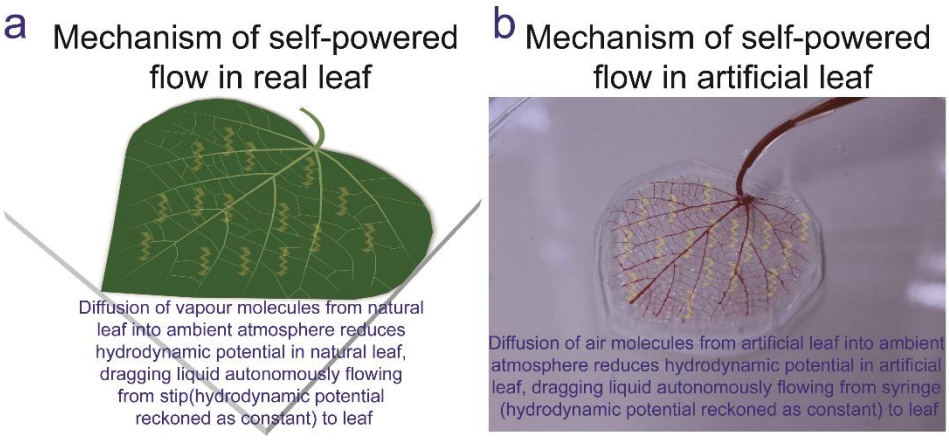

Figure. 12 The mechanism of self-pumped flow inside a real leaf and artificial leaf. (a) The schematic of a self-pumped flowing mechanism in a real leaf. The brown arrows under the schematic leaf represent the diffusion and evaporation of vapor molecules from the leaf into the atmosphere. (b) The self-pumped flowing mechanism in the artificial leaf. The brown arrows under the PDMS leaf represent the diffusion and evaporation of air molecules from the leaf into the atmosphere, with distribution of bubbles captured on the underside of the artificial leaf clearly visual inside the water bath.

Depending on aforementioned discussion, it's seen that diffusion micropump is different with all traditional micropumps. Because of its unique superiority of integrating so many advantages together, it can be widely applied in various types of microdevices. No doubt this new micropump will have dramatic significance in lots of different fields like biomedical fields and life sciences --- not only in basic research application, but also in commercial prospect accounting its simple structure, easy fabrication, compact size, high precision, low power consumption, and relatively fast response time. All these advantages are important issues of modern micropump area. Nevertheless, there haven't been any traditional micropumps able of realizing all these advantages together, reflecting the great prospect of the diffusion micropump.

2 Aims and scopes

The aims of this thesis are

Choose the most appropriate mechanical micropumps (syringe pump) and nonmechanical micropumps (capillary pump and diffusion pump) for different applications inside leaf-inspired and other microdevices.

These aims can be realized into the following parts

a) Choose syringe pump for application on multi-phage and micro-droplet fluidic control inside Y-structural PDMS-glass microchip (article 1), leakage & anticorrosive assay of PDMS-polymer device (article 2), and homogeneous velocity control inside 3D helical microreactor (article 5)

b) Choose capillary pump for application on self-activated & programmable velocity control inside 2.5D microstructures (article 1)

c) Choose diffusion pump for application on self-activated liquid transport inside leaf-inspired microdevices (article 3)

d) Choose diffusion pump for application on self-activated & homogeneous velocity control inside polymer device (article 4)

e) Choose diffusion pump for application on self-activated & inhomogeneous velocity control (article 5)

f) Choose diffusion pump for application on culture medium injection to leaf-inspired biomimetic microvasculature for cellular dynamic assay (article 6)

3 Publications

The results of this work are based on six articles from 2015. Five of them are published. One article has been submitted to journal.

(1) **Wenming Wu** and Andreas Manz, "Rapid manufacture of modifiable 2.5-dimensional (2.5D) microstructures for capillary force-driven fluidic velocity control", *RSC Adv.*, 2015, 5, 70737 - 70742. (SCI indexed, IF = 3.840) **(First author)**

(2) **Wenming Wu**, Jing Wu, Jae-Heon Kim and Nae Yoon Lee, "Instantaneous room temperature bonding of a wide range of non-silicon substrates with poly(dimethylsiloxane) (PDMS) elastomer mediated by a mercaptosilane", Lab on a Chip, 2015, 15, 2819-2825. (SCI indexed, IF = 6.112) (**First author**)

(3) **Wenming Wu**, Rosanne M. Guijt, Yuliya E. Silina, Marcus Koch, and Andreas Manz, "Plant leaves as templates for soft lithography" RSC Adv., 2016, 6, 22469–22475. (SCI indexed, IF = 3.840) **(First author)**

(4) **Wenming Wu**, Kieu The Loan Trinh; Yu Zhang and Nae Yoon Lee, "Portable plastic syringe as a self-actuated pump for long-distance uniform delivery of liquid inside a microchannel and its application for flow-through polymerase chain reaction on chip", RSC Adv., 2015, 5, 12071-12077. (SCI indexed, IF = 3.840) **(First author)**

(5) **Wenming Wu**, Kieu The Loan Trinh and Nae Yoon Lee, "Flow-through polymerase chain reaction inside a seamless 3D helical microreactor fabricated utilizing a silicone tube and a paraffin mold", Analyst, 2015,140, 1416-1420. (SCI indexed, IF = 4.107) Hot article in Analyst (Jan. 2015). **(First author)**

(6) **Wenming Wu** and Andreas Manz, "The manufacture of chamber-embedded microdevice from Tilia platyphyllos leaf, and the biocompatibility assay at single cell level", *submitted*. **(First author)**

The link of article (5) ~ (1) is as follows:

- Article 1：http://pubs.rsc.org/en/content/articlelanding/2015/ra/c5ra13407b#!divAbstract
- Article 2: http://pubs.rsc.org/en/Content/ArticleLanding/2015/LC/C5LC00285K#!divAbstract
- Article 3：http://pubs.rsc.org/en/content/articlelanding/2016/ra/c5ra25890a#!divAbstract
- Article 4：http://pubs.rsc.org/en/content/articlelanding/2015/ra/c4ra15473h#!divAbstract
- Article 5: http://pubs.rsc.org/en/content/articlelanding/2015/an/c4an01675k#!divAbstract

The contributions of Wenming Wu to above six articles include three main sections: 1. design the article 2. do the experiment 3. write the manuscript. And other authors also attend different sections of the articles.

In addition, although not proposed in this thesis, there are another eight papers published by the author, to provide his professional level to the area.

(1) **Wu** *et al.* Sens. Actuators B, 2014, 190, 177– 184. (SCI indexed, IF = 4.097) **(co-correspondence author)**

(2) **Wu** *et al.* Microchim Acta, 2014, 181, 1697–1705. (SCI indexed, IF = 3.740) **(Second author)**

(3) **Wu** *et al.* Sensors and Actuators B: Chemical, 2013, 181, 756. (SCI indexed, IF = 4.097) **(First author)**

(4) **Wu** *et al.* Sensors and Actuators B: Chemical, 2013, 181, 955. (SCI indexed, IF = 4.097, 18 citation) **(co-correspondence author)**

(5) **Wu** *et al.* Analyst, 2012, 137, 2069. (SCI indexed, IF = 4.107, 22 citation). a) Hot article in Analyst (Apr. 2012) b) Analyst Blog (Mar. 2012) c) Highlight featured in <<Technology Review>> [German version] (2012. 03. 30). d) Highlight featured in <<Chemistry World>> (2012. 05. 12). **(First author)**

(6) **Wu** *et al.* "Hand-held syringe as a portable plastic pump for on-chip continuous-flow PCR: miniaturization of sample injection device", Analyst, 2012, 137, 983. (SCI indexed, IF = 4.107, 16 citation) **(First author)**

(7) **Wu** *et al.* "Bubble-free on-chip continuous-flow polymerase chain reaction: concept and application", Analyst, 2011, 136, 2287. (SCI indexed, IF = 4.107, 20 citation) **(First author)**

(8) **Wu et al.** "Three-dimensional on-chip continuous-flow polymerase chain reaction employing a single heater", Anal Bio analytical Chemistry, 2011, 400, 2053. (SCI indexed, IF = 3.778 in 2011, 22 citation) **(First author)**

3.1 Wu *et al.* (2015)

Wenming Wu and Andreas Manz, "Rapid manufacture of modifiable 2.5-dimensional (2.5D) microstructures for capillary force-driven fluidic velocity control", *RSC Adv.*, 2015, 5, 70737 - 70742. (SCI indexed, IF = 3.840) **(First author)**

Authorship Contributions

Wenming Wu: participate in research design, conduct experiments, perform data analysis, and write the manuscript

Andreas Manz: participate in research design, data analysis and modify the manuscript

This work affirms capillary pump as an efficient approach in self-activated & programmable liquid delivery in 2.5D microchannel, while syringe pump as an efficient approach in microdroplet formation and multi-phase flow control in Y-structural PDMS-Glass chip fabricated from multilayer-tape lithography.

This paper reports rapid 2.5-dimensional (2.5D) lithography technique without the use of any clean-room staff or photoresist. In traditional methods, multiple exposures (e.g., photolithography), multiple etchings (e.g., dry etching), or multiple printings (e.g., inkjet printing) is inevitable for fabricating 2.5D microstructures containing a series of microchannels with different heights, which is always a laborious and time-consuming process. In comparison, here a 2.5D master mould can be structured in much less time simply by controlling the multilayer-tape. Furthermore, the height, width, and length of microchannels of the 2.5D master mold can be easily modified into various other structures, whereas, master mold can't afford any further modification once fabricated by traditional fabrication techniques (e.g., photolithography, dry etching, and inkjet printing). So for the case that a series of similar microstructures are required for parallel experiments or various applications, one same master mold can be repeatedly used after modification, without the necessity of fabricating a new master mould every time as before. If I use a scalpel to manually cut the microchannels in the tape mould, the smallest microchannel I fabricate is 500μm in width. For higher resolution (microchannel with width lower than 500μm), more accurate access like numerical control machine can be good candidate.

I test two kinds of pumping systems in three devices fabricated from multilayer-

tape lithography. One is directly through the usage of syringe pump, which can provide stable ink-droplets flow or multi-phase (oil-ink-oil) flow inside Y-structure PDMS chip, just by controlling flow rate of ink and oil at different velocity (Fig. 2, article 1). In addition, another portable energy free capillary pump is also applied to 2.5D microchip. I find microchannel-height can efficiently control sequential capillary-force-driven flow. The flowing-out time of blue ink inside 55 mm long microchannels are 4'35", 3'20", and 2'20" when microchannel height are 200 μm (fmy layers of tape), 300 μm (six layers of tape), and 400 μm (eight layers of tape), respectively.

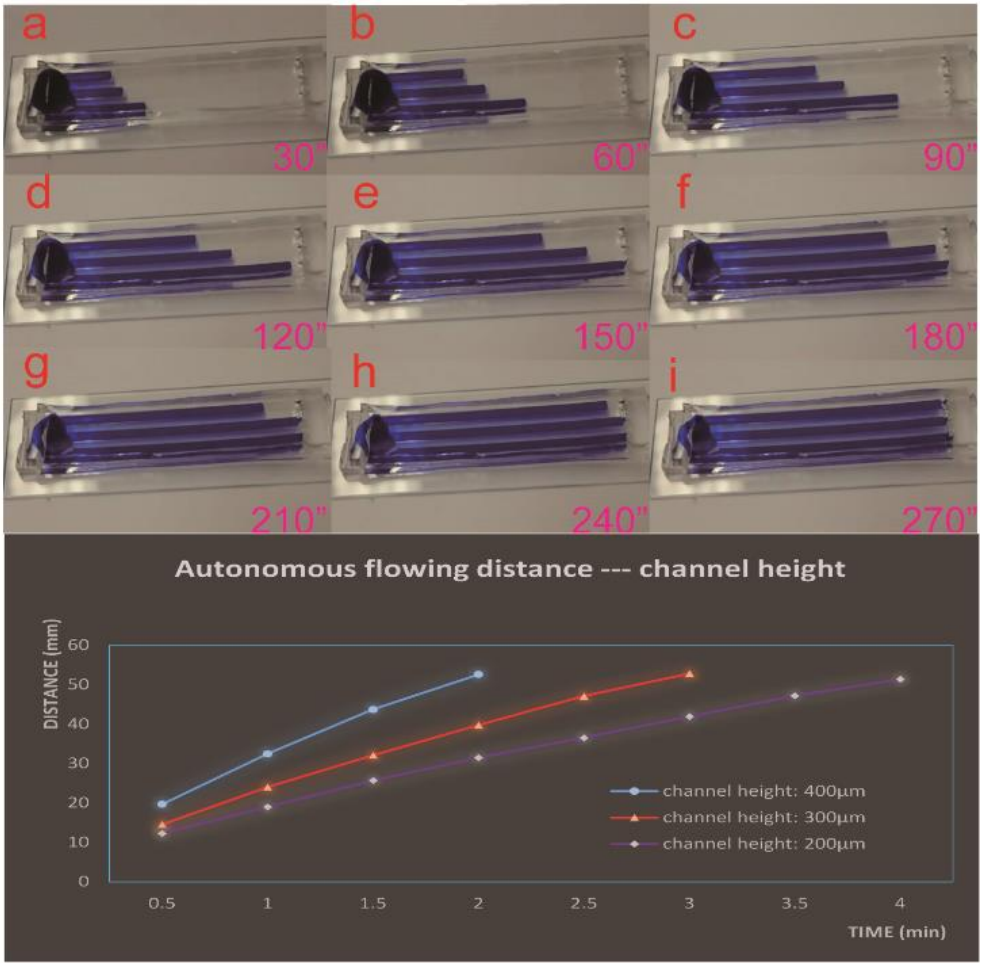

Figure 1. Capillary flow 2.5D chip. The height of the three channels are 200 μm, 300 μm, and 400 μm from top down, with a same channel length of 55 mm and channel width of 2.5 mm.

After detaching two, one, and one layer of tape from the three microchannels of 2.5D tape-master, the microchannel height changes to 100 μm, 250 μm and 300 μm, with flowing-out time changed to 7'50", 3'55", and 2'50", correspondingly (Fig. 4, article 1). Through further mathematical modeling, the relationship between microchannel-height and autonomous capillary flow-rate is systemically studied, verifying that autonomous capillary flow increases as the microchannel-height of 2.5D microchip increases. My model may initiate much easier methodology to functionalize autonomous programmable capillary-force-driven flow than other approaches depending on 2D microchip.

RSC Advances

COMMUNICATION

View Article Online
View Journal | View Issue

Cite this: *RSC Adv.*, 2015, **5**, 70737

Received 8th July 2015
Accepted 12th August 2015

DOI: 10.1039/c5ra13407b

www.rsc.org/advances

Rapid manufacture of modifiable 2.5-dimensional (2.5D) microstructures for capillary force-driven fluidic velocity control†

Wenming Wu[ab] and Andreas Manz*[ab]

A cost-effective, straightforward and modifiable 2.5D microfabrication methodology, as we term multi-layer-tape lithography, is presented here for the first time. It uses a commercial scalpel to prototype 2.5D multilevel microchannels on commercial tape as thin as 500 μm in minutes. Three functional microfluidic devices are applied with this methodology, and display high performance regarding microdroplet formation, multiphase flux and self-powered sequential fluid delivery. We find the microchannel height of a 2.5D microchip can efficiently control capillary force-driven flow velocity. The autonomous sample flow rates through 55 mm long microchannels are 0.1 μL s^{-1}, 0.21 μL s^{-1} and 0.39 μL s^{-1} when multilevel microchannel heights are 200 μm, 300 μm, and 400 μm, respectively. After detachment of two, one, and one layers of tape from the three microchannels of a 2.5D tape-master, the microchannel heights are modified to 100 μm, 250 μm and 300 μm, with the autonomous sample flow rate changing to 0.03 μL s^{-1}, 0.15 μL s^{-1} and 0.28 μL s^{-1}, correspondingly. In contrast with 2D microfabrication technology, we anticipate that multi-layer tape lithography will pave the way for researchers, especially those from resource-limited labs, to develop cost-effective, practical, self-powered, and disposable 2.5D microfluidic devices.

1 Introduction

Ever since the micro Total Analysis System (μTAS) was introduced by us in 1990,[1] there has been an explosion of interest in facilitating miniaturized μTAS-based devices as cost-effective, portable, disposable and rapid lab-on-a-chip (LOC) systems for diagnostic, chemical or bio-medical Point-Of-Care (POC) analysis. An on-chip integrated self-powered micropump is a key element in the ideal POC diagnostic chip, which should be 'affordable, user-friendly, rapid and equipment-free', according to the World Health Organization.[2] Since the early 2000s, various promising self-powered pumping mechanisms have been developed for autonomous sample delivery inside the microsystem. In our previous works, several internally self-powered micropumps were successfully introduced to activate autonomous sample transport inside very long microchannels of PDMS glass, PMMA–PMMA and silicon-tubing microchips.[3–5] Other self-powered pumping mechanisms have also been developed to automate self-powered fluidic transport inside microchips, such as mechanical force-driven pumping,[6] capillary force-driven pumping,[7] wicking force-driven pumping[8,9] vapour force-driven pumping,[10] and degas-driven pumping,[11] *etc.* Lately, Lee's group presented seminal work on an automated self-powered sample flow (red dye) through implementing internally encapsulated working liquid plug (blue dye) inside a 2D microchip, wherein autonomous sample flow can be programmed to be 0.07 μL s^{-1}, 0.12 μL s^{-1} and 0.17 μL s^{-1}, simply by adjusting circular section angles of on-chip fibrous material by 20°, 40° and 60°, respectively.[2] This smart method, exempt from external off-chip operations, improves internally self-powered micropumping systems for potential POC applications. Yet besides the analytical channel functionalized for sample transport and POC detection, a working liquid channel and activation chamber (2.6 mm and 5 mm in width, respectively) should be integrated inside the same device to increase overall device size and systemic complexity. Nowadays, most self-powered micropumps are applied to 2D microchips. We estimate that if 2.5D microfluidic platforms are utilized for self-powered liquid transport instead of 2D platforms, performance regarding autonomously programmable liquid delivery may be improved. Inspired by this idea, we innovated a truly cost-effective, user-friendly, portable, disposable and rapid way to realize self-powered programmable sample delivery inside 2.5D microchips, integrating parallel multilevel analytical channels for autonomous liquid delivery of different rates in each channel. Simply by controlling the heights of analytical

[a]*Mechatronics Department, University of Saarland, Saarbrücken, Germany. E-mail: manz@kist-europe.de*

[b]*KIST Europe, GmbH, Campus E7.1, 66123 Saarbrücken, Germany*

† Electronic supplementary information (ESI) available. See DOI: 10.1039/c5ra13407b

channels, a similar autonomous programmable flow rate can be obtained as previously reported.[2]

The manufacturing efficiency of 2.5D microdevices is one key factor determining how widely such autonomously programmable liquid delivery methodology may spread to potential users. Currently speaking, rapid and inexpensive 2.5D microfabrication methodology is still a major challenge in the microfluidic field today. In classic 2.5D microfabrication methods, repeated micro-patterning such as multi-exposures by photolithography, multi-carvings by CNC micromachining, or multi-etchings by chemical etching are the most popular approaches in fabricating 2.5D microchannels with multiple heights, and are laborious and time-consuming. For instance, the 'stacking method' is one popular technique for fabricating 2.5D microchips today, wherein a first layer of photoresist should be prefabricated on substrate with accurate positioning, followed by repeated exposure, aligning and stacking of photoresist for the second, third, and fourth… layers, to finally form multiple-height 2.5D microchannels.[12,13] Because of the operational difficulty of accurate alignment on the micro-scale, very complicated 2.5D microstructures (*i.e.*, multilevel microchannels with more than five multi-level heights) are not eligible for the 'stacking method'. Lately, Cooksey and Atenciaab introduced a 'folding method' for fabricating 2D and 3D microdevices.[14] Nevertheless, this method is still inapplicable to multi-height 2.5D microstructures. A number of other 3D or 2.5D microfabrication methodologies have been proposed by our group[15–17] and other groups[18–20] recently. However, most of these approaches require expensive manufacturing equipment, time-consuming steps or labour-intensive operations, and are thus inaccessible to researchers from resource-limited laboratories. To solve the challenges associated with 2.5D microfabrication, herein a multiple-layer tape-based manufacturing methodology is introduced for the first time, wholly depending on benchtop and straightforward instruments. Microchannels as thin as 500 μm in width can easily be carved on multi-layer tape in minutes by a commercial scalpel. The number of tape layers can be calculated as 'microchannel height divided by the tape height'. After different layers of tape are detached from the microchannels, a 2.5D tape master consisting of multi-level microchannels can easily form, waiving the need for laborious alignment steps and expensive machineries. Ever since Whitesides *et al.* introduced PDMS for microfabrication in the late 1990s,[21,22] PDMS has become the most widely used material for microfabrication today. As a proof of concept, herein three PDMS microchips are treated with this multi-layer-tape lithographical methodology. In contrast to other microfabrication techniques,[23–31] multi-layer-tape lithography is more accessible to potential μTAS users limited to expensive microfabrication instrumentation, and displays further potential for application in a wide range of fields such as chemistry, biology, pharmacy and medicine, *etc.* (ESI 1†).

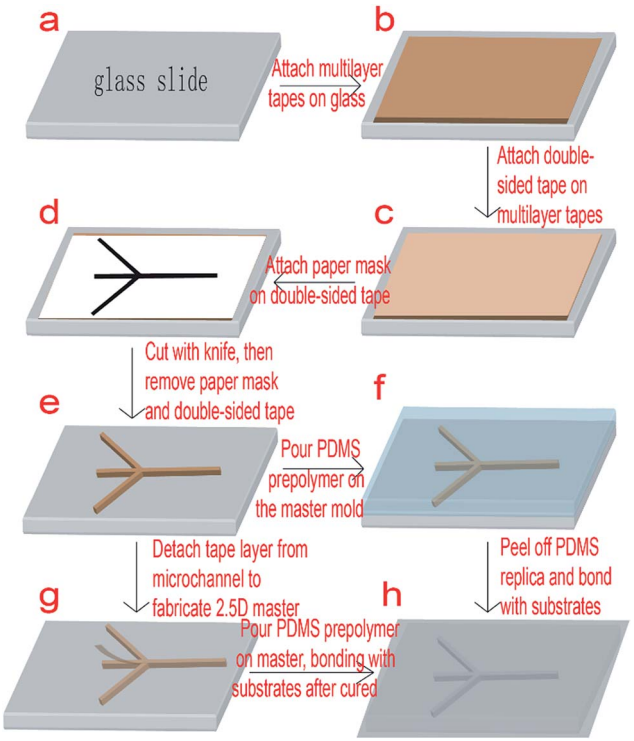

Fig. 1 Schematic steps of the multi-tape lithography for 2.5D microstructure fabrication. (a) The glass slide. (b) Multi-layer tape adheres to the glass slide. (c) Double-sided tape adheres to the multi-layer tape. (d) Paper mask is attached to the double-sided tape. (e) The multi-layer tape-master fabricated after removal of the paper mask. (f) After curing at 80 °C, for 30 min, the PDMS structure is peeled off. (g) A 2.5D master is made by detaching different layers of tape from each channel, according to the channel height. (h) PDMS replica is bonded with other substrates.

2 Experimental

2.1 Y-channel microchip

A schematic fabrication process of this 2.5D multi-layer-tape lithography is shown in Fig. 1. The channel height is determined by the number of tape (tesa 57176-00 tesapack ultra-strong tr. 66 m : 50 mm) layers attached to the glass slide, and can be conveniently adapted. The height of the tape is measured

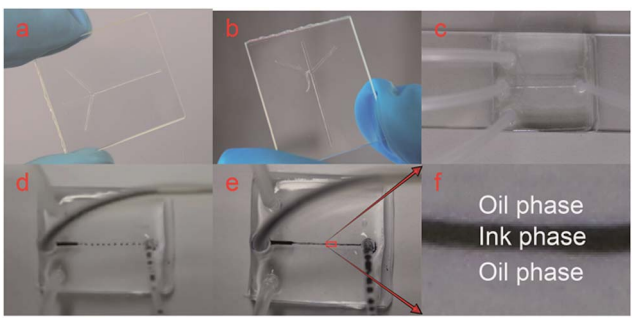

Fig. 2 (a) Three-layer tape-master, with a channel width of 500 μm and channel height of 150 μm. (b) One layer of tape is peeled off from the left channel of the tape-master in (a) to make a 2.5D tape-master. (c) The Y-structure PDMS chip fabricated by multi-layer-tape lithography. (d) Micro-droplet formation inside the Y-structure chip. The flow rates of ink and oil are 50 μL h^{-1} and 250 μL h^{-1}, respectively. (e) Multi-phase (oil-ink-oil) flow inside the Y-structure chip. The flow rates of ink and oil are 100 μL h^{-1} and 150 μL h^{-1}, respectively. (f) Magnification image of the multi-phase flow zone in (e), shown as a red rectangle.

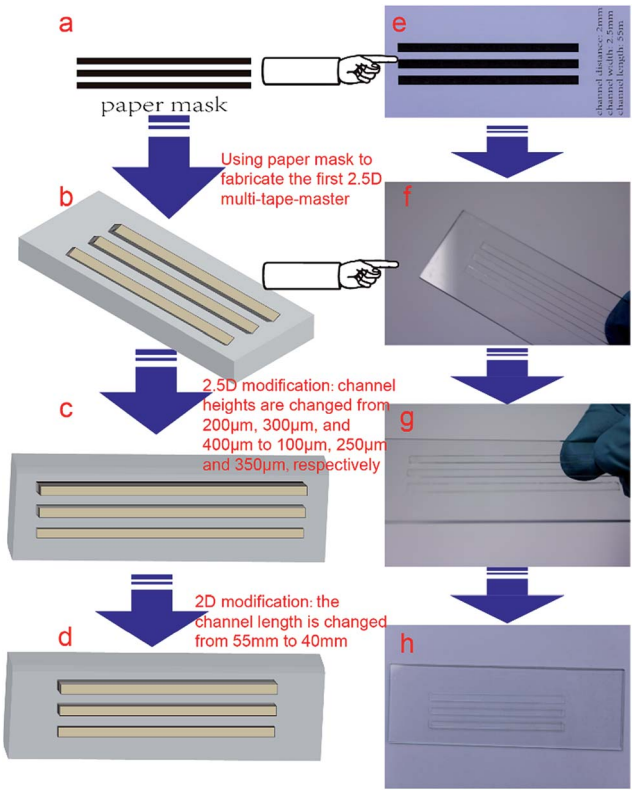

Fig. 3 The schematics for microchannel modification: 2D (channel length or width) and 2.5D (channel height) modifications of microstructure are done after the micro-device is fabricated. (a) The three-channel paper mask, with a channel length of 55 mm, channel distance of 2 mm, and channel width of 2.5 mm. (b) Original 2.5D tape-master with three parallel channel heights of 200 μm, 300 μm, and 400 μm, fabricated through multi-tape lithography. (c) One-time modifiable 2.5D tape-master, with three channel heights of 100 μm, 250 μm, and 350 μm, fabricated by directly modifying the multi-layer tape-master in (b). (d) Two-times modifiable 2.5D tape-master, with the same channel length of 45 mm, and three channel heights of 100 μm, 250 μm, and 350 μm, fabricated by directly modifying the tape-master in (c). (e) Real photo of paper mask. (f) Real photo of original tape-master. (g) Real photo of one-time modifiable tape-master. (h) Real photo of two-times modifiable tape-master.

by a Vernier calliper (Mitutoyo absolute digital). First, multiple layers of single-sided tape are attached to a paper mask (printed on an office printer) through double-sided tape (tesa double-sided tape 10 m : 15 mm) as shown in Fig. 1c. Second, the microstructure is cut into the tapes, with the paper mask and double-sided tape easily removed to leave a tape-glass hybrid master (Fig. 1e). After PDMS is poured in the master and cured (Fig. 1f), the PDMS replica can be taken off and bonded with a wide range of materials[23] (Fig. 1h) to make a functional chip. Tape layers in each channel can be detached depending on the required channel height to make the appropriate 2.5D structures (Fig. 1g).

We first fabricate one three-layer- tape-master (Fig. 2a) through this multi-layer-tape lithography, with a channel width of 500 μm and channel height of 150 μm. As shown in Fig. 2b, the tape layer can easily be detached from the 2D tape channel to fabricate a 2.5D tape-master. A Y-structure PDMS (Sylgard® 184) chip (Fig. 2c) is also fabricated from the multi-layer tape-master in Fig. 2a, with PDMS replica and glass substrate bonded by oxygen plasma (Diener electronic: 0010915) at a power of 75 W for 30 s. As shown in Fig. 2d and e, micro droplets and multiphase flow can stably form in this chip, demonstrating multi-layer tape lithography quantified for microfabrication. The quantified stable micro-droplet formation inside this chip is also provided in ESI 2,† promising a wide range of microdroplet-applicant downstream fields such as cultivation of mammalian cells,[32] controllable synthesis of nanoplates,[33] and interactional assay of cell pairs,[34] *etc.*

2.2 Parallel channel microchip

Furthermore, a 2.5D master containing three parallel channels with multi-level heights of 200 μm, 300 μm, and 400 μm, respectively, is fabricated by this 2.5D multi-layer tape lithography. To reveal the feasibility of the microstructural modifiability of this technique, modifications are realized to all three channels of the 2.5D tape-master, both in channel height (Fig. 3b, c, f and g) and in channel length (Fig. 3c, d, g and h). Tape layers of the three channels in Fig. 3b and f are four, six, and eight, respectively, corresponding to 200 μm, 300 μm, and 400 μm in channel height. Simply by detaching two, one, and one layers of tape from these three channels, we can change the multi-level channel heights to 100 μm, 250 μm, and 300 μm, finally. We also find that it is very easy to modify channels in the 2D level (width and length). As shown in Fig. 3c and d, after modification on three channels, the length of all channels changes from 55 mm to 45 mm. This proves that both 2D (channel length or width) and 2.5D (channel height) modification of the microstructure can be easily realized on the existing master, without the necessity of fabricating a new master.

3 Results and discussion

3.1 Programmable capillary flow

Two 2.5D microchips are fabricated from two tape-masters (Fig. 3f and g), with PDMS surface functionalized through oxygen plasma at 35 W for 0.7 min. We found programmable autonomous flow is easily produced in parallel 2.5D channels after sample injection (ESI 3†).

It requires about 4′35″, 3′20″, and 2′20″ for the ink flowing through three parallel channels of the first capillary flow chip (Fig. S1, ESI 4†), with multi-level heights of 200 μm, 300 μm, and 400 μm, respectively. Correspondingly, the autonomous sample flow rates through three 55 mm long microchannels are calculated to be 0.1 μL s^{-1}, 0.21 μL s^{-1} and 0.39 μL s^{-1}, respectively. Without the necessity of fabricating a new master, the second capillary flow chip is fabricated simply by detaching two, one, and one layers of tape from the three microchannels of the first 2.5D tape-master (Fig. 3f), with channel height changed to 100 μm, 250 μm, and 350 μm (Fig. 3g). As a result, total flowing-out time is changed to 7′50″, 3′55″, and 2′50″ (Fig. S2, ESI 4†), respectively. Correspondingly, autonomous sample flow rates

through three 55 mm long parallel microchannels are calculated to be 0.03 μL s^{-1}, 0.15 μL s^{-1} and 0.28 μL s^{-1}, respectively.

Quantitative analysis of autonomous flow distance (mm) is plotted against time (min), as indicated in Fig. 4. Because channel length (55 mm), channel width (2 mm), and surface functionalization (oxygen plasma at 35 W for 0.7 min) are all the same for three parallel multi-level microchannels, except for channel height, we can conclude that the sequential autonomous flow rate through these channels is dictated by channel height. As shown in Fig. 4, as the channel height increases, the flow rate becomes faster, and it displays the same trend in both the first capillary flow chip (Fig. S1, ESI 4†) and the second capillary flow chip (Fig. S2, ESI 4†). On the basis of the aforementioned analysis, we estimate a channel-height controlled autonomous programmable chip can be realized in accordance with the theoretical analysis, as illustrated in "Section 3.2".

3.2 Mathematical modelling

To theoretically verify the relationship between capillary flow rate and multi-level channel height, the fluidic hydrodynamic inside the 2.5D microchip is further analysed, wherein flowing velocity is determined by both the capillary driven force F_c and the capillary resistance force F_R. As shown in Fig. S3 of ESI 4,† F_c is in the same direction with the capillary flow, whereas F_R is in the opposite flow direction. The flowing velocity can be derived and calculated by the following equation,

$$F_c = F_R$$

If the micro-channel is a column with a circular cross-section, the flowing resistance force F_R can be calculated by the Hagen–Poiseuille equation:

$$-\frac{dp_l}{dz} = \frac{8\eta u}{r^2}$$

where η is the viscosity of the liquid, p_l is the internal pressure of the liquid medium which is proportional to the flowing resistance force, u is flowing velocity, and r is radius.

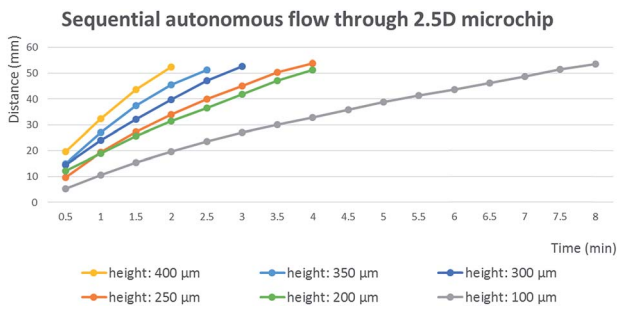

Fig. 4 Quantitative analysis of sequential autonomous flow inside 2.5D microchips with multi-level channel height of 100 μm (grey dotted line), 200 μm (green dotted line), 250 μm (henna dotted line), 300 μm (deep blue dotted line), 350 μm (light blue dotted line) and 400 μm (brown dotted line), respectively. Channel length and width are 2 mm and 55 mm, respectively.

From this equation, we can estimate that the velocity is in proportion to the square of the diameter of the column microchannel. In other words, the flowing-out time decreases as the column microchannel diameter increases.

However, the cross-section of the channel here is rectangular instead of circular. In previous work, we have systemically analysed the relationship between the flowing resistance force and the flowing velocity inside a channel with a rectangular cross-section, which is the same channel type as used here, and it can be represented by the following equation,[28]

$$-\frac{dp_l}{dz} = \frac{\lambda\rho u^2}{2d_h}$$

where λ is a frictional coefficient of capillary-driven flow, ρ is liquid density, u is flowing velocity, and d_h is the equivalent diameter of the rectangular microchannel.

It is easily seen that, as the channel height increases, d_h will increase, resulting in decreased resistance force. Therefore the flowing velocity should increase if the channel height increases, resulting in decreased flowing-out time.

3.3 Microchannel characterization

We further use a scanning electronic microscope (QUANTA FEG250) and optical microscope (Zeiss axiovert S100) to characterize the surface smoothness of 2.5D tape-masters. Multi-level tape layers of 3, 5, 7 and 11, as well as intersectional multiple tape layers of 11–10 and 4–3, are selected for characterizing both the top surface and the cross-sectional surface. As shown in Fig. 5a–c, the top surface of the tape-master displays qualified smoothness, comparable to the surface of a glass slide. At 16 000× magnification, dot-like structure as little as 100 nm is found (Fig. S4, ESI 4†), proving roughness at top surface of the multi-layer tape-master is ignorable at micro-meter scale. However, the smoothness of the boundary surfaces in the multi-layer tape-master depends on the height of the tape in use. There are some curved grooves between tape layers, which are around 10 μm in height, as shown in Fig. 5a–c. To better reveal these curved grooves, the cross-section of the multi-layer tape-master is further characterized (Fig. 5d–f). Because the multi-layer 2.5D tape-master is built up of a single layer of tape as a constructional unit, the tape layer is visible and has about 10 μm high curved grooves in between, as shown in Fig. 5d and f. Intersectional height decrease of 2.5D tape-master is also characterized in Fig. 5e and f, wherein one layer of tape is detached in intersectional locations to produce a reduction of channel height by 50 μm from left to right in both cases.

Similarly to photolithography-based master prototyping wherein proper photoresist (*e.g.*, SU-8 2005, SU-8 2007, SU-8 2010 or SU-8 2015, *etc.*) should be selected depending on the specialized microchannel height, herein suitable tape (10 μm, 50 μm, 100 μm, in height *etc.*) should also be dependent on microchannel height. In our case, the height of all microchannels (Fig. 2 and 3) are within 400 μm, so tape 50 μm in height (tesa 57176-00 tesapack ultra-strong tr. 66 m : 50 mm) is appropriate for prototyping microchannels. Nevertheless, if a

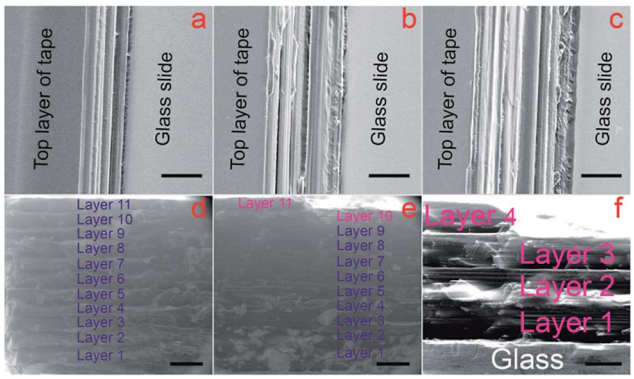

Fig. 5 The SEM image of the tape-master. (a) The boundary of a three-layer tape channel. (b) The boundary of a five-layer tape channel. (c) The boundary of a seven-layer tape channel. (d) The cross-section of an 11-layer tape channel. (e) The cross-section of the 11-layer and 10-layer tape channel. (f) The cross-section of the four-layer and three-layer tape channel. Rule bars are 125 μm in (a–c); 100 μm in (d and e); and 50 μm in (f).

master with channel height lower than 50 μm should be fabricated, then the selected tape height should be less than 50 μm, such as 10 μm or 25 μm. The height of the tape also affects the resolution of the channel height of the microchip. For example, if two kinds of single-sided tape with heights of 10 μm and 15 μm are selected, then a height resolution of 5 μm can be realized, because a channel height of 10 μm, 15 μm, 20 μm, and 25 μm… *etc.*, can be fabricated simply by arranging these two kinds of tape.

4 Conclusion

This paper reports a multi-layer tape lithography for fabricating 2.5D microchips easily, rapidly and cheaply. Without any expensive instruments or reagents, the total manufacturing cost of a 2.5D master by multi-layer tape lithography is under 0.03 US$, allowing convenient microstructural modification of the tape-master in both 2D level (channel length is modified by 10 mm here) and 2.5D level (channel heights are modified by 50 μm and 100 μm here). If we use a commercial scalpel to manually cut microchannels in the multi-layer tape, the smallest microchannel width is 500 μm. A Y-shaped microchannel as thin as 500 μm in width is directly fabricated through a manual knife-cut, quantified for microdroplet formation when the flow rates of ink phage and oil phage are 50 μL h^{-1} and 250 μL h^{-1}, respectively, and multi-phage flow when the flow rates of ink and oil are 100 μL h^{-1} and 150 μL h^{-1}, respectively.

Sequential and programmable autonomous flow is realized in 2.5D microchips fabricated through this multi-layer tape lithography. Two 2.5D capillary force-driven flow chips are fabricated, with channel heights controlled to be 200 μm, 300 μm, and 400 μm for the first chip, and 100 μm, 250 μm, 350 μm for the second chip. The flowing-out time of ink in 55 mm long channels increases from 2′20″ to 7′50″ as the height of channel decreases from 400 μm to 100 μm, suggesting that the channel height is an efficient approach for controlling the capillary flow rate, as supplementary of previous methods relying on a 2D microchip. Through mathematical modelling, the relationship between microchannel height and autonomous capillary flow rate is also systemically studied, verifying that autonomous capillary flow rate increases as the multilevel microchannel increases in height, in accordance with experimental results.

Given the aforementioned advantages, we believe that multi-layer tape lithography can dramatically decrease the microfabrication expense of 2.5D microdevices and thus lower the barrier to the widespread use of microfluidic POC chips in non-engineering labs or automatic analysis labs, which may be unable to afford expensive clean rooms, UV transmitters or inkjet printer, *etc.*

References

1 A. Manz, N. Graber and H. M. Widmer, *Sens. Actuators, B*, 1990, **1**, 244.
2 T. Kokalj, Y. Park, M. Vencelj, M. Jenko and L. P. Lee, *Lab Chip*, 2014, **14**, 4329.
3 W. Wu, K. T. L. Trinh and N. Y. Lee, *RSC Adv.*, 2015, **5**, 12071.
4 W. Wu, K. T. L. Trinh and N. Y. Lee, *Analyst*, 2012, **137**, 983.
5 W. Wu, K. T. L. Trinh and N. Y. Lee, *Analyst*, 2015, **140**, 1416.
6 H. Hwang, S.-H. Kim, T.-H. Kim, J.-K. Park and Y. Kyoung, *Lab Chip*, 2011, **11**, 3404.
7 P. Novo, F. Volpetti, V. Chu and J. P. Conde, *Lab Chip*, 2013, **13**, 641.
8 B. Lutz, T. Liang, E. Fu, S. Ramachandran, P. Kauffman and P. Yager, *Lab Chip*, 2013, **13**, 2840.
9 G. M. Whitesides, *Lab Chip*, 2013, **13**, 4004.
10 S. Begolo, D. V. Zhukov, D. A. Selck, L. Li and R. F. Ismagilov, *Lab Chip*, 2014, **14**, 4616.
11 I. K. Dimov, L. Basabe-Desmonts, J. L. Garcia-Cordero, B. M. Ross, A. J. Ricco and L. P. Lee, *Lab Chip*, 2011, **11**, 845.
12 D. T. Chiu, E. Pezzoli, H. Wu, A. D. Stroock and G. M. Whitesides, *Proc. Natl. Acad. Sci. U. S. A.*, 2001, **98**, 2961.
13 M. Zhang, J. Wu, L. Wang, K. Xiao and W. Wen, *Lab Chip*, 2010, **10**, 1199.
14 G. A. Cooksey and J. Atenciaab, *Lab Chip*, 2014, **14**, 1665.
15 W. Wu and N. Y. Lee, *Anal. Bioanal. Chem.*, 2011, **400**, 2053.
16 W. Wu and N. Y. Lee, *Sens. Actuators, B*, 2013, **181**, 756.
17 W. Wu, K. T. L. Trinh and N. Y. Lee, *Analyst*, 2012, **137**, 2069.
18 P. K. Yuen and V. N. Goral, *Lab Chip*, 2010, **10**, 384.
19 W. Lee, D. Kwon, W. Choi, G. Y. Jung and S. Jeon, *Sci. Rep.*, 2015, **5**, 7717.
20 M. Zhang, J. Wu, L. Wang, K. Xiao and W. Wen, *Lab Chip*, 2010, **10**, 1199.
21 J. C. McDonald, D. C. Duffy, J. R. Anderson, D. T. Chiu, H. Wu, O. J. A. Schueller and G. M. Whitesides, *Electrophoresis*, 2000, **21**, 27.
22 G. M. Whitesides, E. Ostuni, S. Takayama, X. Jiang and D. E. Ingber, *Annu. Rev. Biomed. Eng.*, 2001, **3**, 335.
23 W. Wu, J. Wu, J. H. Kima and N. Y. Lee, *Lab Chip*, 2015, **15**, 2819–2825.

24 T. Kwa, Q. Zhou, Y. Gao, A. Rahimian, L. Kwon, Y. Liu and A. Revzin, *Lab Chip*, 2014, **14**, 1695.
25 R. L. Hartman, H. R. Sahoo, B. C. Yen and K. F. Jensen, *Lab Chip*, 2009, **9**, 1843.
26 P. Vulto, P. Kuhn and G. A. Urbanb, *Lab Chip*, 2013, **13**, 2931.
27 L. Zhang, W. Wang, X. Ju, R. Xie, Z. Liu and L. Chu, *RSC Adv.*, 2015, **5**, 5638.
28 W. Wu, K. T. Kang and N. Y. Lee, *Analyst*, 2011, **136**, 2287.
29 J. Kim, R. Surapaneni and B. K. Gale, *Lab Chip*, 2009, **9**, 1290.
30 X. Fang, S. Wei and J. Kong, *Lab Chip*, 2014, **14**, 911.
31 A. D. ávan der Meer, P. Dijke and A. den Berg, *Lab Chip*, 2013, **13**, 3562.
32 H. Hufnagel, A. Huebner, C. Gülch, K. Güse, C. Abell and F. Hollfelder, *Lab Chip*, 2009, **9**, 1576.
33 Q. Fu, G. Rana and W. Xu, *RSC Adv.*, 2015, **5**, 37512.
34 T. P. Lagus and J. F. Edd, *RSC Adv.*, 2013, **3**, 20512.

3.2 Wu *et al.* (2015)

Wenming Wu, Jing Wu, Jae-Heon Kim and Nae Yoon Lee, "Instantaneous room temperature bonding of a wide range of non-silicon substrates with poly(dimethylsiloxane) (PDMS) elastomer mediated by a mercaptosilane", Lab on a Chip, 2015, 15, 2819-2825. (SCI indexed, IF = 6.115) **(First author)**

This cooperated project is done with Prof. Nae Yoon Lee of Gachon University in Korea, and Prof. Manz provides sincere encourages and supports for such international cooperative project.

Authorship Contributions

Wenming Wu: design research and methodology, contribute to experimental principle, conduct experiments, perform data analysis, write and modify the manuscript

Jing Wu: conduct experiments, perform data analysis, and modify the manuscript

Jae-Heon Kim: conduct experiments (e.g., pull test part, leak test part, large area bonding and XPS analysis part)

Nae Yoon Lee: participate in research design, perform data analysis, and modify the manuscript

This work affirms syringe pump as an efficient approach in accurate liquid injection in novel 2D PDMS/Polymer microdevice for anticorrosive assay and leakage test.

PDMS is the most widely utilized material for microdevices today. Although PDMS can readily bond with another silicon-based material (such as glass, silicon wafer, and quartz) through simple surface oxidation, its ability to form irreversible chemical bonds with non-silicon-based materials such as plastics, metals, alloys, and ceramics is hampered. In this study, I introduce a concept for fabricating novel hybrid microdevices by instantaneously bonding versatile non-silicon-based substrates with PDMS at room temperature utilizing single silane coupling reagent,

3-mercaptopropyltrimethoxysilane (MPTMS). Over ten non-silicon substrates including polycarbonate (PC), two types of poly(vinylchloride) (PVC), poly(methylmethacrylate) (PMMA), polystyrene (PS), polyimide (PI), two types of poly(ethylene terephthalate) (PET), polypropylene (PP), iron (Fe), aluminum (Al), copper (Cu), brass, alumina (Al_2O_3), and zirconia (ZrO_2) are bonded successfully with PDMS using this method. In addition to a series of characterization including contact angle measurement, XPS analysis, delamination and pull tests, I utilize two kinds of leak tests to check this robust method, and two liquids are transported through two different microdevices at controllable rate.

For the first test, PDMS slide containing a serpentine microchannel with width, depth, and total length of 2 mm, 200 μm, and 115 mm, respectively, is bonded on flat PVC. As shown in Fig. 6a-b, no leakage happens even if tetrahydrofuran (THF) is transported to the microchannel at a flow rate of 1 mL/min for 25 min by syringe pump and further kept inside the microchannel for up to 8 h, although noticeable swelling of PDMS takes place. The second microdevice is PDMS–PMMA microchip, engraved with a dense serpentine microchannel network whose width, depth, microchannel distance and total length are 300 μm, 100 μm, 100 μm and 1.8 m, respectively. To produce high pressure on the microchannel during liquid transport, the red ink is controlled to flow out of the 1.8 m-long serpentine microchannel within 3 min. As shown in Fig. 6, no leakage occurs inside the microchannel, confirming the instantaneous and robust bonding between PDMS and PMMA.

So I affirm that syringe pump is qualified to provide accurate flow rate during liquid transport, and thus, can be efficient approach in anticorrosive assay and leakage test of novel PDMS/Polymer microdevice.

Lab on a Chip

PAPER

View Article Online
View Journal | View Issue

Cite this: *Lab Chip*, 2015, **15**, 2819

Instantaneous room temperature bonding of a wide range of non-silicon substrates with poly(dimethylsiloxane) (PDMS) elastomer mediated by a mercaptosilane†

Wenming Wu,‡[a] Jing Wu,§[a] Jae-Heon Kim[a] and Nae Yoon Lee*[ab]

Received 10th March 2015,
Accepted 8th May 2015

DOI: 10.1039/c5lc00285k

www.rsc.org/loc

This paper introduces an instantaneous and robust strategy for bonding a variety of non-silicon substrates such as thermoplastics, metals, an alloy, and ceramics to poly(dimethylsiloxane) (PDMS) irreversibly, mediated by one-step chemical modification using a mercaptosilane at room temperature followed by corona treatment to realize heterogeneous assembly also at room temperature. The mercapto functional group is one of the strongest nucleophiles, and it can instantaneously react with electrophiles of substrates, resulting in an alkoxysilane-terminated substrate at room temperature. In this way, prior oxidation of the substrate is dispensed with, and the alkoxysilane-terminated substrate can be readily oxidized and irreversibly bonded with oxidized PDMS at room temperature. A commercially available Tesla coil was used for surface oxidation, replacing a bulky and expensive plasma generator. Surface characterization was conducted by water contact angle measurement and X-ray photoelectron spectroscopy (XPS) analysis. A total of fifteen non-silicon substrates including polycarbonate (PC), two types of poly(vinylchloride) (PVC), poly(methylmethacrylate) (PMMA), polystyrene (PS), polyimide (PI), two types of poly(ethylene terephthalate) (PET), polypropylene (PP), iron (Fe), aluminum (Al), copper (Cu), brass, alumina (Al_2O_3), and zirconia (ZrO_2) were bonded successfully with PDMS using this method, and the bond strengths of PDMS–PMMA, PDMS–PC, PDMS–PVC, PDMS–PET, PDMS–Al, and PDMS–Cu assemblies were measured to be approximately 335.9, 511.4, 467.3, 476.4, 282.2, and 236.7 kPa, respectively. The overall processes including surface modification followed by surface oxidation using corona treatment for bonding were realized within 12 to 17 min for most of the substrates tested except for ceramics which required 1 h for the bonding. In addition, large area (10 × 10 cm^2) bonding was also successfully realized, ensuring the high reliability and stability of the introduced method.

Introduction

The first introduction of a transparent elastomer, poly(dimethylsiloxane) (PDMS), as a casting material for soft lithography has opened a new horizon for microfabrication and brought extensive repertoire of PDMS as a material of choice for fabricating microdevices particularly in the fields of microfluidics, Lab-on-a-Chip, and micro total analysis systems (μTAS).[1–4] Substrate bonding is indispensable not just for the construction of miniaturized fluidic devices that are applicable to microscale biological experiments, but also for numerous fields of applications such as microelectronics and packaging. Although PDMS can readily bond substantially with another silicon-based material such as glass, silicon wafer, and quartz through simple surface oxidation and thermal curing,[5–7] its ability to form robust and irreversible chemical bonds with non-silicon-based materials such as plastics, metals, alloys, and ceramics in the assembly process is hampered.[8] Considering that hybrid microstructures constructed with PDMS and non-silicon-based materials have potential benefits when fabricating microvalves[9–11] and when assembling heterogeneous substrates in microelectronics and packaging areas, researchers began to show great interest

[a] *Department of BioNano Technology, Gachon University, 1342 Seongnam-daero, Sujeong-gu, Seongnam-si, Gyeonggi-do 461-701, Korea.*
E-mail: nylee@gachon.ac.kr
[b] *Gachon Medical Research Institute, Gil Medical Center, Inchon 405-760, Korea*

† Electronic supplementary information (ESI) available. See DOI: 10.1039/c5lc00285k

‡ Current address: Department of Mechatronics, University of Saarland, Saarbrücken, Germany & KIST Europe GmbH, Campus E7.1, 66123 Saarbrücken, Germany.

§ Current address: Department of Mechanical Engineering, University of Hong Kong, Haking Wong Building, Pokfulam Road, Pokfulam, Hong Kong.

concerning the bonding of silicon-based PDMS with non-silicon-based substrates.[12–24]

Im *et al.*[12] grafted an epoxy-containing polymer, poly(glycidyl methacrylate) (PGMA), *via* an initiated chemical deposition (iCVD) method and reacted it with a partner substrate activated with plasma polymerized polyallylamine (PAAm) to realize bonding at 70 °C. Xu and Gleason[13] deposited glycidyl methacrylate and 4-aminostyrene on substrates *via* iCVD and bonded them at 50 °C for 24 h. Several researchers employed either an amine-functionalized silane reagent[14,17,19] or a methacrylate-functionalized silane reagent[16] as an adhesion promoter on thermoplastic surfaces and bonded it with PDMS after surface oxidation of both substrates. In our previous studies,[18,21] we demonstrated room temperature bonding of various thermoplastics with PDMS by forming a robust amine–epoxy bond employing aminosilane and epoxysilane.[25] Most of the previous studies mentioned above, however, require prior surface oxidation followed by surface functionalization with silane coupling reagents having diverse terminal functionalities. Besides, these methods generally take more than an hour altogether for surface modification and subsequent bonding and require the use of multiple reagents for surface modification, or harsh environment such as high temperature and high pressure for bonding, not to mention the use of expensive and bulky apparatus.

To simplify the surface coating procedures prior to bonding, Lee and Ram[15] demonstrated hydrolytically stable coating of amine-containing silane reagents on polycarbonate (PC) by reacting the amine functionality with PC, but required heating at 70 °C for 24 h for bonding. We also employed either an amine-functionalized silane coupling reagent[20,26] or amine-functionalized PDMS[22] as a linker for coating thermoplastics which can undergo urethane bond formation[27] at room temperature by the reaction of the amine functionality with the carbonyl backbone of thermoplastics, and bonded the coated substrates with PDMS after surface oxidation of both substrates. Nevertheless, each bonding method is limited to certain types of substrates, and no reports were made to date on a universally applicable method for bonding PDMS with a wide range of non-silicon substrates.

In this study, we introduce a novel concept for instantaneously bonding versatile non-silicon-based substrates with PDMS at room temperature without requiring prior surface oxidation and utilizing a single silane coupling reagent, 3-mercaptopropyltrimethoxysilane (MPTMS). Fig. 1 shows the schematics for room temperature modification of non-silicon-based substrates employing MPTMS. Fig. 1a shows a substrate containing electrophilic groups on the surface. δ+ and δ− represent the electrophilic and nucleophilic sites, respectively. Fig. 1b shows the reaction of the substrate with an aqueous solution of MPTMS. Hydrolysis occurs in the alkoxy terminal of MPTMS, while nucleophilic reaction takes place between the mercapto functional group of MPTMS and the substrate. Fig. 1c shows the hydrolysis of the alkoxy terminal of MPTMS, producing alcohol and resulting in the cross-linking of adjacent MPTMS molecules. Fig. 1d shows the nucleophilic reaction between the mercapto functional group of MPTMS and the substrate, resulting in the grafting

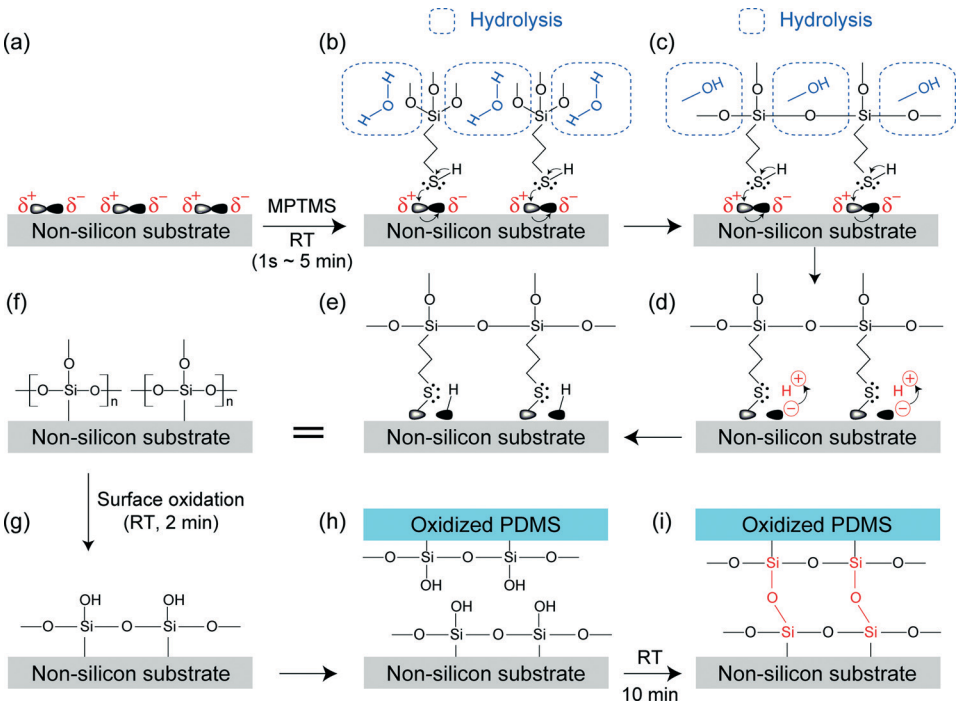

Fig. 1 Schematics illustrating procedures for (a–f) surface modification with 2% MPTMS at room temperature on a non-silicon substrate, and (g–i) bonding of an oxidized non-silicon substrate with oxidized PDMS realized at room temperature for 10 min.

of MPTMS on the substrate. Fig. 1e shows the formation of the alkoxysilane-terminated substrate as a result of the reaction with MPTMS, the simplified schematic of which is shown in Fig. 1f. Fig. 1g shows the oxidation of the alkoxy terminal of the substrate at room temperature for 2 min, and Fig. 1h shows the conformal contact of the two substrates at room temperature for 10 min.

Although the use of aminosilane can also facilitate bonding between several thermoplastics and PDMS, the number of substrates reported so far was limited to a few.[14,17,19,27] Since it is well-known that the mercapto functionality has stronger nucleophilic properties than the amino functionality, we chose mercaptosilane as a linker for surface modification in this study. The bonding performance of fifteen non-silicon-based materials was examined including several thermoplastics, metals, an alloy, and ceramics.

Experimental

Materials

3-Mercaptopropyltrimethoxysilane (MPTMS) was purchased from Sigma-Aldrich. The PDMS prepolymer (Sylgard 184) and curing agent were purchased from Dow Corning. Polycarbonate (PC), poly(methylmethacrylate) (PMMA), polystyrene (PS), poly(ethylene terephthalate) (PET), polypropylene (PP), poly(vinylchloride) (PVC), aluminum (Al), copper (Cu), and brass were purchased from Goodfellow. PI (Kapton) was purchased from DuPont. A Tesla coil (BD-10ASV, Electro-Technic Products) was used for the corona discharge.[28]

Surface modification and bonding

The thermoplastics, metals, and alloy were treated with a 2% (v/v) aqueous solution of MPTMS at room temperature instantaneously in the case of the thermoplastics, and for 1–5 min for the metals and the alloy. After rinsing with distilled water and drying, the abovementioned substrates and PDMS were treated by corona discharge for 2 min, and immediately after surface oxidation, they came into conformal contact with each other for 10 min to realize irreversible bonding at room temperature. The percentages of MPTMS could be varied within the range between 1 and 10%. Due to the strong reactivity of the mercapto-terminated silane coupling reagent, the solution was freshly prepared immediately before the experiment and discarded after approximately 30 to 60 min. In the case of the ceramics, MPTMS was used without dilution, and bonded with PDMS at 80 °C for 30 min. Movie S1 in the ESI† demonstrates the overall procedures including surface modification of PMMA with MPTMS and subsequent bonding with PDMS. In this movie, an oxygen plasma generator was used instead of the Tesla coil, which resulted in a much faster and instantaneous bonding.

Surface characterization

Contact angle measurement. Water contact angles were measured on pristine substrates, MPTMS(2%)-treated substrates, MPTMS(2%)-coated substrates further treated with corona discharge, and corona-treated pristine substrates, by the sessile drop technique using a Phoenix 300 contact angle measuring system (Surface Electro Optics, Korea). The contact angles were further analysed with Image Pro 300 software.

XPS analysis. XPS analyses were conducted using an Axis-Hsi (Kratos Analytical, UK) equipped with a magnesium X-ray radiation source of dual gun (1253.6 eV) and a pass energy of 20 eV. The pressure in the chamber was below 5×10^{-9} Torr before the data were taken, and the voltage and current of the anode were 15 kV and 10 mA, respectively. The take-off angle was set at 45°. The binding energy of C1s (284.5 eV) was used as the reference. The resolution for the measurement of the binding energy was about 0.1 eV.

Bond strength analysis

Delamination and pull tests. A delamination test was performed on all fifteen substrates. The bond strength was measured using a texture analyser (QTS 25, Brookfield, Middleboro, MA, USA). First, a hole was punched on the non-silicon substrate and a thick twine was inserted. Next, another twine was inserted into the PDMS prepolymer and cured simultaneously with PDMS. After bonding the two substrates, the assembly was pulled apart at a speed of 100 mm min^{-1}. The experiments were repeated three times for reproducibility.

Leak test. Two kinds of leak tests were performed. For the first test, a thick and short serpentine microchannel whose width, depth, and total length were 2 mm, 200 μm, and 115 mm, respectively, was made on the PDMS side and bonded with flat PVC according to the method mentioned above. Afterward, tetrahydrofuran (THF) was introduced into the microchannel at a flow rate of 1 mL min^{-1} for 25 min and kept inside the microchannel for 8 h to observe whether swelling of the PDMS affected the bonding. For the second test, a relatively narrower and longer serpentine microchannel whose width, depth, and total length were 300 μm, 100 μm, and 1.8 m, respectively, was made on the PDMS side and bonded with flat PMMA. The distance between each parallel microchannel was 100 μm. This was performed to observe whether the narrow space between each channel affected the bonding.

Results and discussion

Contact angle measurement

To confirm the success of surface modification, water contact angles were measured at various stages of surface modification as shown in Fig. 2. Among the fifteen non-silicon substrates examined in this study, we selected four candidates – PVC, PET, Al, and Cu.

As shown in Fig. 2, the water contact angles of pristine PVC, PET, Al, and Cu were measured to be approximately 72.0°, 75.0°, 85.4°, and 74.7°, respectively. After instantaneous treatment with 2% MPTMS on pristine PVC, PET, Al,

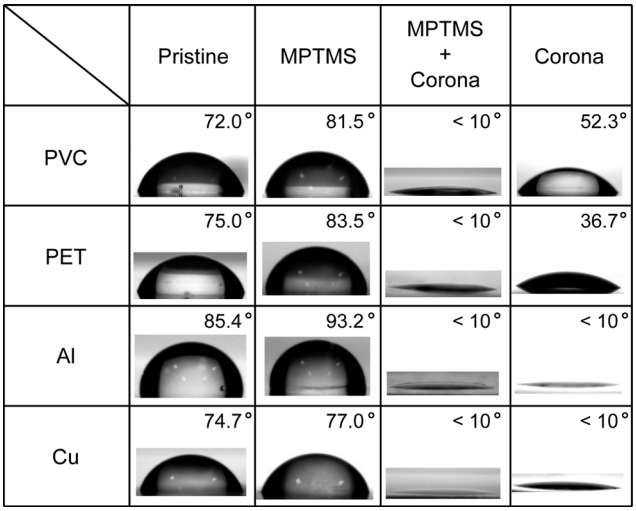

Fig. 2 Measurements of water contact angles of PVC, PET, Al, and Cu at various stages of surface modification. Water contact angles were measured on pristine substrates, MPTMS-treated substrates, MPTMS-coated substrates further treated with corona discharge, and corona-treated pristine substrates.

and Cu at room temperature, the corresponding water contact angles increased to 81.5°, 83.5°, 93.2°, and 77.0°, respectively, presumably because of the formation of hydrophobic alkoxy groups on the surface. Since the alkoxy group can be easily oxidized, the MPTMS treated surface displayed less than 10° in the water contact angles of all four substrates, after corona treatment. As a reference, we also measured the water contact angles after corona treatment of the pristine substrates. As shown in Fig. 2, the water contact angles decreased to 52.3° and 36.7° for PVC and PET, respectively. The decrease in the water contact angle values was not as significant as those with MPTMS coating step added, which implies that MPTMS coating is responsible for the successful hydroxylation of the substrate.

XPS analysis

Fig. 3 shows the results of XPS analyses performed on PVC,[29–31] PET,[32] Al, and Cu.[33]

Fig. 3a, c, e, and g show the elemental peaks of the pristine substrates, all of which basically contain C1s and O1s peaks. Cl peaks, which are characteristic of PVC, appeared as shown in Fig. 3a. Al and Cu peaks appeared for Al and Cu substrates, respectively, as shown in Fig. 3e and g. After surface modification with MPTMS, additional peaks of silicon and sulfur atoms such as Si2p, Si2s, S2p, and S2s, characteristic of mercaptosilane, appeared at approximately 101, 152, 164, and 242 eV, respectively, representing successful modification of the various non-silicon-based substrates with MPTMS.[34–36] These values corresponded well with previous references reporting the binding energies of each element peak. Besides these four substrates, XPS analyses were also performed on PMMA, PC, PS, PI, and PP, and the results are shown in Fig. S1 in the ESI.† In addition to performing XPS analyses, we also measured the surface roughness before and

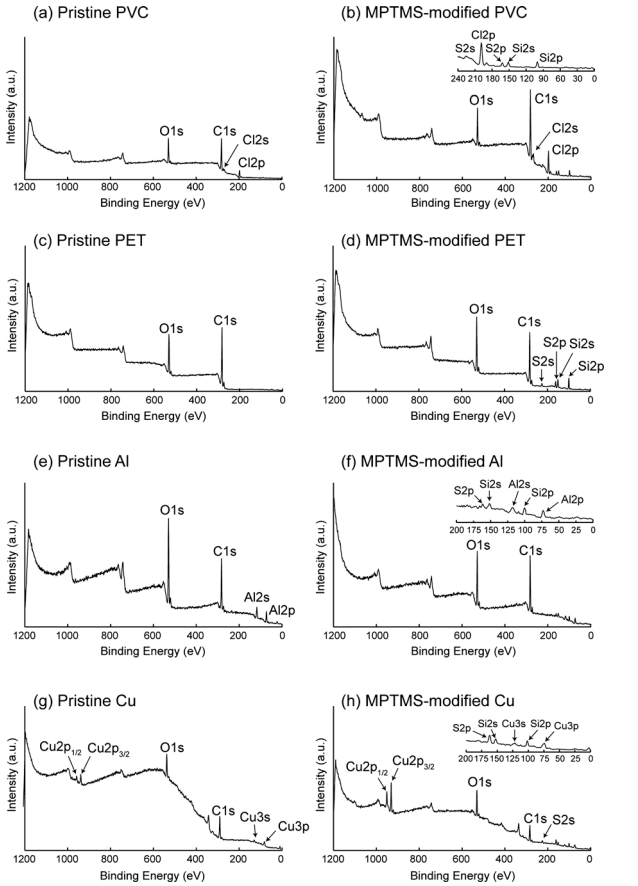

Fig. 3 Results of XPS analyses performed on PVC, PET, Al, and Cu. (a) Pristine PVC. (b) MPTMS-modified PVC. (c) Pristine PET. (d) MPTMS-modified PET. (e) Pristine Al. (f) MPTMS-modified Al. (g) Pristine Cu. (h) MPTMS-modified Cu.

after coating PMMA with mercaptosilane, using an atomic force microscope (AFM). As shown in Fig. S2 in the ESI,† the surface roughness of PMMA increased relatively homogeneously to approximately 30 to 50 nm, over the entire surface of the scanned area, which was 10 μm. Nevertheless, the measured height of the coated mercaptosilane was incomparably low so as not to disturb the bonding of the microchannel with small dimensions.

Bond strength analysis (1): delamination and pull tests

Fig. 4 shows the results of delamination tests performed on thirteen substrates including PET, urethane functionalized PET (U-PET), PVC, PP, PS, aluminum foil, brass, Cu, Fe, PI, PVC copolymer, alumina (α-Al_2O_3), and zirconia (3Y-ZrO_2). MPTMS can easily undergo nucleophilic reaction not just with thermoplastics, but also with metals containing unsaturated outer electrons such as Al, Cu, and Fe, as well as alloys such as brass, and even ceramics such as alumina (α-Al_2O_3) and zirconia (3Y-ZrO_2). As shown in Fig. 4, all thirteen substrates were successfully bonded with PDMS using the method introduced in this study. The water contact angles of pristine Al and Cu both decreased to less than 10° even without MPTMS coating step added because metals can be readily

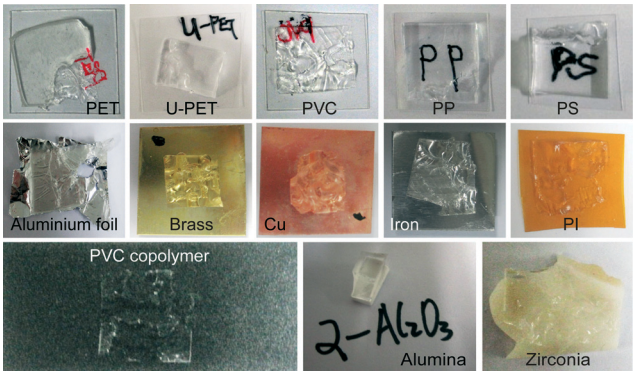

Fig. 4 Results of delamination tests performed on thirteen substrates including PET, U-PET, PVC, PP, PS, aluminum foil, brass, Cu, Fe, PI, PVC copolymer, alumina (α-Al_2O_3), and zirconia (3Y-ZrO_2).

hydroxylated (Fig. 2). Nevertheless, the hydroxylated substrates failed to directly react with the corona-treated PDMS, which was confirmed by the complete detachment of the two substrates (data not shown).

Pull tests were performed on four thermoplastics (PMMA, PET, PVC, and PC) and two metals (Al and Cu). The bond strength of PDMS–PMMA, PDMS–PET, PDMS–PVC, PDMS–PC, PDMS–Al, and PDMS–Cu assemblies were measured to be approximately 335.9, 476.4, 467.3, 511.4, 282.2, and 236.7 kPa, respectively. These values were higher than previously reported methods, which displayed 180 kPa and 178 kPa for PDMS–PMMA and PDMS–PC assemblies, respectively.[18] Fig. 5a shows the photo of the experimental procedure for performing the pull test. Fig. 5b–g show the results of pull tests performed on PMMA, PET, PVC, PC, Al, and Cu, respectively, bonded with PDMS, indicating that permanent bonds were realized. Using this method, miniaturized electronic components such as the membrane, microelectrode, or microheater can be permanently assembled readily and rapidly into a microfluidic system.

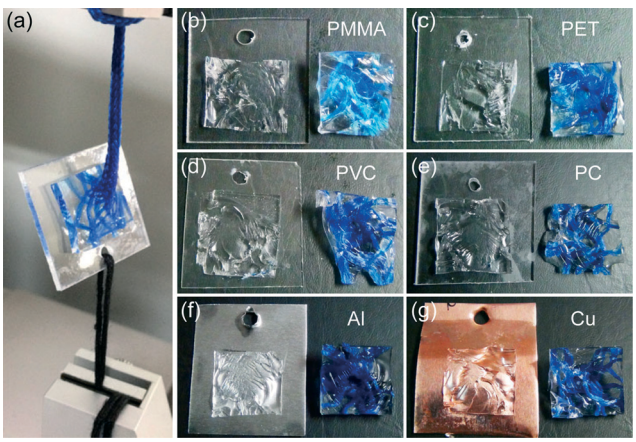

Fig. 5 (a) A photo showing the experimental procedure for performing the pull test. (b–g) Results of pull tests: (b) PDMS–PMMA, (c) PDMS–PET, (d) PDMS–PVC, (e) PDMS–PC, (f) PDMS–Al, and (g) PDMS–Cu.

All the non-silicon substrates used in this study contain electrophilic groups as their components. For example, pristine thermoplastics contain electrophilic carbonate or carbonyl groups. The pristine metals, alloy, and ceramics have electrophilic unsaturated outer electrons or transition metals. Since these electrophilic groups have common chemical properties, they can all react with the same reactive group, the mercapto functionality, during the surface modification process using MPTMS, and the resulting terminal alkoxy groups can be readily oxidized to bond with oxidized PDMS by forming a robust siloxane (Si–O–Si) bond at the interface. This method was tested over two-year time courses to eliminate the effect of ambient temperature and humidity which vary seasonally. The results turned out to be highly reproducible irrespective of the atmospheric conditions. The wide range of the applied concentration of the mercaptosilane solution such as between 1 and 10% verifies the high reliability and stability of the coating method introduced in this study.

Bond strength analysis (2): leak test

Fig. 6 shows the results of the two kinds of leak tests performed in this study. Fig. 6a and b show the results of THF introduction into the PDMS–PVC assembly. We chose THF since it can swell PDMS, so that the volume of the PDMS could change which could possibly lead to leakage if the bonding is not robust. For better visualization of THF flow inside the microchannel, it was colored with black ink. When THF was kept inside the microchannel for 25 min, neither noticeable swelling of the PDMS nor leakage was observed (Fig. 6a). However, after keeping THF inside the microchannel for up to 8 h without taking out THF from the microchannel, noticeable swelling of PDMS took place (Fig. 6b).

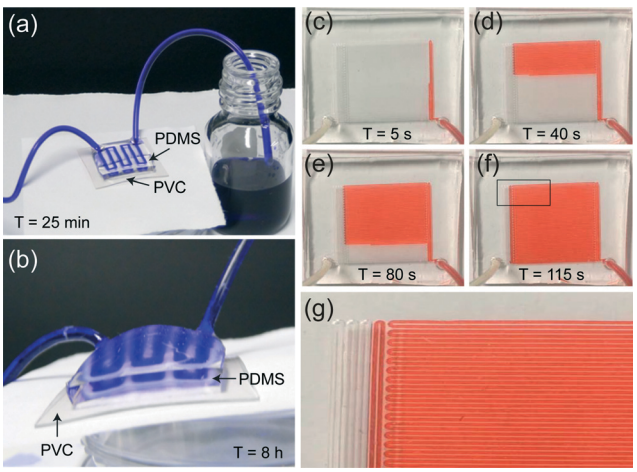

Fig. 6 Results of the two kinds of leak tests. (a–b) Introduction of THF, which was colored with black ink, into the PDMS–PVC assembly and observation of channel leakage for (a) 25 min and (b) 8 h. (c–g) Introduction of red ink solution into the PDMS–PMMA assembly and observation of channel leakage at (c) 5 s, (d) 40 s, (e) 80 s, and (f) 115 s. (g) shows the enlarged image of the rectangle shown in (f).

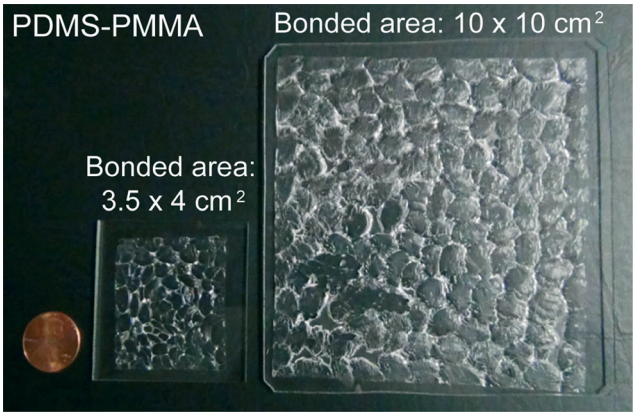

Fig. 7 Results of large area bonding between PDMS and PMMA.

Nevertheless, leakage did not take place, confirming the robust bonding between PVC and PDMS. The deformed PDMS did not return back to its original shape when we observed the bonded assembly for several months. This is probably because the THF molecules were trapped inside the PDMS without being released.

Fig. 6c–g show the results of red ink introduction into the PDMS–PMMA assembly, engraved with a dense serpentine microchannel network, immediately after bonding PDMS and PMMA. The flow rate was relatively fast so that the red ink flowed out of the 1.8 m-long serpentine microchannel within 3 min. No leakage occurred inside the microchannel, confirming the instantaneous and robust bonding between PDMS and PMMA. A 6-fold fast-mode movie clip demonstrating this experiment is demonstrated in Movie S2 in the ESI.†

Large area bonding

The feasibility and robustness of the introduced bonding strategy were further examined by preparing relatively large sizes of the substrates as shown in Fig. 7. We examined the bonding between PMMA and PDMS by cutting one PMMA into 5 × 5 cm^2 and its partner PDMS into 3.5 × 4 cm^2, and another PMMA into 11 × 11 cm^2 and its partner PDMS into 10 × 10 cm^2. As shown in Fig. 7, both assemblies were permanently bonded on the entire surface after surface modification of PMMA with 2% (v/v) MPTMS at room temperature for 1 min followed by corona treatment for 2 min and then bonding at room temperature for 10 min, which was exactly the same condition for bonding small sized substrates, only that the chemical treatment time was increased to 1 min to ensure homogeneous coating. These results revealed once again the high reliability of the bonding strategy introduced in this study.

Conclusion

The mercaptosilane-mediated chemical modification method introduced in this study can become a facile and robust approach for bonding elastomeric PDMS with various non-silicon substrates, which is intrinsically difficult to realize simply by surface oxidation followed by thermal bonding. This method is fast, requires a room temperature process for both surface modification and bonding, and universally applicable to a wide range of non-silicon materials such as thermoplastics, metals, alloys, and ceramics, drawing a lot of attention also from the experts in electronics, materials science, and mechanical engineering. To the best of our knowledge, this is the first study reporting instantaneous and highly stable bonding of PDMS with a wide range of non-silicon substrates, with total process time within 12 to 17 min.

Acknowledgements

This research was supported by Basic Science Research Program through the National Research Foundation of Korea (NRF) funded by the Ministry of Science, ICT & Future Planning (2014R1A1A3051319). This work (Grant No. C0187018) was also supported by Business for Cooperative R&D between Industry, Academy, and Research Institute funded by Korea Small and Medium Business Administration in 2014.

Notes and references

1 G. M. Whitesides, *Lab Chip*, 2013, **13**, 11–13.
2 M. Baker, *Nature*, 2011, **471**, 661–665.
3 A. D. Tadmor, E. A. Ottesen, J. R. Leadbetter and R. Phillips, *Science*, 2011, **333**, 58–62.
4 Y. Xia and G. M. Whitesides, *Angew. Chem., Int. Ed.*, 1998, **37**, 550–575.
5 W. Wu, K. T. L. Trinh and N. Y. Lee, *Analyst*, 2012, **137**, 2069–2076.
6 W. Wu, K.-T. Kang and N. Y. Lee, *Analyst*, 2011, **136**, 2287–2293.
7 W. Wu, K. T. L. Trinh and N. Y. Lee, *Analyst*, 2012, **137**, 983–990.
8 G. M. Whitesides, *Nature*, 2006, **442**, 368–373.
9 I. R. G. Ogilvie, V. J. Sieben, B. Cortese, M. C. Mowlem and H. Morgan, *Lab Chip*, 2011, **11**, 2455–2459.
10 B. Cortese, M. C. Mowlem and H. Morgan, *Sens. Actuators, B*, 2011, **160**, 1473–1480.
11 H. Hwang, H.-H. Kim and Y.-K. Cho, *Lab Chip*, 2011, **11**, 1434–1436.
12 S. G. Im, K. W. Bong, C.-H. Lee, P. S. Doyle and K. K. Gleason, *Lab Chip*, 2009, **9**, 411–416.
13 J. Xu and K. K. Gleason, *Chem. Mater.*, 2010, **22**, 1732–1738.
14 K. Aran, L. A. Sasso, N. Kamdar and J. D. Zahn, *Lab Chip*, 2010, **10**, 548–552.
15 K. S. Lee and R. J. Ram, *Lab Chip*, 2009, **9**, 1618–1624.
16 P. Gu, K. Liu, H. Chen, T. Nishida and Z. H. Fan, *Anal. Chem.*, 2011, **83**, 446–452.
17 V. Sunkara, D.-K. Park, H. Hwang, R. Chantiwas, S. A. Soper and Y.-K. Cho, *Lab Chip*, 2011, **11**, 962–965.
18 L. Tang and N. Y. Lee, *Lab Chip*, 2010, **10**, 1274–1280.
19 M.-E. Vlachopoulou, A. Tserepi, P. Pavli, P. Argitis, M. Sanopoulou and K. Misiakos, *J. Micromech. Microeng.*, 2009, **19**, 015007.
20 M. Jang, S. Park and N. Y. Lee, *Sens. Actuators, A*, 2014, **206**, 57–66.

21 N. Y. Lee and B. H. Chung, *Langmuir*, 2009, **25**, 3861–3866.
22 J. Wu and N. Y. Lee, *Lab Chip*, 2014, **14**, 1564–1571.
23 J. Kim, R. Surapaneni and B. K. Gale, *Lab Chip*, 2009, **9**, 1290–1293.
24 M. Rafat, D. R. Raad, A. C. Rowat and D. T. Auguste, *Lab Chip*, 2009, **9**, 3016–3019.
25 M. J. Lee, N. Y. Lee, J. R. Lim, J. B. Kim, M. Kim, H. K. Baik and Y. S. Kim, *Adv. Mater.*, 2006, **18**, 3115–3119.
26 M. Jang, C. K. Park and N. Y. Lee, *Sens. Actuators, B*, 2014, **193**, 599–607.
27 V. Sunkara and Y.-K. Cho, *ACS Appl. Mater. Interfaces*, 2012, **4**, 6537–6544.
28 K. Haubert, T. Drier and D. Beebe, *Lab Chip*, 2006, **6**, 1548–1549.
29 K. Artyushkova and J. E. Fulghum, *Surf. Interface Anal.*, 2001, **31**, 352–361.
30 L. M. Matuana, J. J. Balatinecz and C. B. Park, *Polym. Eng. Sci.*, 1998, **38**, 765–773.
31 D. J. Balazs, K. Triandafillu, P. Wood, Y. Chevolot, C. van Delden, H. Harms, C. Hollenstein and H. J. Mathieu, *Biomaterials*, 2004, **25**, 2139–2151.
32 A. Vesel, M. Mozetic and A. Zalar, *Vacuum*, 2008, **82**, 248–251.
33 G. Deroubaix and P. Marcus, *Surf. Interface Anal.*, 1992, **18**, 39–46.
34 Y. Yu, J. Addai-Mensah and D. Losic, *J. Nanosci. Nanotechnol.*, 2011, **11**, 1–8.
35 J.-H. Park, Y.-G. Lee and S.-G. Oh, *J. Ceram. Process. Res.*, 2011, **12**, 456–461.
36 S. S. Kim, J. E. Park and J. Lee, *J. Appl. Polym. Sci.*, 2011, **119**, 2261–2267.

Electronic Supplementary Material (ESI) for Lab on a Chip.

Electronic Supplementary Information

Instantaneous room temperature bonding of a wide range of non-silicon substrates with poly(dimethylsiloxane) (PDMS) elastomer mediated by a mercaptosilane

*Wenming Wu, Jing Wu, Jae-Heon Kim, and Nae Yoon Lee**

Department of BioNano Technology, Gachon University, 1342 Seongnam-daero, Sujeong-gu, Seongnam-si, Gyeonggi-do, 461-701, Korea

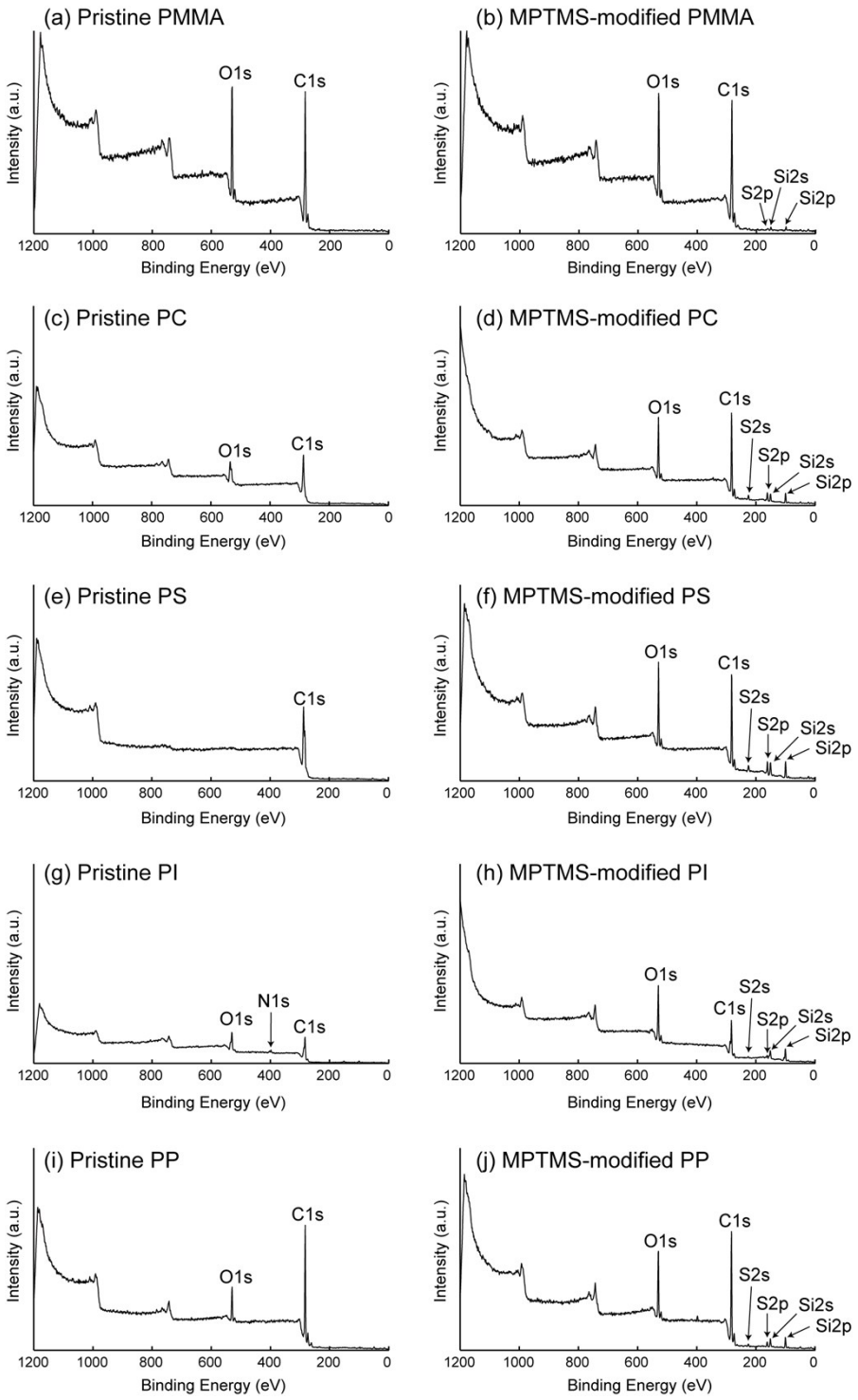

Fig. S1 Results of XPS analyses performed on PMMA, PC, PS, PI, and PP.

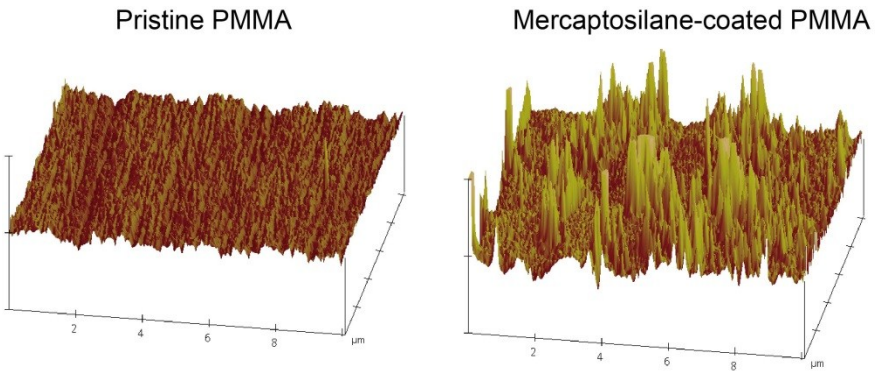

Fig. S2 Results of surface roughness measurement before and after coating PMMA with mercaptosilane, using atomic force microscope (AFM). The scanned area was 10 μm, and one scale of the Y-axis represents 30 nm.

3.3 Wu *et al.* (2016)

Wenming Wu, Rosanne M. Guijt, Yuliya E. Silina, Marcus Koch, and Andreas Manz, "Plant leaves as templates for soft lithography" RSC Adv., 2016, 6, 22469–22475. (SCI indexed, IF = 3.840) **(First author)**

Authorship Contributions

Wenming Wu: participate in research design, conduct experiments, perform data analysis, and write the manuscript
Rosanne Guijt： SEM experiment plan, modify the manuscript
Yuliya Silina: AFM and headspace analysis
Marcus Koch: elasticity measurements and interpretation of results
Andreas Manz: participate in research design, evaluation of results, and modify the manuscript

This work affirms diffusion pump as an efficient approach in liquid injection in novel leaf-inspired microdevice for self-pumped flow analogy of biomimetic microvasculature.

Here I introduce a simple approach to fabricate bio-inspired microdevices depending on direct replication from plant leaves. By simply selecting different venations, my method can easily fabricate different microstructural categories, without the use of any costly reagent, clean room or expensive machine indispensable in photolithography and inkjet printing. With respect to conventional manufacturing techniques, an artificial mask or master mold must be predesigned before fabrication of the microchips. In contrast, my method detracts from this traditional framework because the microstructure can be directly fabricated here based on various natural templates such as plant leaves, insect wings, fish scales, etc. By waiving the fabrication step of the artificial mask and master mold, this

method can dramatically decrease the cost, time, and labor required in fabricating microchips, and thus, is a practical project that can be undertaken in ordinary chemistry or biology labs.

This is the first time that highly consistent micro-structures from a natural template can be so quickly and easily replicated into a microdevice. Because a natural leaf template is directly utilized for microstructural definition, herein truly 3D (varied microchannel height all through the network) vascular structure is reproduced with the surface topography of the leaves also replicated, resulting in complex structured channel surfaces that may offer a much more realistic microenvironment for Lab-on-a-Chip based cell assays. The natural leaves utilized can be used over 50 times without dramatic decline in structure.

It is known that the diffusion- and evaporation-based gas-molecules' exchange between the stomata (CO_2, O_2, and H_2O, etc.) and atmosphere facilitates the self-powered hydraulic flux of leaves. To investigate this mechanism, I further fabricated three PDMS leaves containing different networks of characteristic spacing and ordered hierarchy. Through the usage of diffusion pump, I analogize molecule-diffusion resulted self-pumped hydraulic flow in leaves, monitored in real time and takes into account both factors: "evaporation-induced liquid flow" and "hydraulic behavior in microvascular networks". There are two key attributes of vascular design within leaves: one is to ensure that all portions of the leaf are adequately supplied by the long-term optimized microvascular geometry and properly distributed stomata; while the other is to ensure the hydraulic conductance or liquid potential inside the microvascular channels is as high as possible by a highly ordered network hierarchy. As shown in Fig. 6, through real-time monitoring of the hydraulic flow inside the microvascular networks, I can evaluate the dynamic conductance in real time, covering all bifurcating channels ranging from highest order to lowest order. It is observed that in all three artificial leaves in Fig. 7, if the bifurcating channels share the same order, the flowing-out time is always the same. The average flow rate in the 1^{st}-ordered microchannels and

2^{nd}-ordered microchannels are 0.08 mm/sec (n=1) and 0.04 mm/sec (STDV, n=16) for Carpinus betulus, 0.16 mm/sec (STDV, n=5) and 0.11 mm/sec (STDV, n=7) for Aegopodium podagraia, and 0.45 cm/sec (STDV, n=5) and 0.22 cm/sec (STDV, n=10) for Tilia platyphyllos. Based on such flow analysis inside PDMS leaves using the same method, I can see average flow rate through first-ordered microchannels is 1.5-2.2 times faster than average flow rate in the second order channels, ranging from Aegopodium podagraia, Carpinus betulus and Tilia platyphyllos leaves. This indicates that the hydraulic potential and conductivity are directly correlated with the order of the microchannel, which ensures that all bifurcating channels of the same order gain identical liquid transportation ability in order to avoid the under-support or over-supply of any cells in leaves.

Due to the direct structure replication method I posit, my method can provide a solid foundation for understanding various natural microvascular networks in plants, animals, and microorganisms using a "micro Total Analysis System". Even if I only show one application example for the analogy of hydraulic transportation in the venation system, I nevertheless believe my method can initiate many microvascular-related research through the "micro Total Analysis System". Furthermore, many additional advantages associated with my method may emerge because the microchannels fabricated here are based on direct structural replication and modification from natural leaves in the "micro Total Analysis System", but not from the traditional technique which is cost-ineffective, time-consuming, labor-intensive, and financially impractical to ordinary labs.

RSC Advances

COMMUNICATION

View Article Online
View Journal | View Issue

Cite this: *RSC Adv.*, 2016, **6**, 22469

Plant leaves as templates for soft lithography†

Wenming Wu,[ab] Rosanne M. Guijt,[c] Yuliya E. Silina,[d] Marcus Koch[d] and Andreas Manz*[ab]

Received 4th December 2015
Accepted 10th February 2016

DOI: 10.1039/c5ra25890a

www.rsc.org/advances

We report a simple fast, practical and effective method for the replication of the complex venation patterns of natural leaves into PDMS with accuracy down to a lateral size of 500 nm. Optimising the amount of crosslinker enabled the replication and sealing of the microvascular structures to yield enclosed microfluidic networks. The use of plant leaves as templates for soft lithography was demonstrated across over ten species and included reticulate, arcuate, pinnate, parallel and palmate venation patterns. SEM imaging revealed replication of the plants microscopic and sub-microscopic topography into the PDMS structures, making this method especially attractive for mimicking biological structures for *in vitro* assays. Flow analysis revealed that the autonomous liquid transport velocity in 1st-order microchannel was 1.5–2.2 times faster than that in the 2nd-order microchannels across three leaf types, with the sorptivity rule surprisingly preserved during self-powered flow through leaf-inspired vascularity from *Carpinus betulus*.

Biological microstructures have long been a source of inspiration for artists and scientists.[1] In engineering, biomimetic approaches have enabled the systematic study of nature-derived nano-, micro- and macroscopic structures. Perhaps most famous is the discovery of superhydrophobicity mimicking[2] the nano-microscopic surface morphology of the natural-leaf templates, such as *Strelitzia reginae*,[3,4] taro,[5] lotus and rice leaves.[6,7] Superhydrophobic surfaces have been utilized in a myriad of technological applications including anti-wetting[8,9] bubble bursting,[10] organic-proofing,[11] directional transportation,[12] antifogging,[13] superhydrophobicity–superhydrophilicity transition,[14,15] self-cleaning,[16–18] self-repairing interfaces.[19,20]

The diversity and organization of microvascular structures from plants has drawn significant attention, inspiring solutions in engineering modeling,[21] paleoecology hindcasting,[22] low-noise microelectronics,[23] thermal distribution,[24] the design of durable wind turbines,[25] green energy,[26] *etc.* Recent research revealed that both radius tapering and the ratio of daughter to parent branch areas in leaf veins are in strong agreement with Murray's law, and hence resemble the circulatory and respiratory systems.[27] In both cases, the sum of the cubes of each-order veins is conserved throughout the flow network.[28] This correlation provides great opportunities for leaf-inspired microfluidic devices in the creation of bio-realistic *in vitro* models. By selecting different venation types including reticulate, arcuate, parallel, pinnate and palmate, we foresee leaf-inspired microfluidic devices can be utilized for various applications, *e.g.*, cancer metastasis, microparticle separation, capillary electrophoresis and 3D microvessel engineering, *etc.*

Almost twenty years ago, microfluidic fabrication was revolutionised by the introduction of polydimethylsiloxane (PDMS) for casting from microstructured templates.[29] PDMS has become the most widely adopted material in fabricating microdevices[30–33] thanks to its ease of use, optical transparency and biocompatibility. The templates used for casting have ranged from structures made in multilayer tape,[34] SU-8 or other photoresists like Norland Optical Adhesive (NOA),[35] 3D printed resin,[36] printed circuit boards, or by simply gluing capillaries and other structures onto a substrate (*e.g.*, PMMA).[35,37]

Traditional fabrication techniques including inkjet printing, photolithography and chemical etching have all been used to produce "leaf inspired" microchannels.[38–40] Prof. A. Lewis' group printed a fugitive organic ink according to the microvasculature of ivy leaves.[36] After casting epoxy matrices, the ink could be removed at 80 °C under light vacuum, leaving a microvascular fluidic network. Other reports were based on traditional photolithography and soft lithography technologies to produce an SU-8 master for further replication into gel[38] or PDMS.[39] Photomasks were created by depositing chromium onto a leaf skeleton obtained by alkaline removal of the soft

[a]*Mechatronics Department, University of Saarland, Germany*
[b]*KIST Europe GmbH, 66123, Saarbrücken, Germany. E-mail: manz@kist-europe.de*
[c]*School of Medicine and ACROSS, University of Tasmania, Hobart, Australia*
[d]*INM-Leibniz Institute for New Materials, Campus D2 2, Saarbrücken, Germany*

† Electronic supplementary information (ESI) available. See DOI: 10.1039/c5ra25890a

tissue,[40] which was then used to transfer the microvascular network onto a silicon wafer.

Here we introduce a simpler alternative approach where microfluidic structures are directly replicated from plant leaves. In contrast with other microfabrication techniques, this highly economical approach only utilizes PDMS elastomer for microchip fabrication and eliminates the reliance for costly reagents, *e.g.*, fugitive ink,[36] photoresist,[38] developer[38–40] and corrosive chemicals.[39,40] Furthermore, clean room facilities and microfabrication equipment including inkjet printer,[36] mask aligners,[38–40] CNC milling,[47] or laser ablation are also waived here. Because a natural leaf template is directly utilized for microstructural definition, herein truly 3D (varied microchannel height all through the network) vascular structure is reproduced instead of 2D (same microchannel height all through the network) vascular structure as in previous reports.[36,38–40] Unlike other "leaf inspired" microfabrication techniques,[38–40] the surface topography of the leaves is also replicated, resulting in complex structured channel surfaces that may offer a much more realistic microenvironment for Lab-on-a-Chip based cell assays.[41–43] We anticipate this nature-inspired manufacturing methodology may open new opportunities by leading microfluidic based microvascular engineering towards more bio-realistic assays.

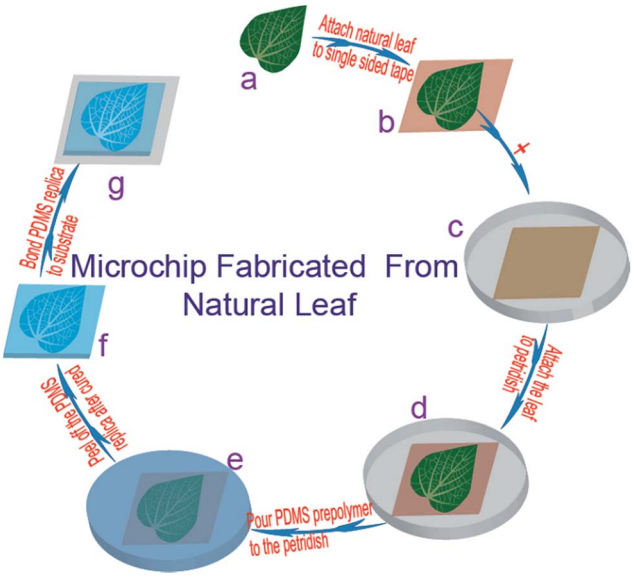

Fig. 1 Schematic steps of the direct replication of microvascular networks from natural leaves into a microfluidic PDMS device. The natural leaf (a) attached to single-sided tape (b) is mounted onto a Petridish (d) using double sided tape (c). The PDMS pre-polymer is poured over the leaf and cured (e) before the PDMS replica is removed (f). An enclosed microchannel is formed by sealing the PDMS replica with a glass or PDMS substrate after oxygen plasma treatment (g). The biomimetic chip is placed in an oven at 80 °C for 2 hours in order to stabilize bonding strength (g).

Experimental

Microchip fabrication

A schematic overview of the main steps in the use of plant leaves as templates for soft lithography is schematically depicted in Fig. 1. Leaves were removed from plants and rinsed under running water for one minute, and gently wiped using laboratory paper and blow dried using a N_2. On the same day, the leaf was attached to single-sided tape (Tesa 57176-00 Tesapack ultra-strong tr. 66 m: 50 mm wide) and then to a disposable Petri dish (Mit 3 Nocken Ø 90 mm, 391-0247) using double-sided tape (Tesa double side tape 10 m: 15 mm wide). PDMS (SYLGARD 184; Dow Corning, USA) was prepared by carefully mixing the PDMS prepolymer and cross linker in a 20 : 1 ratio, and degassed for 1 h in a vacuum desiccator to remove air bubbles. When pouring the PDMS into the Petri dish containing the leaf, any possible bubbles formed could automatically disappear after few minutes. The PDMS was cured in an oven (Binder, US PATS 4585923) at 45 °C for 24 h (Fig. 1f).

Next, the PDMS replica was cut using a box cutter and peeled off the template. The template was again covered with PDMS to protect it for further structure replication. An oxygen plasma system (Diener electronic: 0010915) was used to activate the surfaces of both PDMS replica and glass or PDMS substrates before bonding. Finally, the assembled devices were placed in the oven at 80 °C for two hours to increase bonding strength. Images of leaves templates were taken using a consumer CCD camera (Canon ED560D with macro-lens).

Pressure-driven flow

A 5 mL disposable syringe was utilized to fill the microfluidic network. The syringe was filled with 2.5 mL of red ink (WATERMAN Fountain Pen Ink, Audacious Red S0110730) before the piston was withdrawn to the 4.3 mL mark. A 2 mm diameter inlet was punched in the PDMS replica of a leaf to connect with the central vein and connected with silicone tubing, sealed in place using uncured PDMS. A pipette tip (1–200 μL, UltraFine™, graduiert, VWR International GmBH) was used to connect the filled syringe with the microfluidic network. The system was pressurized by pushing the piston from the 4.3 mL mark to the 3.2 mL mark on the syringe, and fixed in this position using a metal wire (Fig. S6, ESI 1†).

Scanning electron microscopy (SEM)

For correlative SEM analysis of the positive leaf and the negative PDMS replica, a FEI (Hilsboro, OR, USA) Quanta 400 FEG was used. Samples were investigated in low vacuum mode (p = 100 Pa water vapor) at an accelerating voltage of 10 kV using the secondary electron (large field) detector (30 μm final lens aperture size; spot size 3; pixel dwell time 30 μs, image size 1024 × 884 pixels).

Atomic force microscopy (AFM)

For AFM measurements 20 nm gold was sputtered on the PDMS replica to eliminate charging during investigation. A Nanowizard 3 (JPK Instruments, Berlin, Germany) operating in tapping mode was used to reveal the 3D structure of the replicated leaf surface. AFM tips from NANOSENSORS (Neuchatel, Switzerland), type PPP-NCLR were used for height measurements.

Elastic modulus (*E*-modulus) of PDMS templates

Varying the degree of crosslinking in the polymer network allows tuning its mechanical properties in a wide range. To estimate mechanical properties of PDMS produced with different amount of crosslinking from the each of flat templates a cylinder with a 3 mm diameter was cut for the subsequent compression test performed under 25 °C with a TA DMA Q 800 instrument (TAINSTRUMENT, Eschborn, Germany).

Head-space gas chromatography mass spectrometry

(HS-GC-MS). To verify the chemical stability of the produced PDMS templates HS-GC-MS analysis was performed. A gas sample of 500 μL at 50, 70 and 100 °C from the headspace above the sample (0.15 g) (5 min incubation time; agitator speed, 500 rpm; fill speed, 100 μL s^{-1}; injection speed, 500 μL s^{-1}) was injected by a PAL auto sampler (CTC Analytics, Zwingen, Switzerland) into the QP5050 (Shimadzu, Japan) GC-MS system. A Phenomenex (Torrance, CA, USA) ZB-WAX-plus column (30 m × 0.25 mm; film thickness 0.25 μm) was utilized for separation. An injection temperature of 200 °C (split ratio 1 : 35) was used, with the temperature program kept at 50 °C for 1 min, then raised to 200 °C at 20 K min^{-1} and held at the final temperature 250 °C for 5 min. The column inlet pressure was adjusted to 100 kPa, giving a flow rate of 1.7 mL min^{-1}. The transfer line to the mass spectrometer and the source temperatures were 230 °C and 200 °C, respectively. Electron ionization (70 eV) mass spectra were recorded in the *m*/*z* range of 40–920.

Results and discussion

Leaf-inspired microfluidic devices

There is a large variation in the size, geometry and venation between leaves from different plant species, and in this work, leaves from *Tilia platyphyllos*, *Prunus cerasifera*, *Viburnum davidii*, *Prunus avium*, *Plantago lanceolate*, *Carpinus betulus*, *Fraxinus excelsior*, *Glechoma hederacea*, *Acer pseudoplatanus* and *Aegopodium podagraia* were all successfully replicated in PDMS.

Examples of leaves and their replicates of a reticulate, arcuate, parallel, pinnate and palmate venation are given in Fig. 2a–j, with close-up images of the microvascular channels in Fig. 2k–o. More information about microchip fabrication from other leaves is also added to Fig. S1 (ESI 1†). The widths of the first ordered channels were measured to be 0.54 mm, 0.81 mm, 1.20 mm, 0.82 mm and 0.43 mm for *Tilia platyphyllos*, *Aegopodium podagraia*, *Plantago lanceolate*, *Frangula alnus* and *Acer pseudoplatanus* leaves, respectively. Remarkably that, the 1st ordered channel in *Plantago lanceolate* was 2.8 times wider than in *Acer pseudoplatanus*. Across all species, the smallest veins were around 8 μm wide (Fig. S2, ESI 1†), much smaller than previous reports.[39,40] As the replicated vascular structures were copied from the outside of the leaf, internal structures like the phloem and xylem cannot be replicated by means of this method. The vascular geometry and size distribution across the bifurcating channels, however, was maintained as demonstrated by the reduction in channel width moving down from the first order or main vein as shown in Fig. 2k–o.

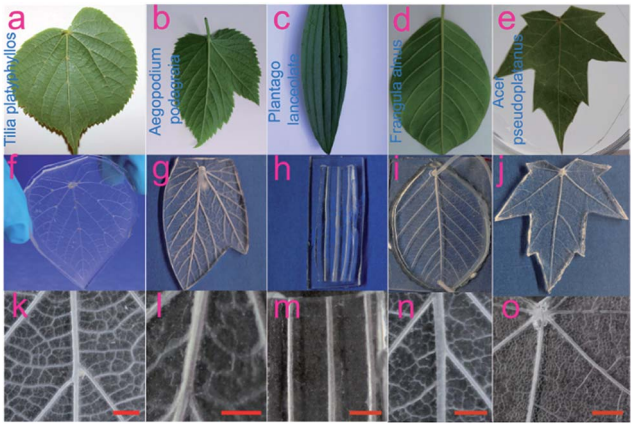

Fig. 2 Diversity in shape and venation in plant leaves. (a–e) Photographs of the fresh leaves; (f–j) photographs of PDMS replicates and (k–o) close-ups of the first order vein of *Tilia platyphyllos*, *Aegopodium podagraia*, *Plantago lanceolate*, *Frangula alnus* and *Acer pseudoplatanus*. Scale bar images (k–o) corresponds to 2.5 mm.

Optimization of crosslinker : monomer ratio

Initially, the soft lithography experiment was carried out using the standard 1 : 10 crosslinker : monomer ratio, but the obtained structures could not be sealed in a leakage-tight manner to glass or PDMS substrates. This was hypothesized to be due to the stiffness of the PDMS preventing the textured leaf replica from sealing with the flat substrate. It is known that the stiffness of PDMS can be reduced when the amount of initiator reaches 1 : 20 ratio.[44,45] The soft lithography process was repeated using PDMS mixed in 1 : 15, 1 : 20 and 1 : 30 crosslinker : monomer ratios. The templates obtained using over 1 : 30 PDMS ratio were sticky to touch and left residues, indicating that PDMS was not be fully cured even when extending the curing time to days. For this reason PDMS template synthesized with 1 : 30 crosslinker : monomer ratio has been eliminated from the further experiments. The 1 : 20 ratio provided a PDMS template that was softer than the PDMS obtained using the 1 : 10 or 1 : 15 ratio (Table 1).

In addition, PDMS template mixed in 1 : 20 crosslinker : monomer ratio was not sticky and did not leave residues. Moreover, it was important for microfluidic applications because it enabled leakage-tight sealing to flat glass and PDMS substrates.

Whilst a softer PDMS can also be obtained by partially curing the PDMS in a shorter curing time, this is not recommended as it increases the variability. Inspection of incompletely cured

Table 1 *E*-Modulus of PDMS templates with different amount of crosslinking

	Crosslinker : monomer ratios		
	1 : 10 (RSD, %)	1 : 15 (RSD, %)	1 : 20 (RSD, %)
E-Modulus, N mm^{-2}	1.1 (2.1%)	0.6 (0.8%)	0.1 (1.2%)

structures by SEM (*data are not shown*) revealed a highly heterogeneous replication, randomly distributed smooth areas amongst highly structured regions.

Next, PDMS prepared in 1 : 10; 1 : 15 and 1 : 20 ratios were inspected by SEM (Fig. 3). The microscopic images showed that structures obtained under 1 : 20 ratio PDMS have been replicated in greater detail *versus* templates synthesized in 1 : 15 or 1 : 10 ratios. Sub-micron scale structures of *Aegopodium podagraia* leaf (Fig. 3d–f) showed the replication of the hair-like appendages also known as trichomes.

Because both vascularit[21–28] and surface topography[3–20] can play important role for downstream applications, it was considered to be important to not only preserve the vascularity, but also the microscopic topography of the leaf. To reveal the accuracy of the replicated templates (1 : 20 ratio), a stoma of the back side of *Tilia platyphyllos* was chosen. As shown in Fig. 4, the line structure next to the stoma can be replicated with high accuracy down to a lateral size of 500 nm. A penetration depth of 90 μm was also found for *Tilia platyphyllos* replica (Fig. 4d and h). In contrast to this, the nanostructures inside the stoma unfortunately were not replicated into the PDMS using this technique.

On the next step, AFM measurements revealed 3D structure of the replicated leaf of *Tilia platyphyllos* on PDMS. The liner structure next to the stoma was transformed into the PDMS up to a height variation of several hundreds of nanometer (see Fig. S3, ESI 1†). For the depth of a hole of a stoma that was replicated into the PDMS a height of more than 1 μm was found (see Fig. S3, ESI 1†).

Remarkably that produced PDMS replicates (1 : 20 ratio) showed also an excellent chemical stability estimated by HS-GC-MS *versus* pure PDMS matrix that maybe important in the future for bio-applications (for more information see Fig. S4, ESI 1;† HS-GC-MS chromatograms showed for pure PDMS matrix, natural *Tilia platyphyllos* leaf after contact with PDMS and PDMS template after contact with a *Tilia platyphyllos* respectively).

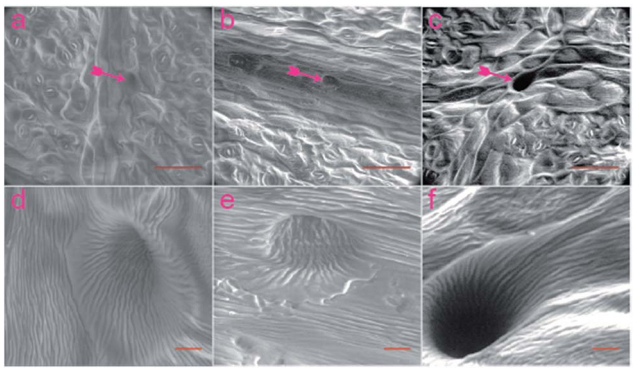

Fig. 3 SEM images of PDMS replica from *Aegopodium podagraia* leaf. (a) PDMS elastomer prepared at 1 : 10. (b) 1 : 15, and (c) at 1 : 20 initiator : monomer ratios. (d) Image of micro-hole in (a). (e) Enlarged image of micro-hole in (b). (f) Enlarged image of micro-hole in (c). Purple arrows represent the position of microholes replicated from trichomes. Scale bars (a)–(c) 100 μm, (d)–(f) 10 μm.

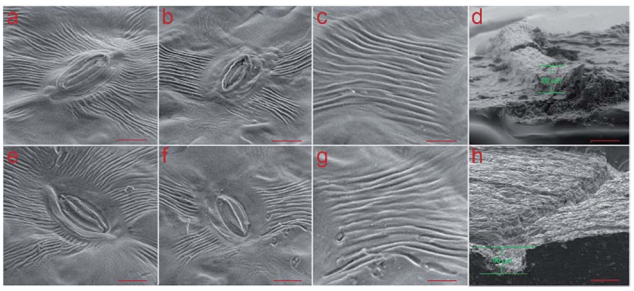

Fig. 4 SEM images of *Tilia platyphyllos* leaf and corresponding PDMS replica. (a)–(d) image of *Tilia platyphyllos* leaf. (e)–(f) PDMS replica from *Tilia platyphyllos* leaf with the same microvascular position in (a)–(d). Scale bars (a), (b), (e) and (f) 10 μm, (c) and (g) 5 μm, (d) and (h) 100 μm.

Influence of the storage conditions of leaves templates on the soft lithography efficiency

Having optimized the casting conditions using *Aegopodium podagrai* and *Tilia platyphyllos* (see above), the fidelity of replication and structural diversity between plant species were studied using *Plantago lanceolate*, *Viburnum davidii*, and *Glechoma hederacea*. SEM images of the original leaves (Fig. 5a–c) confirmed the diversity in surface morphology between the species. The SEM images at low magnification revealed a variety of surface features. Fig. 5d–i confirmed this diversity is transferred into the PDMS replica, with biodiversity in both vascularity and surface topology preserved using plant leaves directly as template in soft lithography. The 800× images showed the stoma, the mouth-like features used for gas exchange, was also replicated well into PDMS. It is well known that cells culture in a more biologically realistic manner on structures that are not smooth but structured. Studies using the PDMS plant replicas in our laboratory have confirmed a more *in vivo*-like migration pattern for human melanoma cells (in submission – LC-TIN-01-2016-000076).

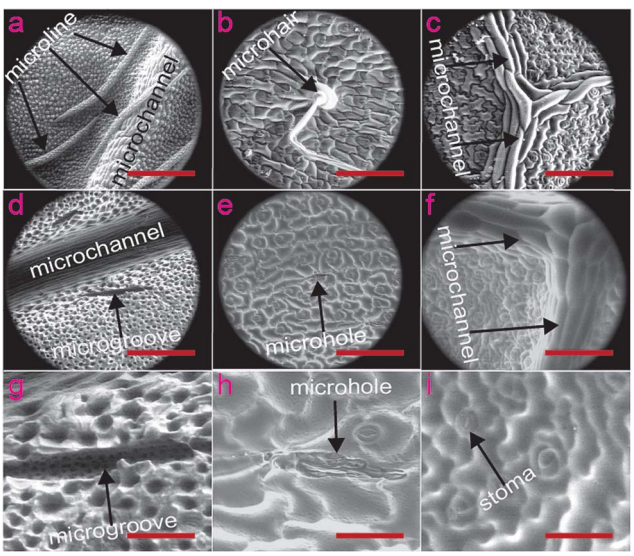

Fig. 5 SEM images of PDMS replica (1 : 20) and real leaf. (a) Leaf-template *Viburnum davidii*. (b) Leaf of *Plantago lanceolate* (c) *Glechoma hederacea* leaf. Scale bars in (a)–(f) 200 μm, (g)–(i) 50 μm.

Whist the biodiversity between leaves provides a wide variety of structures, this means the optimal leaf for a certain bioassay may have to be identified experimentally. Additionally, the precise size and geometry between leaves will vary, which may introduce an unwanted variability between studies conducted with PDMS replicates from different leaves.

To avoid this issue, and the seasonal dependence, the longevity of the templates was investigated. Initially, fresh leaves (processed on the same day they were picked) were used as templates for replication in PDMS to avoid the structural changes as the leaf dehydrates. The template was then again covered with PDMS and stored for up to a year. The *Tilia platyphyllos* template (Fig. 6a) has been replicated into PDMS for at least thirty times over a one year period. The discoloration of the leaves (Fig. 6d) indicates oxidative processes as well as the loss of water through the permeable PDMS. When comparing 'b' and 'e', some shriveling and loss of microscale features can be observed after a year storage, but a surprisingly high level of detail of the microstructures is preserved, as indicated by the SEM images of the stomata (Fig. 6f).

As aforementioned, low heated temperature of 45 °C was required for the curing of PDMS on fresh leaf template to preserve the microscopic structure. In the other case, the template would change color from green to black and microstructures were found to have collapsed. Interestingly, it was found that for aged templates stored over three months, the use of higher temperatures like 70 °C or 80°C could be used for curing PDMS without damaging the template. Whilst creating a daughter template from the first PDMS replica, for example NOA 63 resist,[35] will guarantee uniformity across the replicated structures, the ability to store the templates over an extended period of time adds to the versatility of the approach. Longevity of the *Carpinus betulus* leaf template was also investigated, indicating similar endurance results as *Tilia platyphyllos* leaf (Fig. S5, ESI 1†).

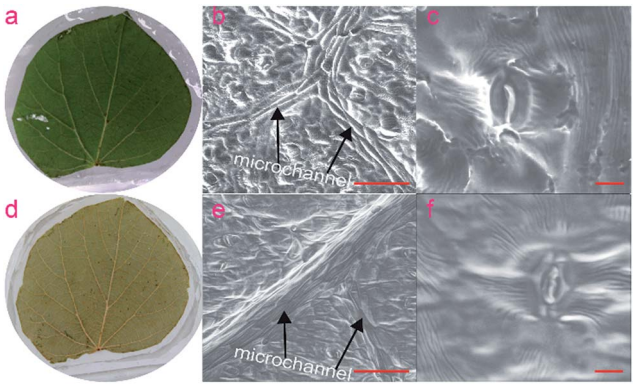

Fig. 6 *Tilia platyphyllos* leaf stored in PDMS for one year, utilized for microfabrication of over thirty times during this period. (a) Photograph of freshly prepared *Tilia platyphyllos* leaf. (b) PDMS replica from fresh *Tilia platyphyllos* leaf showing microvascular structure. (c) Imprint of stomata in PDMS replica from fresh *Tilia platyphyllos* leaf. (d) Photograph of *Tilia platyphyllos* leaf after one year. (e) PDMS replica from 1 year old *Tilia platyphyllos* leaf showing microvascular structure (f) SEM image of PDMS replica of stomata from one year old *Tilia platyphyllos* leaf. Scale bars (b) and (e) 100 μm, (c) and (f) 10 μm.

Flow through vascular network

Water transport is one of the most important function of natural leaves. Noticeably, such complicated process totally depends on self-activated pumping with only one stiped inlet. Inspired by this post, we innovated self-powered autonomous flow inside biomimetic PDMS leaves without the need for access holes other than the inlet, to visually reveal how autonomous flow behaves inside leaves' microvasculature. Similar to real leaves, herein fluidic filling into PDMS leaves was totally self-activated, and thus, requiring very low energy[46–48] consumption.

Assuming the air in the syringe behaves as an ideal gas, Boyles law $P_1V_1 = P_2V_2$ can be used to predict the pressure[47,48] applied at the inlet of the microvascular network by compressing the air in the syringe to be approximately 2.6 atm (260 kPa). This pressure can be used to fill the microfluidic network with the ink, using the gas-permeability of PDMS to squeeze the air out. Altogether three PDMS leaves (Fig. 7) were directly replicated from natural leaves (*Tilia platyphyllos*, *Aegopodium podagraia* and *Carpinus betulus*) for flow studies, with significant differences in their microvascular networks. The flow studies were used to compare the hydrodynamic resistance of the 1st and 2nd-ordered channels branching off the main vein (Fig. S6, ESI 1†). Image analysis revealed the average flow rate in the 1st-ordered microchannels and 2nd-ordered microchannels were 0.08 mm s^{-1} ($n = 1$) and 0.04 mm s^{-1} (STDV, $n = 16$) for *Carpinus betulus*, 0.16 mm s^{-1} (STDV, $n = 5$) and 0.11 mm s^{-1} (STDV, $n = 7$) for *Aegopodium podagraia*, and 0.45 cm s^{-1} (STDV, $n = 5$) and 0.22 cm s^{-1} (STDV, $n = 10$) for *Tilia platyphyllos* (Fig. S7, ESI 1†). Based on flow analysis inside PDMS leaves, average flow rate through first-ordered microchannels was 1.5–2.2 times faster than flow rate in the second order channels (ESI 2, 3†), ranging from *Aegopodium podagraia*, *Carpinus betulus* and *Tilia platyphyllos* leaves. The higher flow rate in 1st microchannel than 2nd ordered microchannels, indicates geometrical microvascular configuration in leaves obtained higher overall hydraulic conductivity in first-ordered microchannels. The flow hierarchy used in plant leaves to ensure equal distribution of nutrients was preserved in the PDMS leaves with replicated fluidic structure.

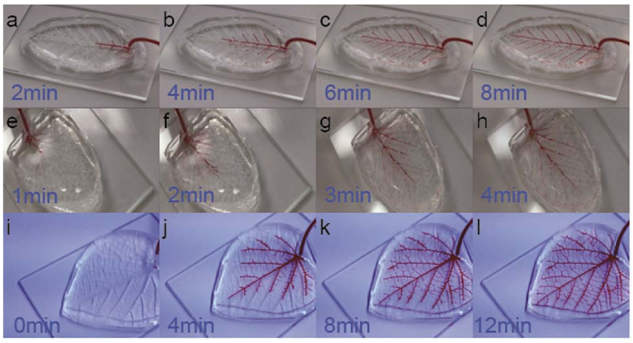

Fig. 7 Hydrodynamic filling of PDMS leaves: (a)–(d) *Carpinus betulus*, (e)–(h) *Aegopodium podagraia*, and (i)–(l) *Tilia platyphyllos*, images were obtained at 2 min, 1 min, and 4 min intervals, respectively.

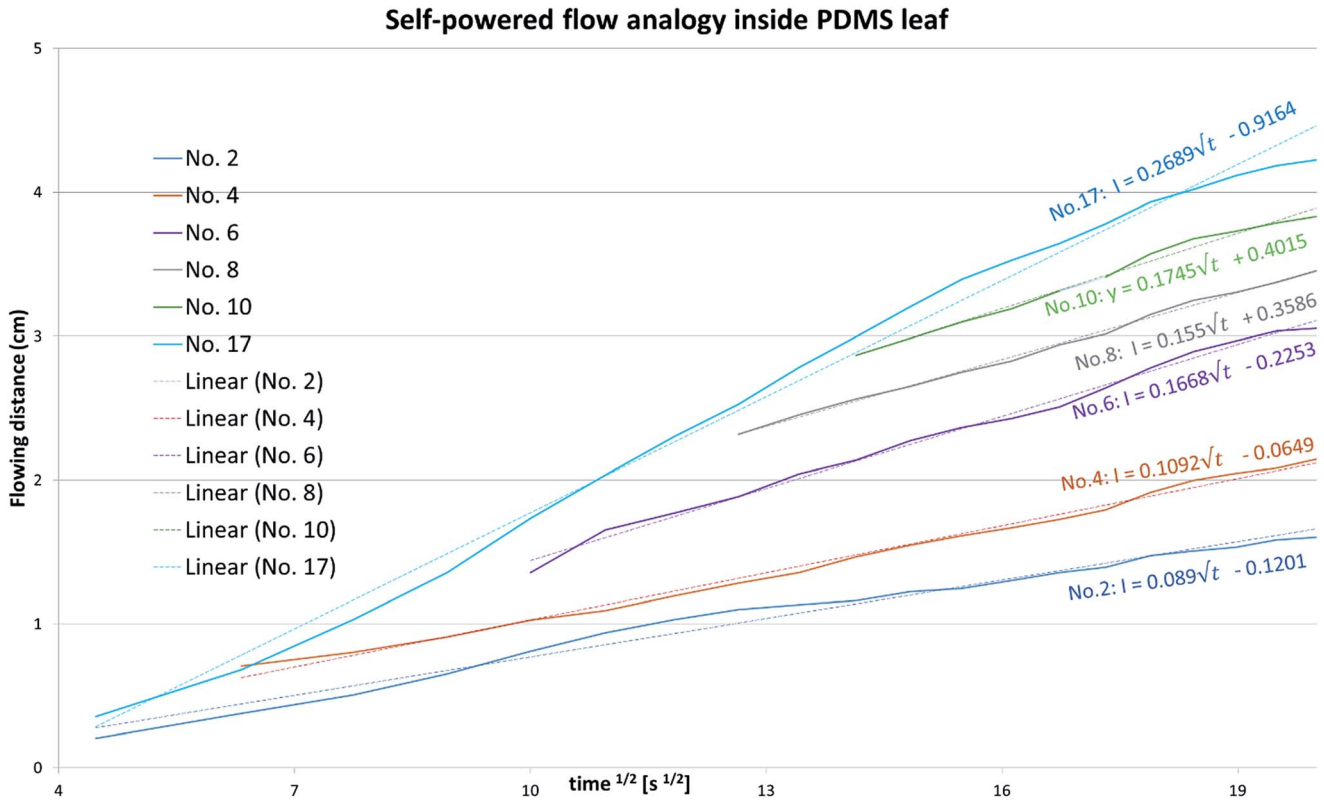

Fig. 8 Quantitative flow analogy inside PDMS leaf containing parallel networks replicated from *Carpinus betulus*, with flowing distance plotted *versus* square root of time.

Total filling time of all three PDMS leaves was less than 10 minutes, indicating suitability for loading medium for static cell culture. Accounting that both plant leaves and animal circulatory systems are nature evolved microfluidic channels[51] obeying Murray's law,[27] plant leaves may become attractive templates to fabricate biomimetic microvascular devices for further animal cell studies.

Further analysis of the flow rate in both the 1st microchannel (no. 17) and 2nd ordered microchannels (no. 2, 4, 6, 8, 10) of PDMS leaf from *Carpinus betulus* (Fig. S8, ESI 1†), also surprisingly showed that the flow in leaf-inspired microvascular channel obeys sorptivity rule,[49,50] which is mostly found in capillary absorption, and can be represented by the following equation,

$$I = S\sqrt{t}$$

where I is the cumulative flow amount, S is sorptivity constant, and t is time.

It's seen from Fig. 8, the flowing distance (amount) in both the 1st microchannel and the 2nd ordered microchannels of PDMS leaf from *Carpinus betulus*, were linearly correlate with the square root of time, obeying sorptivity rule.

Conclusion

A simple method for the replication the venation pattern and microscopic surface morphology – down to a lateral size of 500 nm of plant leaves into PDMS is presented by directly using the leaves as template. The method was applied to leaves from over ten different species, covering the most common reticulate, arcuate, pinnate, parallel and palmate venation patterns. The soft lithography process was optimised by reducing the initiator to monomer ratio from 1 : 10 to 1 : 20 to make a softer PDMS, which allows for a leakage-tight seal with a flat substrate despite the surface topography. Using reversibly bound PDMS on glass devices, no leakages were observed when filling the microfluidic network with pressures up to 260 kPa. Evaluation of the linear flow velocities in 1st and 2nd order microchannels revealed the linear flow rate in the 2nd order channels was about half of that in the 1st order structure, facilitating ordered filling of the leaf. It's surprisingly found here that flow in both 1st and 2nd ordered microchannels of PDMS leaf from *Carpinus betulus*, obeys sorptivity rule that's believed mainly applied to capillary absorption in conventional views. We'll make a deeper study on this discovery in our future work.

With a demonstrated ability to replicate from a wide variety of vascular structures, this methodology provides access to a variety of fluidic structures, with an even larger variety in functionality provided by presence, location and structure of micro- and nanometer scaled structures caused by structures like stomata and trichomes. The surface of leaf-replicated channels is not smooth and may be more bioequivalent than lithographically fabricated structures, with preliminary studies confirming a more *in vivo*-like migration pattern for human

melanoma cells. The variety in three dimensional vascularity and inhomogeneous surfaces offered by this new, simple and affordable approach for biomimetic microfabrication may benefit many *in vitro* cell-based assays.

Acknowledgements

The authors would like to thank Karsten Brill (KIST) for SEM images, Florian Warnke (KIST) for assistance in identifying leaves species, JuYeol Bae (Pusan National University, Korea) for assistance in preparing samples, Sarah Fischer (INM) for Elastic-modulus measurements and Franziska Emmerich (INM) for excellent AFM images. RMG would like to acknowledge the Alexander von Humboldt Foundation for a fellowship.

Notes and references

1 S. Mann, *Biomineralization, Principles and Concepts in Bioinorganic Materials Chemistry*, Oxford University Press, Oxford, 2001.
2 M. Liu, Y. Zheng, J. Zhai and L. Jiang, *Acc. Chem. Res.*, 2010, **43**, 368.
3 E. Mele, S. Girardo and D. Pisignano, *Langmuir*, 2012, **28**, 5312.
4 Z. Yuan, H. Chen, J. Tang, H. Gong and Y. Liu, *J. Phys. D: Appl. Phys.*, 2007, **40**, 3485.
5 C. Liu, *Microfluid. Nanofluid.*, 2010, **9**, 923.
6 W. Zhao, L. Wang and Q. Xue, *J. Phys. Chem. C*, 2010, **114**, 11509.
7 M. Sun, C. Luo, L. Xu, H. Ji, Q. Ouyang, D. Yu and Y. Chen, *Langmuir*, 2005, **21**, 8978.
8 M. Liu, Y. Zheng, J. Zhai and L. Jiang, *Acc. Chem. Res.*, 2010, **43**, 368.
9 B. Deng, R. Cai, Y. Yu, H. Jiang, C. Wang, J. Li and L. Li, *Adv. Mater.*, 2010, **22**, 5473.
10 J. Wang, Y. Zheng, F. Q. Nie, J. Zhai and L. Jiang, *Langmuir*, 2009, **25**, 14129.
11 W. Choi, A. Tuteja, S. Chhatre and J. M. Mabry, *Adv. Mater.*, 2009, **21**, 2190.
12 M. J. Hancock, K. Sekeroglu and M. C. Demirel, *Adv. Funct. Mater.*, 2012, **22**, 2223.
13 X. F. Gao, X. Yan, X. Yao, L. Xu, K. Zhang and J. H. Zhang, *Adv. Mater.*, 2007, **19**, 2213.
14 Z. Zhang, T. Zhang, Y. W. Zhang, K. S. Kim and H. Gao, *Langmuir*, 2012, **28**, 2753.
15 M. Xiao, M. Cheng, Y. Zhang and F. Shi, *Small*, 2013, **9**, 2509.
16 Y. C. Jung and B. Bhushan, *J. Phys.: Condens. Matter*, 2010, **22**, 035104.
17 G. D. Bixler and B. Bhushan, *Nanoscale*, 2013, **5**, 7685.
18 A. Solga, Z. Cerman, B. F. Striffler, M. Spaeth and W. Barthlott, *Bioinspiration Biomimetics*, 2007, **2**, S126.
19 T. S. Wong, S. H. Kang, S. K. Y. Tang, E. J. Smythe and B. D. Hatton, *Nature*, 2011, **477**, 443.
20 X. Wang, X. Liu, F. Zhou and W. Liu, *Chem. Commun.*, 2011, **47**, 2324.
21 M. Kobayashi, *Comm. Nonlinear Sci. Numer. Simulat.*, 2010, **15**, 787.
22 D. L. Royer, P. Wilf, D. A. Janesko, E. A. Kowalski and D. L. Dilcher, *Am. J. Bot.*, 2005, **92**, 1141–1151.
23 H. F. Huang, Q. X. Chu and J. K. Xiao, *IEEE Trans. Electromagn. Compat.*, 2010, **52**, 759.
24 M. Coppens, *Ind. Eng. Chem. Res.*, 2005, **44**, 5011.
25 W. Liu and Y. Zhang, *Adv. Nat. Sci.*, 2010, **3**, 82.
26 R. F. Service, *Science*, 2011, **334**, 925.
27 C. A. Price, S. J. C. Knox and T. J. Brodribb, *PLoS One*, 2013, **8**, e85420.
28 K. A. McCulloh, J. S. Sperry and F. R. Adler, *Nature*, 2003, **421**, 939.
29 C. S. Effenhauser, G. Bruin, A. Paulus and M. Ehrat, *Anal. Chem.*, 1997, **69**, 3451.
30 W. Wu, J. Wu, J. H. Kima and N. Y. Lee, *Lab Chip*, 2015, **15**, 2819–2825.
31 W. Wu, K. T. Kang and N. Y. Lee, *Analyst*, 2011, **136**, 2287.
32 W. Wu, K. T. L. Trinh and N. Y. Lee, *Analyst*, 2012, **137**, 2069.
33 W. Wu, K. T. L. Trinh and N. Y. Lee, *Analyst*, 2012, **137**, 983.
34 W. Wu and A. Manz, *RSC Adv.*, 2015, **5**, 70737.
35 W. Wu and N. Y. Lee, *Anal. Bioanal. Chem.*, 2011, **400**, 2053.
36 W. Wu, C. J. Hansen, A. M. Aragón, P. H. Geubelle, S. R. White and A. Lewis, *Soft Mater.*, 2010, **6**, 739.
37 W. Wu and N. Y. Lee, *Sens. Actuators, B*, 2013, **181**, 756.
38 H. J. Koo and O. D. Velev, *Sci Rep.*, 2013, **3**, 2357.
39 X. Noblin, L. Mahadevan, I. A. Coomaraswamy and D. A. Weitz, *Proc. Natl. Acad. Sci. U. S. A.*, 2008, **105**, 9140.
40 J. He, M. Mao, Y. Liu, J. Shao, Z. Jin and D. Li, *Adv. Healthcare Mater.*, 2013, **2**, 1108.
41 I. Wagner, E. Materne, S. Brincker, U. Süßbier, C. Frädrich, M. Busek, F. Sonntag, D. A. Sakharov, E. V. Trushkin, A. G. Tonevitsky, R. Laustera and U. Marxa, *Lab Chip*, 2013, **13**, 4697.
42 I. Maschmeyer, A. K. Lorenz, K. Schimek, T. Hasenberg, A. P. Ramme, J. Hübner, M. Lindner, C. Drewell, S. Bauer, A. Thomas, N. Sambo, F. Sonntag, R. Lauster and U. Marx, *Lab Chip*, 2015, **15**, 2688.
43 K. Schimek, M. Busek, S. Brincker, B. Groth, S. Hoffmann, R. Lauster, G. Lindner, A. Lorenz, U. Menzel, F. Sonntag, H. Walles, U. Marxa and R. Horland, *Lab Chip*, 2013, **13**, 3588.
44 X. Liu, M. Mwangi, X. Li, M. O'Brien and G. Whitesides, *Lab Chip*, 2011, **11**, 2189.
45 K. A. Shaikh, K. Ryu, E. Goluch, J. Nam, J. Liu, C. Thaxton, T. N. Chiesl, A. E. Barron, Y. Lu, C. Mirkin and C. Liu, *Proc. Natl. Acad. Sci. U. S. A.*, 2005, **102**, 9745.
46 I. K. Dimov, L. Basabe-Desmonts, J. L. Garcia-Cordero, B. M. Ross, A. J. Ricco and L. P. Lee, *Lab Chip*, 2011, **11**, 845.
47 W. Wu, K. T. L. Trinh and N. Y. Lee, *RSC Adv.*, 2015, **5**, 12071.
48 W. Wu, K. T. L. Trinh and N. Y. Lee, *Analyst*, 2015, **140**, 1416.
49 C. Hall and W. D. Hoff, *Water Transport in Brick, Stone and Concrete*, CRC Press, 2012.
50 R. Siddique, *Construct. Build. Mater.*, 2013, **47**, 1444.
51 L. Hu, H. Zhou, H. Zhu, T. Fan and D. Zhang, *Soft Matter*, 2014, **10**, 8442.

Electronic Supplementary Material (ESI) for RSC Advances.

Plant leaves as templates for soft lithography

Electronic Supplementary Material

Wenming Wu[1,2], Rosanne M. Guijt[3], Yuliya E. Silina[4], Marcus Koch[4] and Andreas Manz[1,2]*

[1]Mechatronics department, University of Saarland, Germany
[2]KIST Europe GmbH, 66123, Saarbrücken, Germany
[3]University of Tasmania, Australia
[4]INM-Leibniz Institute for New Materials, Campus D2 2, Saarbrücken, Germany

Correspondence and requests for materials should be addressed to A.M. (manz@kist-europe.de)

1 Biodiversity

As shown in Fig. S1r ~ s, the large variety of natural microvascular networks can be transferred to PDMS microfluidic devices with high fidelity. As shown in Fig. S1r, hair like trichomes feature like holes in the PDMS replicas. Fig. S1s, shows the replication of wrinkles of 400 nm ~ 1.2 μm in width.

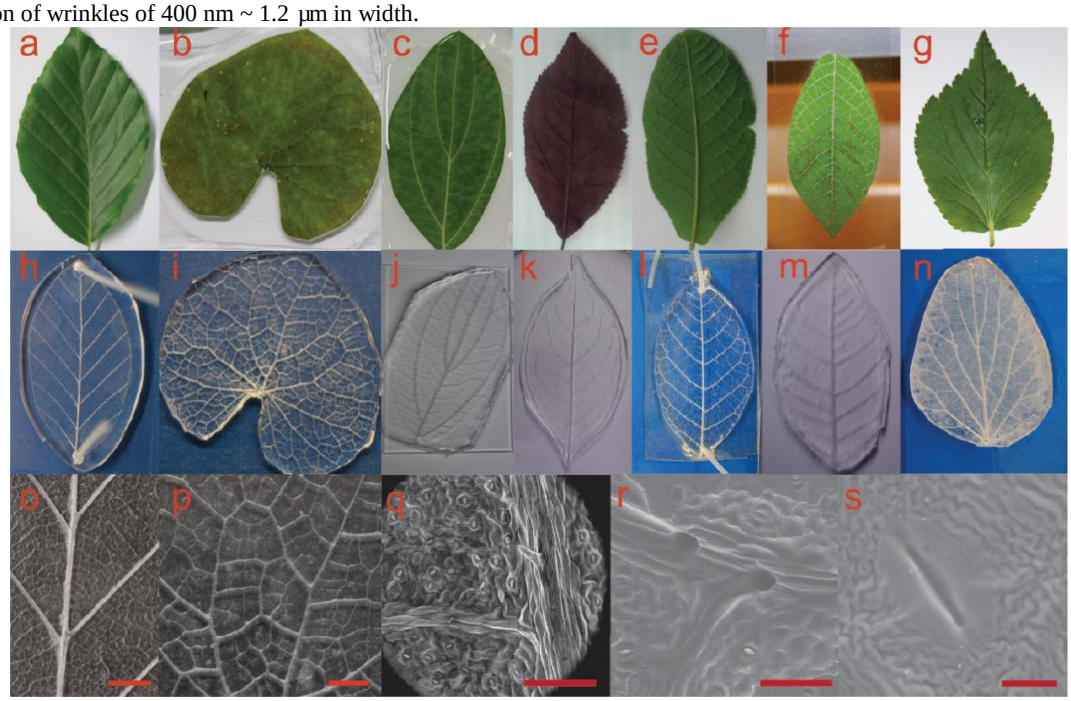

Fig. S1 Diverse biomimetic microchips directly fabricated from various natural leaves. Examples of leaves and their replicates. (a) Leaf of Carpinus betulus. (b) Leaf-template (Glechoma hederacea) immersed with PDMS inside Petridish. (c) Leaf-template (Viburnum davidii) immersed with PDMS inside Petridish. d) Leaf of Prunus cerasifera. (e) Leaf of Prunus avium. (f) Leaf-template (Prunus avium) attached to single-side tape. (g) Simple Leaf of Aegopodium podagraia. (h) ~ (m) Nature inspired microchips fabricated from Carpinus betulus, Glechoma hederacea, Viburnum davidii, Prunus cerasifera, Prunus avium and Fraxinus excelsior. (n) PDMS replica from Aegopodium podagraia leaf. (o) ~ (p) Enlarged microvascular image of biomimetic microchip replicated from Carpinus betulus and (Glechoma hederacea) leaf. (q) SEM image of Aegopodium podagraia leaf. (r) ~ (s) SEM images of biomimetic PDMS mould (prepared at 1:20) replicated from Aegopodium podagraia leaf. Scale bars in (o) ~ (s) are 0.25 cm, 0.25 cm, 200 μm, 100 μm and 10 μm, respectively.

2 Microchannel characterization

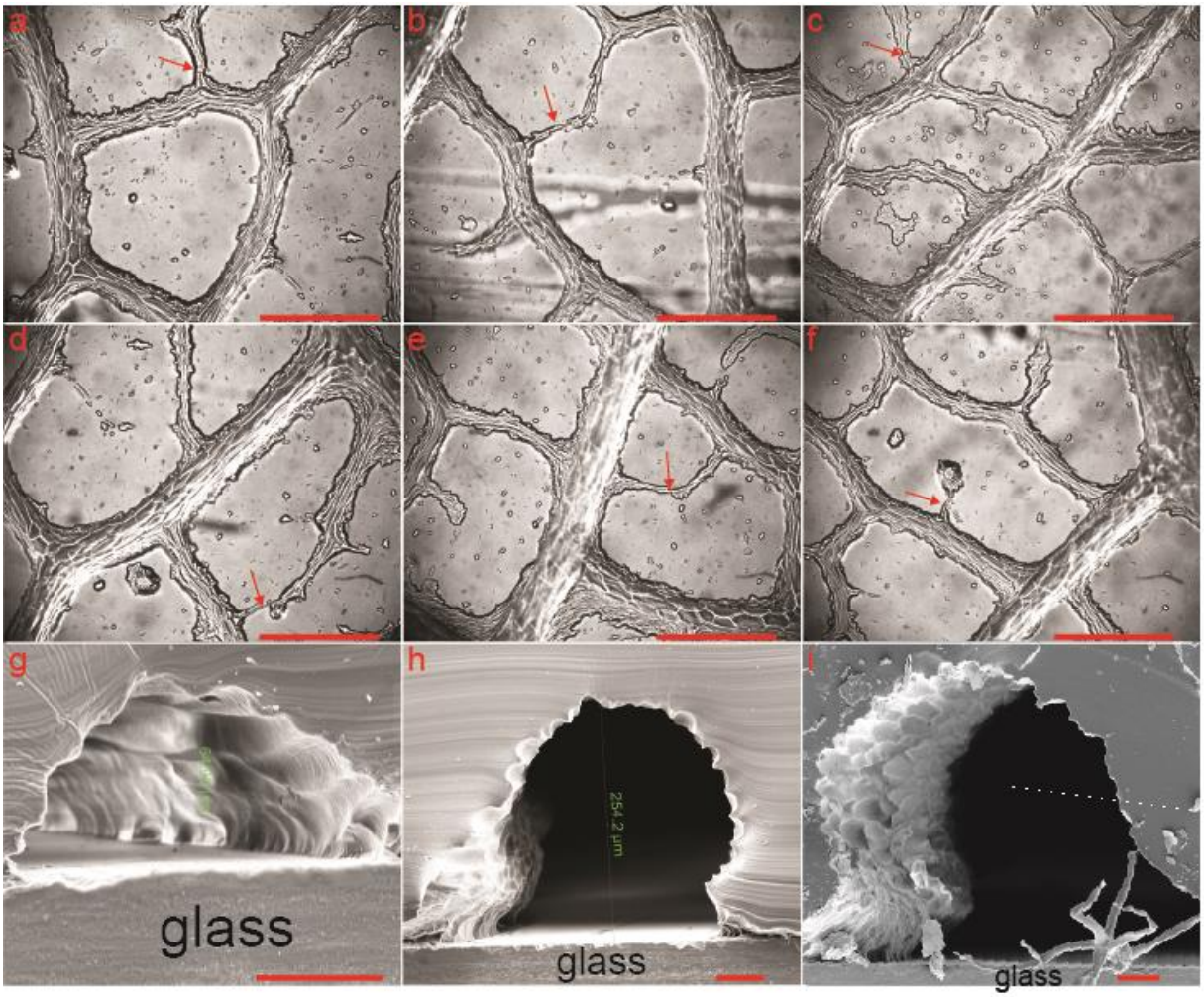

Fig. S2 Microvascular channel of PDMS leaf fabricated from Glechoma hederacea. Scale bars (a) - (f) 500 µm, (g) - (i) 50 µm.

As shown in Fig. S2, the smallest channel width from (a) ~ (f) was found to be 22.3 µm, 8.1 µm, 18.2 µm, 8 µm, 9.7 µm and 9.2 µm, respectively.

As shown in Fig. S2g-i, the biomimetic microvascular channel has varied widths and heights, with micro-scaled topography replicated from the leaves surface onto channel.

3 AFM characterization

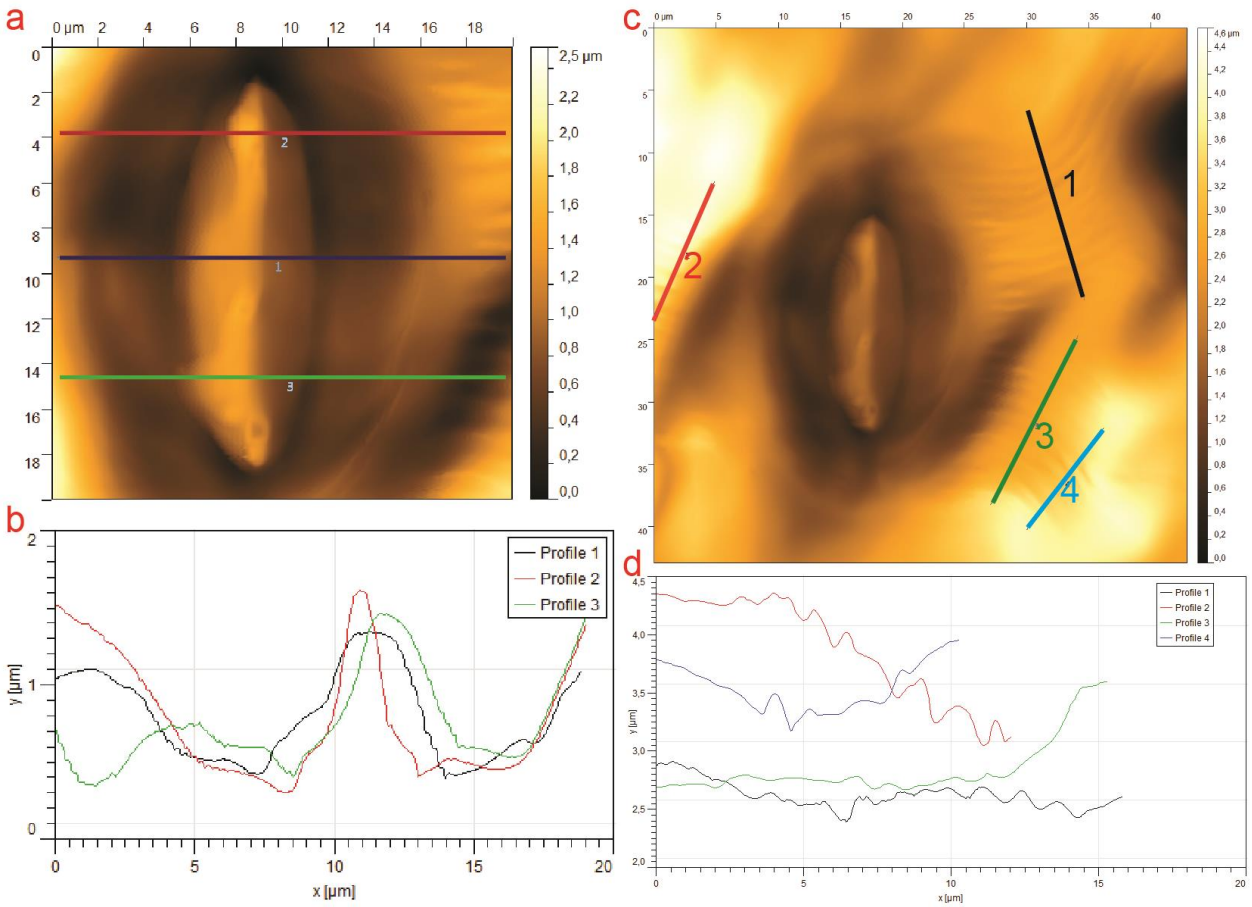

Fig. S3 AFM topography characterization of PDMS leaf. (a) 3D profile of the central part of one stoma on PDMS leaf replicated from Tilia platyphyllos, and corresponding line profiles of the stoma region (b). (c) 3D profile of the peripheral part of one stoma on PDMS leaf replicated from Tilia platyphyllos, and corresponding line profiles of the stoma region (d).

4 HS-GC-MS chromatograms

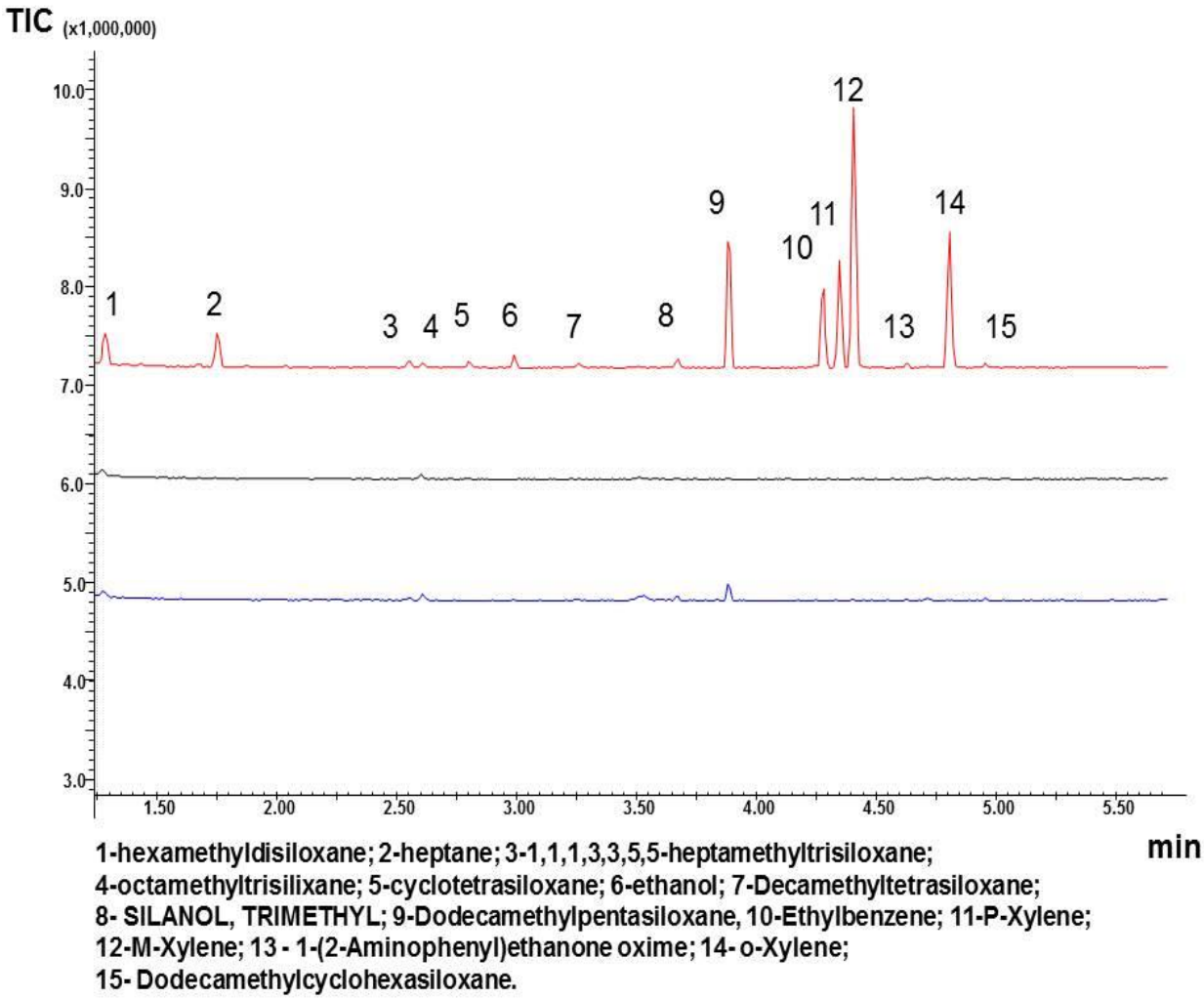

Fig. S4 HS-GC-MS chromatograms of the pure PDMS matrix (red); natural Tilia leaf (blue) after contact with PDMS; one-sided cut of PDMS matrix after contact with a natural Tilia leaf (black), obtained under 50 ℃

5 Longevity endurance of leaf template

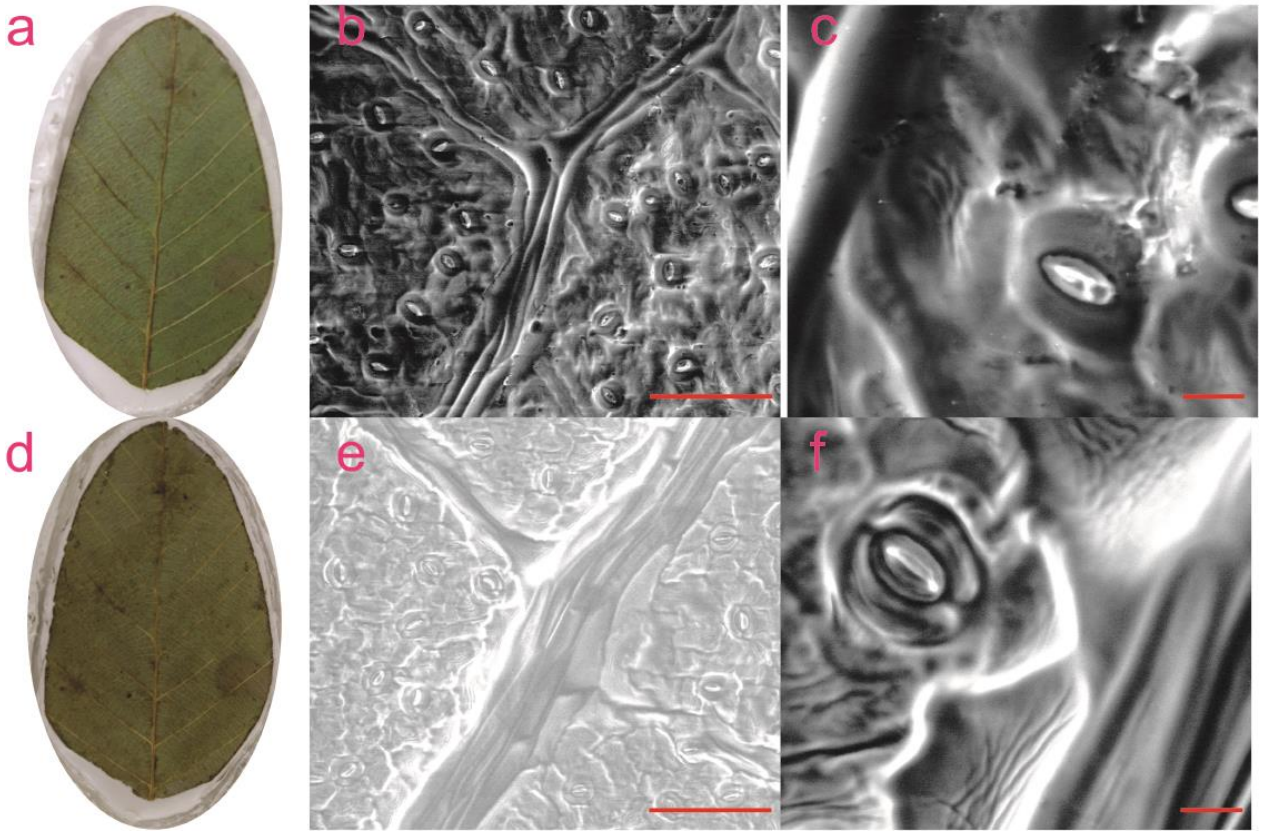

Fig. S5 Carpinus betulus leaf stored in PDMS for one year, utilized for microfabrication of over thirty times during this period. (a) Real image of Carpinus betulus leaf. (b) Microvascular channel in 1:20 PDMS replica from fresh Carpinus betulus leaf. (c) Enlarged image of stomata in 1:20 PDMS replica from fresh Carpinus betulus leaf. a) Real image of one year stored Carpinus betulus leaf. (b) Microvascular channel in 1:20 PDMS replica from one year stored Carpinus betulus leaf. (c) Enlarged image of stomata in 1:20 PDMS replica from one year stored Carpinus betulus leaf. Scale bars (b) and (e) 100 µm, (c) and (f) 10 µm.

6 Self-powered hydraulic flow through microvascular networks of PDMS leaves

We confirmed the pressure applied using the syringe indeed forced the air out of the channels to replace this volume with liquid by visualising the air as bubbles on the PDMS surface when the device was pressurised in a water bath.

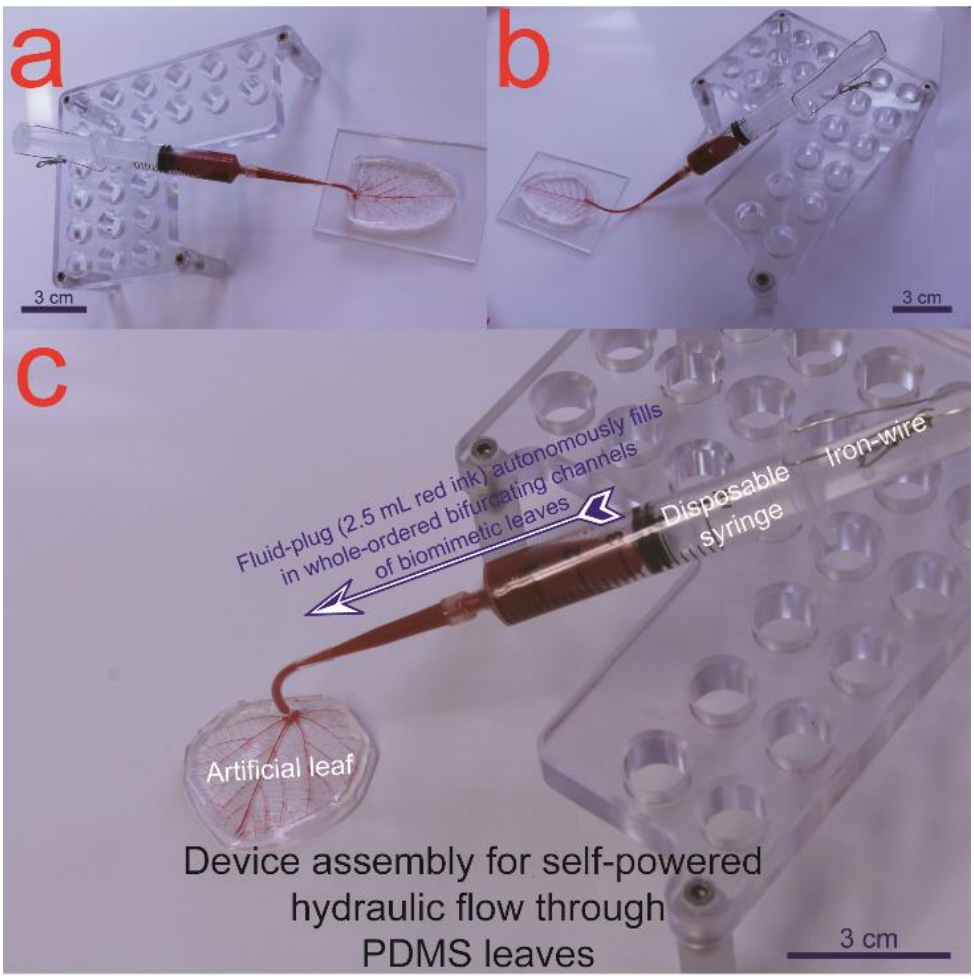

Fig. S6 The filling of the microvascular networks of PDMS replicates using only an inlet channel. (a) The artificial leaf with reticulate networks. (b) The artificial leaf with parallel networks. (c) The artificial leaf with intensive reticular characteristic networks. The scale bar in (a), (b) and (c) are 3 cm.

As shown in Fig. S7, through real-time monitoring of the hydraulic flow inside the microvascular networks, we could evaluate veinal dynamic conductance of biomimetic microvasculature in real time, covering all bifurcating channels ranging from highest order to lowest order. Electronic supplementary information (see ESI 2, ESI 3) is also provided to visually display self-powered flow inside biomimetic microvasculature with complex architectures.

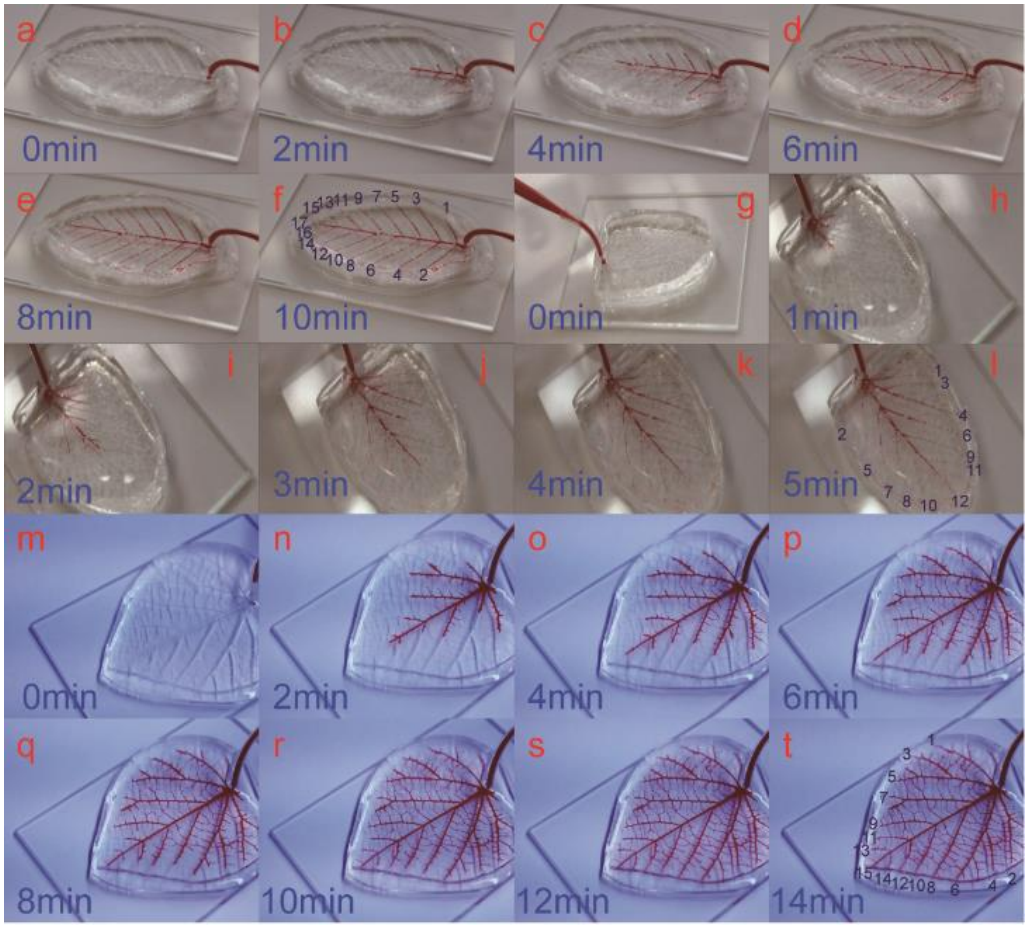

Fig. S7 Nature inspired biomimetic Microchips with whole ordered micronetwork replicated from Tilia platyphyllos, Aegopodium podagraia and Carpinus betulus, for self-powered flow analogy. (a) ~ (f) Self-powered flow analogy inside PDMS leaf containing parallel networks replicated from Carpinus betulus, with a time interval of 2 mins. (g) ~ (l) Self-powered flow analogy inside PDMS leaf replicated from Aegopodium podagraia, with a time interval of 1 min. (m) ~ (t) Self-powered flow analogy inside PDMS leaf replicated from Tilia platyphyllos, with a time interval of 2 mins.

The first PDMS leaf from Carpinus betulus (Fig. S7a~f) had 2-order microvascular bifurcating structures, with one 4.7 cm long first-ordered microchannel (No. 17 in Fig. S7f) in leaf's center and sixteen parallel second-ordered micochannels (No. 1 ~ 16 in Fig. S7f) extending from the central microchannel. As shown in Fig. S7f, the length of second ordered channel varied from 1.7 cm (No. 5, 6) to 0.3 cm (No. 15, 16), with average length of second-ordered microchannels of 1.2 cm. Based in real-time monitor of flow, we found the duration time in first-ordered microchannel was around 628 seconds, while the duration time in second-ordered microchannels gradually decreased from 470 seconds (No. 1, 2) to 110 seconds (No. 15, 16). Correspondingly, the average flowing rate in first-ordered microchannel and second-ordered microchannel were calculated to be 0.00357 cm/sec and 0.00745 cm/sec, respectively. So the flow rate of first-ordered microchannel was 2.08 times of the average rage in second-ordered microchannels.

The second PDMS leaf fabricated from Aegopodium podagraia (Fig. S7h~m) had 2-order microvascular bifurcating structures. But different from the first PDMS leaf, the second PDMS leaf had five first-ordered microchannels extending from the inlet (No. 1, 2, 4, 5, 12 in Fig. S7l) and various second-ordered microchannels (No. 3, 6 ~ 11 in Fig. S7l). Noticeably, the first-ordered microchannel in the center of PDMS leaf (No. 12) was 4.3 cm in length, much longer than another four first-ordered microchannels (No. 1, 2, 4, 5) with average length of 2.5 cm. The duration in first-ordered microchannels (No. 1, 2, 4, 5, 12) were 150 sec, 130 sec, 210 sec, 140 sec, and 275 sec, respectively, with corresponding flow rate calculated to be 0.0153 cm/sec, 0.0161 cm/sec, 0.0148 cm/sec, 0.0164 cm/sec and 0.0156 cm/sec, respectively. For the second-ordered microchannels, average flow rate were calculated to be 0.0109 cm/sec. So average flow rate in first-ordered microchannel is around 1.43 times of that in second ordered microchannels.

The third PDMS leaf fabricated from Tilia platyphyllos (Fig. S7m~t) had 3-order microvascular bifurcating structures. Herein we calculated the flowing performance in five first-ordered microchannels (No. 1, 2, 5, 6, 15 in Fig. S7t) and ten second-ordered

microchannels (No. 3~4, 7~14 in Fig. S7t). The first-ordered microchannel in the center of PDMS leaf (No. 15) was 4.2 cm in length, while other first-ordered microchannels (No. 1, 2, 5, 6) had average length of 2.55 cm. The average flow rate in all first-ordered microchannels (No. 1, 2, 5, 6, 15) were calculated to be 0.0447 cm/sec; and the average flow rate in second-ordered microchannels (No. 3~4, 7~14 in Fig. S7t) were calculated to be 0.0222 cm/sec. So average flow rate in first-ordered microchannels was 2.17 times of second ordered microchannels.

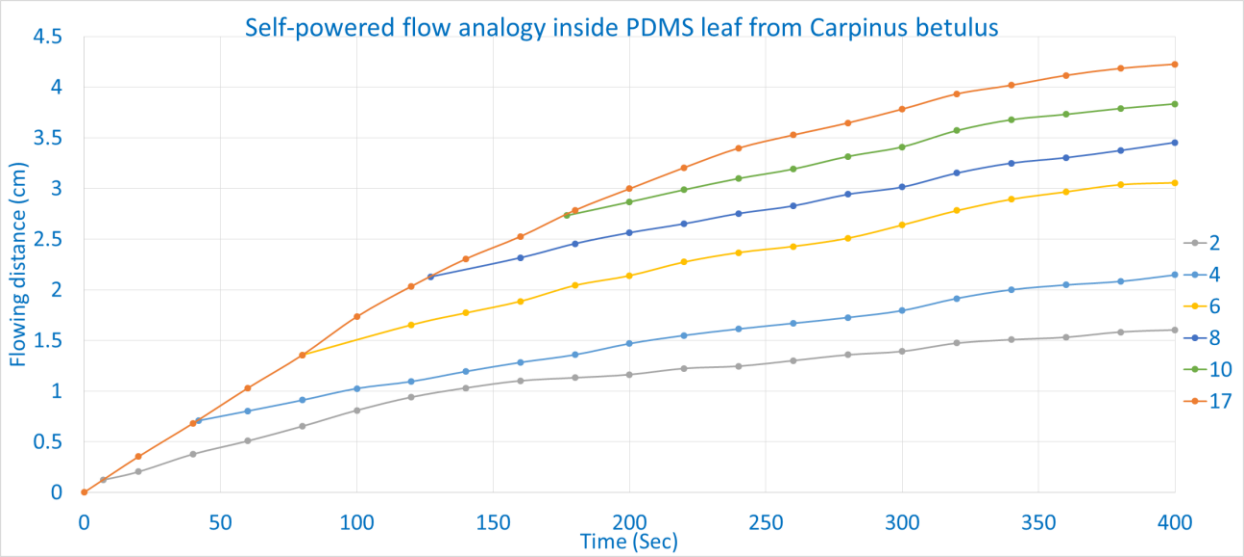

Fig. S8 Quantitative self-powered flow analogy inside PDMS leaf containing parallel networks replicated from Carpinus betulus. The flowing distance is plotted versus time, with a time interval of 20 secs.

3.4 Wu *et al.* (2015)

Wenming Wu, Kieu The Loan Trinh, Yu Zhang and Nae Yoon Lee, "Portable plastic syringe as a self-actuated pump for long-distance uniform delivery of liquid inside a microchannel and its application for flow-through polymerase chain reaction on chip", RSC Adv., 2015, 5, 12071-12077. (SCI indexed, IF = 3.840) **(First author)**

This cooperated project is done with Prof. Nae Yoon Lee of Gachon University in Korea, and Prof. Manz provides sincere encourage and supports for such international cooperative project.

Authorship Contributions

Wenming Wu: participate in research design, contribute to principle, perform data analysis, and write the manuscript

Kieu The Loan Trinh: participate in research design, conduct experiments, perform data analysis, and modify the manuscript

Yu Zhang: modify the manuscript

Nae Yoon Lee: participate in research design, evaluate the result, and modify the manuscript

This work affirms diffusion pump as an efficient approach in uniform liquid delivery for long-distance PMMA microchannel.

A self-activated micropump, which can stably transport a limited amount of sample plug over long distance, has become the aim of researchers during last several decades. Nevertheless, various challenges are presented in realizing this aim. Here, I introduce a self-activated micropump, which for the first time, can homogeneously transport fluidic over long distance without consuming any power. When traditional micropumps are utilized for microfluidic transportation under high temperature, e.g., 95°C which is close to the boiling point of water, large

amounts of vapor bubbles may form inside the microdevice and thus impend the flow stability. In contrast, this micropump can efficiently suppress vapor bubbles even if under such high temperature condition. Laborious fabrication steps or complicated integrated components are inevitably associated with most previous developed micropumps. Herein, without any fabrications steps or complicated integrated components, only one small piece of silicone tube is required to functionalize such self-activated micropump. The reliability of this self-activated micropump was confirmed by its efficient performance in handling flow-through polymerase chain reaction (PCR) for both a 230-bp plasmid vector obtained from E. coli and a D1S80 locus obtained from a human genomic, requiring homogeneous flow to ensure the DNA amplification result.

Since the actuation mechanism of this stable and self-activated micropump is virtually based in air penetration from inside the pressurized fluidic conduit (the outlet tube) to outside atmospheric environment, how the length of the outlet tube determine the flow rate should be analysed. Besides, the quantitative relationship between other parameters (e.g., the height, the width and the length of the micro channel) and the flow rate also requires to be clarified.

To optimize the control parameters of this new self-activated micropump, a series of experiments are performed to ascertain the specialized flow rate under above parameters (Fig.4, article 4). A 25 mL disposable syringe is used for all flowing experiments, and each experiment was performed in triplicate and averaged. All flowing experiments are done at an initial internal of 2 atm. Initial internal pressure was adjusted to this pressure by pushing the piston from 25 to 12.5 mL of the syringe graduation. In this way, the air captured inside the fluidic conduit was compressed to maintain the specific internal pressure, which is about double atmospheric pressure.

RSC Advances

PAPER

Cite this: *RSC Adv.*, 2015, **5**, 12071

Portable plastic syringe as a self-actuated pump for long-distance uniform delivery of liquid inside a microchannel and its application for flow-through polymerase chain reaction on chip†

Wenming Wu,‡§[a] Kieu The Loan Trinh,§[a] Yu Zhang[a] and Nae Yoon Lee*[ab]

Received 29th November 2014
Accepted 12th January 2015

DOI: 10.1039/c4ra15473h

www.rsc.org/advances

A portable plastic syringe was used as a self-actuated pump for uniform delivery of liquid inside a microchannel over a distance of more than 2 meters at a controllable flow rate and without utilizing external electrical power and bulky pumping apparatus. The reliability of the plastic syringe as a potential self-actuator was investigated by performing a flow-through polymerase chain reaction (PCR) on a microdevice fabricated using poly(methylmethacrylate) (PMMA). Liquid flowed at a uniform rate inside the PMMA microchannel in a highly controllable manner even under high-temperature conditions and without the generation of bubbles, and the flow rate was readily adjusted as necessary by varying the operation parameters such as the length of the outlet silicone tube, channel dimension, and initial syringe pressure. A 230 bp plasmid vector obtained from *E. coli* and a D1S80 locus obtained from a human genomic DNA were successfully amplified on a PMMA microdevice equipped with the disposable plastic syringe as a self-actuated micropump.

Introduction

Due to its crucial role in transporting liquid, the micropump has been recognized as one of the most important ingredients of micro Total Analysis Systems (μTAS), and thus, has been the hot issue of wide research interests. In the 1980s, Lintel *et al.*[1] and Smits[2] developed the first genuine MEMS micropumps actuating fluid on the microscale utilizing piezoelectrics. During the last 20 years, over ten mechanisms have been introduced to structure diverse pumping systems appropriate for μTAS, such as the peristaltic micropump,[3] thermo-pneumatic micropump,[4] magnetic micropump,[5] and electro-hydrodynamic micropump.[6] Despite numerous achievements in the development of micropumps,[7] the majority of such devices that have been developed so far require external power for operation.[3–12] Besides, complex fabrication steps or operation processes are always inevitable when using such aforementioned pumps. These disadvantages hinder miniaturization, which is one of the key issues in μTAS.

In order to circumvent above problems, some self-actuated micropumps have been developed, dispensing with any external power. Among these self-actuated micropumps, capillary micropump is one typical representative and simplest format, utilizing capillary force to spontaneously transport small amount of liquid.[13,14] The surface tension resulting from solid–liquid, liquid–gas, and solid–gas interactions, produces an equilibrium contact angle in the anterior and posterior ends of liquid plug inside a microchannel, and governs the self-actuation of sample liquid inside the microchannel. Flow velocity of capillary micropump is reduced non-linearly, as the strength of capillary forces per sample volume decreases dramatically, as more and more sample flows into the microchannel. Also, the inner surface of the microchannel should be hydrophilic. Besides the capillary micropump, vacuum pump was also introduced by Dimov *et al.* to realize a self-powered integrated device for blood assay, where a high air permeability of the microdevice was the critical element.[15] After placing poly(dimethylsiloxane) (PDMS) chip into a vacuum chamber, the air molecules inside the chip permeated through porous PDMS, which resulted in relatively lower pressure at the anterior end of the sample, forming an actuation force toward the outlet. A vacuum chamber and a permeable microdevice are the two preconditions in realizing such pump.

Recently, a wicking flow has also become a hot issue due to its dramatic property in spontaneous transportation of liquid through a microchannel.[16–18] The mechanism of wicking micropump virtually relies on capillary flow, but the platforms

[a]*Department of BioNano Technology, Gachon University, 1342 Seongnam-daero, Sujeong-gu, Seongnam-si, Gyeonggi-do 461-701, Republic of Korea*

[b]*Gil Medical Center, Gachon Medical Research Institute, Inchon 405-760, Republic of Korea. E-mail: nylee@gachon.ac.kr; Fax: +82-31-750-8774; Tel: +82-31-750-8556*

† Electronic supplementary information (ESI) available. See DOI: 10.1039/c4ra15473h

‡ Current address: Mechatronics Department, University of Saarland, Saarbrücken, Germany. KIST Europe GmbH, Saarbrücken, Germany.

§ Both these authors contributed equally to this work.

utilized here are mainly paper or textiles, instead of silicon or glass as in capillary micropumps. In addition to aforementioned self-actuated micropumps, Qin *et al.* also introduced a hydrolytic-powered pump, which can catalytically decompose H_2O_2 into oxygen for creating a pressure gradient which induces sample injection.[19] Even if self-actuated micropumps obtain more noticeable advantages than those which utilize external power, all of these encounter the bottleneck in providing homogeneous flow over a long distance such as several meters.[13–19] Besides, it is also difficult for previously developed self-actuated micropumps to stably transport liquid under harsh microenvironment[13–19] such as high temperature condition. These defects restricted the application of self-actuated micropumps in many areas, *i.e.*, continuous-flow PCR, which always requires a microchannel as long as several meters[20–25] and a temperature as high as 95 °C.

To solve the above-mentioned problems, here a new self-actuated micropump is introduced, which can maintain homogeneous liquid flow over a long distance. The introduced self-actuated micropump not only can stably work at room temperature, but is also reliable under high temperature. Furthermore, not many fabrication steps are involved here. By connecting one small piece of silicone tube to the outlet of a gas-impermeable poly(methylmethacrylate) (PMMA) microdevice and clamping it to realize a blunted end, homogeneous transportation of fluid can be realized using a disposable syringe, connected to the inlet *via* another short segment of a silicone tube with negligible gas permeability. Using the microdevice, a pGEM-3Zf(+) plasmid vector obtained from DH5-α *E. coli* and D1S80 locus obtained from a human genomic DNA, were successfully amplified inside a PMMA microdevice.

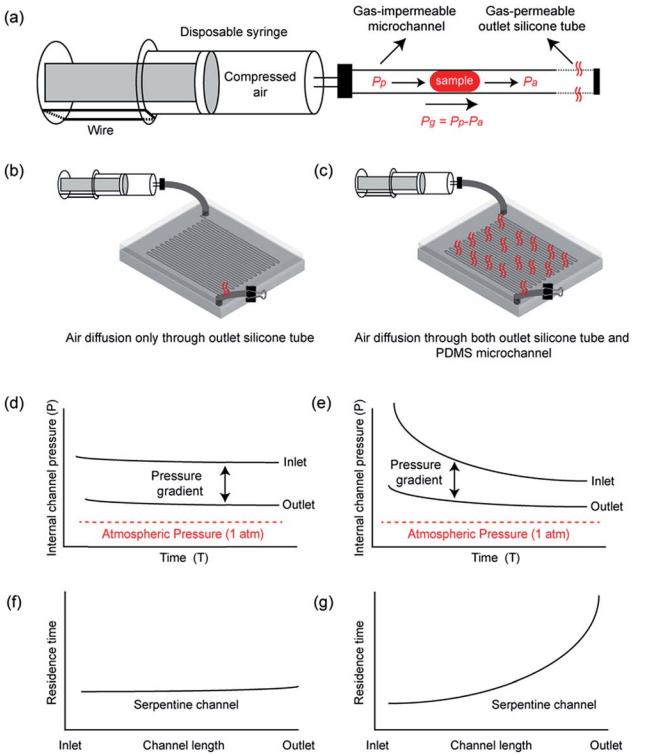

Fig. 1 (a and b) Schematic illustrations demonstrating a new concept for self-actuated pump realizing homogeneous sample flow inside a PMMA microchannel, and comparison with (c) previous study. (d) A schematic graph demonstrating a constant pressure gradient formed by the pressure difference in the inlet and the outlet of the fluidic conduit in this study. (e) A schematic graph demonstrating a gradual reduction in the pressure gradient formed by the pressure difference in the inlet and outlet of the fluidic conduit in our previous study. (f and g) Schematic graphs comparing the sample residence time inside serpentine microchannels in (f) this study and (g) previous study.

Principle

Fig. 1 shows a schematic illustration revealing the actuation mechanism of two different self-actuated micropumps. Both of the mechanisms were based on air permeability from the fluidic conduit to the atmosphere. In our previous studies,[21,22] we have introduced a concept for a self-actuated micropump for delivering sample plug inside a microchannel. However, flow velocity gradually decreased with time. In contrast, the self-actuated micropump introduced here can deliver sample plug with homogenous flow velocity inside a very long microchannel reaching over 2 meters. For actuation, a disposable syringe is connected to the inlet of a gas-impermeable PMMA microchannel. Besides, a permeable silicone tube is connected to the outlet of the fluidic conduit and blunt-ended by using a commercial clamp. As shown in Fig. 1a, P_p and P_a represent the air pressures in the posterior and anterior ends of the sample plug, respectively, while P_g represents the pressure gradient imposed on the sample plug which can be expressed as the following equation.

$$P_g = P_p - P_a$$

Since the pressure of the compressed air captured inside the closed fluidic conduit is higher than the atmospheric pressure, air molecules tend to diffuse from inside the microchannel to the atmosphere. The inlet tube, the PMMA microdevice, and the disposable syringe used here, can all be considered as gas-impermeable, as compared to outlet silicone tube, which is gas-permeable. For this reason, the gas permeability in the posterior end of the sample can be considered negligible, and the air molecules can be rendered to diffuse from the fluidic conduit to the atmosphere only through the outlet silicone tube.

The ideal gas law represented as follows, can be used to calculate the relationship among the pressure (P), the volume (V), and the number of moles of the air molecules (n), where T is the Kelvin temperature and R is the gas constant.

$$PV = nRT$$

Before the sample plug is introduced into the microdevice, air pressure throughout the entire fluidic conduit is the same, represented by $P_p = P_a$. After the sample plug is introduced from the inlet tube by disposable syringe, the sample plug separates the fluidic conduit into two parts, that is, the gas-permeable part at the anterior end and the gas-impermeable part at the

posterior end of the sample plug, resulting in varying gas permeability at both ends of the sample plug. The gas diffusion in the anterior end of sample causes a pressure drop in P_a. Since there is negligible gas diffusion in the posterior end of the sample, P_p can be considered constant. As a result, a homogeneous pressure gradient (P_g) is imposed on the sample plug, and this propels the sample toward the outlet with identical flow velocity (Fig. 1b, d and f), whereas in our previous studies,[21,22] air diffusion occurred all throughout the entire fluidic conduit (Fig. 1c, e and g).

If the inner and outer radii of the outlet silicone tube are r_i and r_o, respectively, the following equation can be derived,

$$G_a = \frac{DA_{av}}{Z}(C_{Aia} - C_{Ao})$$

where G_a is diffusion flux, D is effective diffusion coefficient, C_{Aia} is the concentration of the inner air molecules at the anterior end of the sample plug, C_{Ao} is the concentration of air molecules in the outside atmosphere, Z is the diffusion length, and A_{av} is the average diffusion area. The average diffusion area, A_{av}, can be calculated by the following equation, where L is the total length of the outlet silicone tube.

$$A_{av} = \frac{2\pi L(r_o - r_i)}{\ln \frac{r_o}{r_i}}$$

The diffusion length, Z, can be calculated by the following equation.

$$Z = r_o - r_i$$

So the relationship between the diffusion rate of the air molecules, G_a, and the parameters of outlet tube can be expressed as follows,

$$G_a = \frac{2\pi LD}{\ln \frac{r_o}{r_i}}(C_{Aia} - C_{Ao})$$

which can be converted to the following pressure-based equation.

$$G_a = \frac{2\pi LD}{RT \ln \frac{r_o}{r_i}}(P_a - P_{atm})$$

From the above equations, we can estimate that the diffusion flux increases as the length or inner diameter of the outlet silicone tube increases. Also, as the inner pressure at the anterior end of sample plug increases, the diffusion flux also increases accordingly.

The self-actuation mechanism introduced in this study is totally different from our previous studies.[21,22] In our previous works, the air molecules freely diffused from both at the anterior and posterior ends of the sample plug. As the sample plug progresses forward inside the microchannel, the diffusion area at the posterior end tends to increase. Meanwhile, the diffusion area at the anterior end tends to decrease. As a result, the pressure gradient imposed on the sample plug caused by the non-homogeneous diffusion between the anterior and posterior ends of the sample plug tends to decrease, resulting in a gradual decrease in the overall sample flow. In contrast, since air diffuses only through the outlet silicone tube while the areas of gas diffusion at the anterior and posterior ends of the sample plug – A_{av} and 0 – are kept constant, the introduced self-actuation mechanism can maintain homogeneous liquid flow. In other words, the air diffusion in the outlet silicone tube is the only driving force for sample movement. In addition, impermeability of air at the posterior end of the sample plug and its extremely large volume kept inside the syringe makes the pressure at the posterior end nearly constant, not much decreased as compared to the initial pressure of the compressed air inside the syringe, throughout the sample transport toward the outlet.

In our previous work,[20] we have proven that the velocity of sample plug flowing through the microchannel with rectangular cross-section, is proportional to the pressure gradient (P_g) imposed on the sample plug. But in the new concept of self-actuation, since P_p is constant, the flow velocity is only determined by P_a. For a simpler model of the new self-actuation mechanism, the following equation can be derived,

$$Q_a = G_a = \frac{2\pi LD}{RT \ln \frac{r_o}{r_i}}(P_a - P_{atm}) = \vartheta H_c W_c$$

where Q_a is a fluidic flux, ϑ is the velocity of sample liquid, H_c is the height of the microchannel, and W_c is the width of the microchannel. Based on the above derived equation, we can predict that the flow velocity increases as the permeability (D), length (L), and inner diameter (r_i) of the outlet silicone tube as well as the inner pressure of the microchannel increases. Besides, if the outer diameter (r_o) of the outlet silicone tube or the width (W_c) and height (H_c) of the microchannel increases, the flow rate will decrease, since the flow rate is inversely proportional to the channel height and width under the same fluidic flux. Simply changing the length of the microchannel does not pose any significant effects on the flow rate since no parameter exist representing the length of the microchannel in the above equation. To summarize, considering that a gradual reduction in the pressure gradient was caused by the air diffusion both through the anterior and posterior ends of the sample plug in different ratio, this issue is resolved and homogeneous liquid flow was maintained simply by allowing air diffusion only through the outlet silicone tube, in this study.

Methods

Fabrication of microdevice

Fig. 2 shows the overall schematic for microdevice fabrication. A serpentine microchannel 200 μm wide and 50 μm deep was fabricated on one PMMA substrate (40 × 40 × 2 mm) using a computer numerical control (CNC) milling machine (Fig. 2a and b). After the inlet and outlet ports were punctured on another flat PMMA substrate using a drilling machine, the two

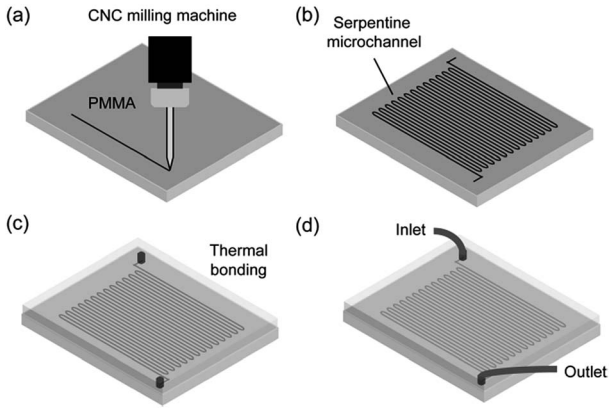

Fig. 2 (a) Fabrication of a serpentine microchannel on PMMA using a CNC milling machine. (b) Serpentine microchannel engraved on one PMMA substrate. (c) Punching inlet and outlet ports on a flat PMMA substrate, followed by thermal bonding. (d) Insertion of silicone tubes into the inlet and outlet ports.

PMMA substrates were thermally bonded at approximately 105 °C (Fig. 2c).[25] Finally, thick-walled silicone tube (i.d. 0.2 mm, o.d. 2 mm) was inserted into the inlet port and thin-walled silicone tube (i.d. 1 mm, o.d. 2 mm) was inserted into the outlet port, and then were glued using PDMS prepolymer (Fig. 2d). By this means, a PMMA microdevice with serpentine channels equivalent to 25 thermal cycles was fabricated. The total length of the microchannel was 1.25 m, which corresponded to approximately 5 cm per cycle.

Procedures for self-actuated liquid flow

Fig. 3 illustrates the procedures for preparing an air-filled syringe and connecting it to the PMMA microdevice for self-actuation of ink solution. First, a red ink, which was used in place of a sample liquid, was sucked into the disposable syringe. As shown in the inset in Fig. 3a, the ink was initially confined at the corner of the syringe. The viscosity of red ink solution at 25 °C is 9.89×10^{-4} Pa s, which was relatively close to that of the water at 25 °C (8.9×10^{-4} Pa s).[26] Prior to connecting syringe to the microdevice, the outlet silicone tube was clamped by a clip (Fig. 3a). Second, the syringe piston was pulled up to a certain graduation and then connected to the inlet silicone tube (Fig. 3b). In this stage, the ink is still confined at the corner of the syringe as shown in the inset in Fig. 3b. Third, the piston was pushed down to a certain graduation to compress the air inside the syringe, and then tied (Fig. 3c). In this stage, the ink is still confined at the corner of the syringe as shown in the inset in Fig. 3c. Now, the ink is deliberately moved to the tip of the syringe and entered into the fluidic conduit, physically segregating the two ends. Because only the silicone tube inserted into the outlet port was gas-permeable (plastic syringe, PMMA microdevice, and thick-walled silicone tube were considered gas-impermeable), air molecules diffused to the atmosphere exclusively through the outlet silicone tube, resulting in the propulsion of the sample toward the outlet of the microchannel. Fig. 3d shows a spontaneous ink flow inside the microchannel actuated by the syringe filled with large volume of compressed air.

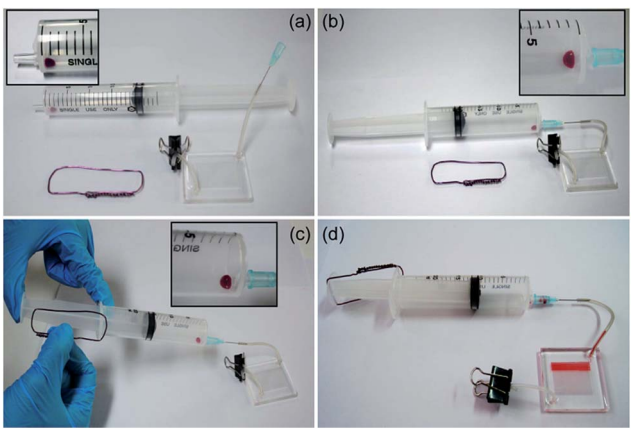

Fig. 3 Procedures demonstrating self-actuated sample injection. (a) The red ink was sucked into the bottom corner of the syringe and the outlet silicone tube was made air-tight. (b) The syringe was connected to the inlet silicone tube. (c) The air inside the syringe was compressed. (d) The ink flow through the PMMA microchannel was actuated by large volume of compressed air in the syringe.

Evaluation of self-actuated liquid flow

A 20 mL syringe was used in evaluating a series of flows, and each experiment was performed three times for reproducibility. All the flow tests were conducted using an initial internal pressure of approximately 2 atm. This was achieved by pushing the piston from the initial graduation of 20 to 10. First, the flow phenomenon was analyzed by varying the length of the outlet silicone tube. The graph in Fig. 4a shows the time-dependent flow rate changes when the length of the outlet silicone tube was varied. As shown in Fig. 4a, the flow rate increased with increasing length of the outlet silicone tube, resulting in shorter residence time for each cycle, and *vice versa*. For example, when the lengths of the outlet silicone tubes were 3, 2, and 1 cm, the total running times were 21, 31, and 50 min, respectively, which corresponded to an average residence times of approximately 49, 72, and 119 s per cycle, respectively. The use of longer outlet silicone tube resulted in faster ink flow inside the PMMA microchannel due to faster air diffusion through the gas-permeable silicone tube in the outlet. From these results, we could conclude that the flow rate of sample could be controlled by adjusting the length of the outlet silicone tube.

Second, the flow phenomenon was analyzed by varying the depth of the PMMA microchannel. The graph in Fig. 4b shows the time-dependent flow rate changes when the depths of the microchannel were varied at 20, 50, and 100 μm, respectively. The width of the microchannel and the length of the outlet silicone tube were fixed at 200 μm and 3 cm, respectively. As shown in Fig. 4b, the flow rate increased with reducing depth of the PMMA microchannel, resulting in a shorter residence time for each cycle, and *vice versa*. For example, when the depths of the microchannels were 20, 50, and 100 μm, the total running times were 12, 21, and 27 min, respectively, resulting in average

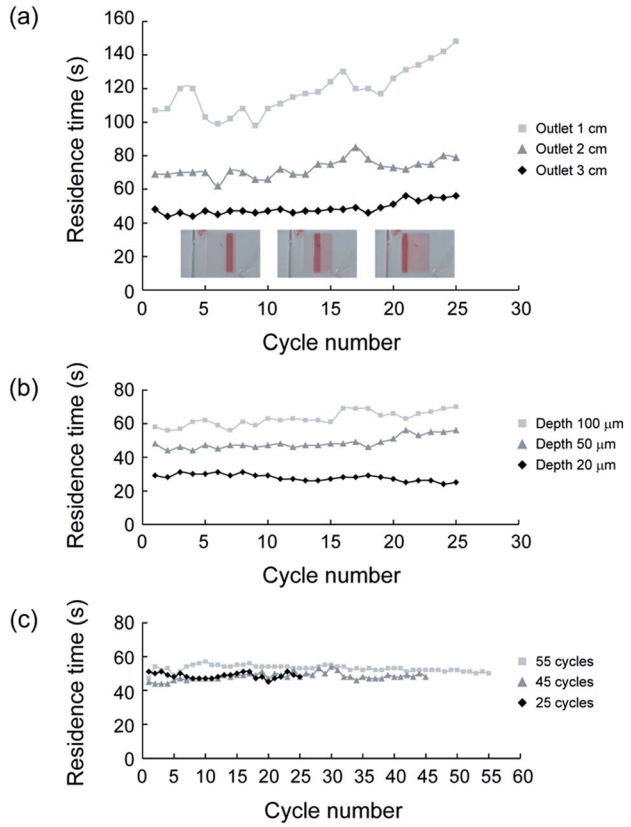

Fig. 4 Effects of (a) length of the outlet silicone tube, (b) depth of the PMMA microchannel, and (c) total length of the PMMA microchannel (cycle number) on the speed and uniformity of the sample flow. Photos in (a) show relative positions of ink plug inside the serpentine microchannel at certain cycle numbers when the length of the outlet silicone tube was 3 cm.

residence times of 28, 49, and 63 s, respectively. This was because, if the flow rates were identical for all three channels, the flow flux would be proportional to the channel depth, and the pressure gradient would be lower for a deeper channel, and *vice versa*. For this reason, the flow rate decreased with increasing channel depth, resulting in a longer residence time for each successive thermal cycle.

Third, the flow phenomenon was analyzed by varying the total length of the microchannel; that is, by varying the number of the serpentines, which is equivalent to the number of the thermal cycles. The width and depth of the microchannel were 200 and 80 μm, respectively, and the length of the outlet silicone tube was fixed at 3 cm. For total channel lengths of 1.25 m (25 cycles), 2.25 m (45 cycles), and 2.75 m (55 cycles), the total running times were 21, 37, and 49 min, respectively. However, the corresponding average residence times were approximately 49, 48, and 53 s, respectively. That is, the average residence times were almost identical regardless of the total length of the microchannel or the cycle number. This is probably because the PMMA microchannel itself is not gas-permeable, and the speed which determines the flow of the ink is the pressure gradient formed by the pressure difference in the anterior and the posterior ends of the ink, which in this case, was identical regardless of the total length of the microchannel. This was also the case with Fig. 4b, in that although different channel volume due to different channel depth resulted in different speed in the flow, the flow was seemingly uniform with slight fluctuations throughout the entire flow regardless of the depth of the microchannel.

Based on these results, we could rationally conclude that, among the three investigated parameters, the length of the outlet silicone tube was the most critical factor that affected the uniformity of liquid flow, presumably because of the gas permeability of the outlet silicone tube, which is the main cause for pressure gradient formation. These results match well with the hypothesis raised in the "Principle" section. Once a desired flow rate is established by finding the optimum length of the outlet silicone tube, the speed of the flow could further be fine-tuned by varying the depth of the microchannel. The number of the serpentines did not seem to affect the speed of flow significantly, which is very desirable because the required cycle number is likely to change depending on the size of the target to be amplified, and therefore, this factor can be neglected when finding the optimum flow rate. To summarize, the use of gas-permeable silicone tube in the outlet port triggered the flow of the liquid by forming pressure gradient between the anterior and posterior ends of the liquid plug, while the low permeability of PMMA microchannel aided in the maintenance of uniform flow rate over a long distance. A 32-fold fast-mode movie clip demonstrating almost constant ink flow inside a serpentine PMMA microchannel is presented as Movie S1 in the ESI.†

Polymerase chain reaction on a microdevice

Based on the above flow analyses, we performed a flow-through PCR using a PMMA microdevice. The PMMA microdevice was connected to a portable syringe and then placed on two heat

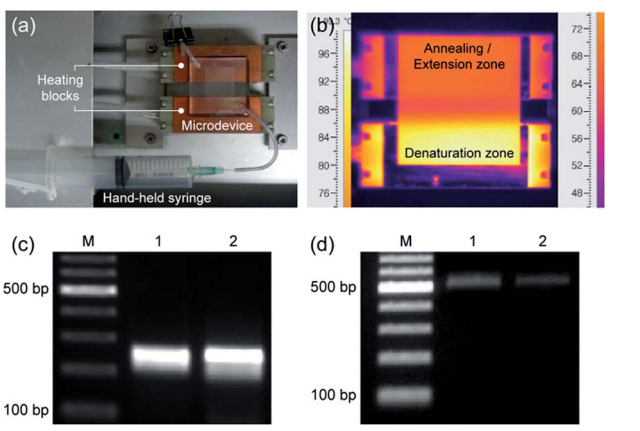

Fig. 5 (a) Experimental setup for performing the flow-through PCR on a PMMA microdevice equipped with a portable syringe. (b) Temperature measurement. (c) Amplification of the 230 bp gene fragment obtained from the pGEM-3Zf(+) plasmid vector. (d) Amplification of the D1S80 locus (369–801 bp) obtained from human genomic DNA. For both gel images, lanes 1 and 2 are results obtained using thermal cycler and PMMA microdevice, respectively. Lane M is a 100 bp DNA size marker.

blocks (Fig. 5a). The surface temperature of the PMMA substrate was measured using an infrared (IR) camera (FLIR Thermovision A320) (Fig. 5b). *E. coli* containing the pGEM-3Zf(+) plasmid vector, and a human genomic DNA (Roche) were used as the DNA templates for performing a two-temperature PCR.[27] The denaturation temperature was adjusted to 95 ± 0.5 °C, and the annealing/extension temperatures were adjusted to 68 ± 0.2 °C for the pGEM-3Zf(+) plasmid vector and 63 ± 0.1 °C for the human genomic DNA. The primer sequences for amplifying a 230 bp gene fragment of the pGEM-3Zf(+) plasmid vector were 5′-CCG GCG AAC GTG GCG AGA AAG GAA GGG AAG AAA GC-3′ (forward) and 5′-TCG CCT TGC AGC ACA TCC CCC TTT CGC CAG C-3′ (reverse). The primer sequences for amplifying the D1S80 locus[28–30] in human genomic DNA were 5′-GAA ACT GGC CTC CAA ACA CTG CCC GCC G-3′ (forward) and 5′-GTC TTG TTG GAG ATG CAC GTG CCC CTT GC-3′ (reverse).

The PCR reagent contained a 5 × green-colored buffer, 0.2 mM dNTPs mixture, 1 mg mL^{-1} BSA, 1 μM forward and reverse primers, and 0.075 U μL^{-1} *Taq* polymerase. The commercially available human genomic DNA (200 ng μL^{-1}) was diluted to achieve a concentration of 5 ng μL^{-1} in the PCR reagent, and the cultured *E. coli* solution was directly used to amplify the target gene (~230 bp) in the pGEM-3Zf(+) plasmid vector. Briefly, 0.5 μL of the *E. coli* culture solution was centrifuged at 14 000 rpm for 10 min and the supernatant was discarded. The precipitate was then resuspended in 0.5 μL of distilled water. In Fig. 5c and d, the results of DNA amplification performed using the PMMA microdevice actuated by a portable syringe were compared with those obtained using a thermal cycler. In both cases, 25 cycles were used for the amplification, and the total running times were less than 30 min when using the microdevice. Lanes 1 and 2 in Fig. 5c show the 230 bp gene fragments obtained when using the thermal cycler and the PMMA microdevice, respectively. The intensity of the target amplicon obtained using the microdevice was approximately 97.2% of that obtained using the thermal cycler, based on an analysis conducted using the Image J software. Lanes 1 and 2 in Fig. 5d show the D1S80 loci amplified using the thermal cycler and the PMMA microdevice, respectively. For a target with size of approximately 500 bp, the intensity of the amplicon obtained using the microdevice was approximately 71.7% of that obtained using the thermal cycler. The sizes of the D1S80 locus, which is used for individual identification in forensic science, ranged between 369 and 801 bp.[28–31] In both cases, the target bands were successfully amplified using the PMMA microdevice with comparable intensities to those obtained using the thermal cycler. Owing to the high internal pressure maintained inside the microchannel throughout the sample flow, bubble generation was spontaneously suppressed during the heated operation.

Conclusion

In this study, we presented an innovative technology for the reliable and uniform flow of a liquid inside a microchannel over 2 m long under freely adjustable operation conditions using a portable plastic syringe. The use of a bulky mechanical pump requiring external electrical power supply was completely replaced by simple hands-on operation, which was sufficient to produce a driving force for transporting the liquid for performing a flow-through PCR on a microdevice. The high pressure generated inside the microchannel successfully resisted bubble formation even under the heated condition, and sample loss was prevented owing to the intrinsic low-gas-permeability of the PMMA. Using this system, two major issues associated when performing a flow-through PCR on chip, such as bubble formation and sample loss, was resolved. The introduced strategy can be widely applicable as a convenient tool, free of electrical input and bulky pumping apparatus such as syringe pump, in various fields of research where stable sample propulsion is required, such as when performing flow-through PCR directly on-site inside a simple serpentine microchannel, greatly enhancing fabrication easiness and device portability.

Acknowledgements

This research was supported by Basic Science Research Program through the National Research Foundation of Korea (NRF) funded by the Ministry of Science, ICT & Future Planning (2014R1A1A3051319). This research was also supported by the Gachon University research fund of 2014 (GCU-2014-0195).

Notes and references

1 H. T. G. van Lintel, F. C. M. van de Pol and S. Bouwstra, *Sens. Actuators*, 1988, **15**, 153–167.
2 J. G. Smits, *Sens. Actuators, A*, 1990, **21–23**, 203–206.
3 N. J. Graf and M. T. Bowser, *Lab Chip*, 2008, **8**, 1664–1670.
4 K. Handique, D. T. Burke, C. H. Mastrangelo and M. A. Burns, *Anal. Chem.*, 2001, **73**, 1831–1838.
5 S. Santra, P. Holloway and C. D. Batich, *Sens. Actuators, B*, 2002, **87**, 358–364.
6 J. Xie, J. Shih, Q. Lin, B. Yang and Y.-C. Tai, *Lab Chip*, 2004, **4**, 495–501.
7 P. Woias, *Sens. Actuators, B*, 2005, **105**, 28–38.
8 M. Yang, S. Sun, H. A. Bruck, Y. Kostov and A. Rasooly, *Lab Chip*, 2010, **10**, 2534–2540.
9 C. Lui, S. Stelick, N. Cady and C. Batt, *Lab Chip*, 2010, **10**, 74–79.
10 H. Lai and A. Folch, *Lab Chip*, 2011, **11**, 336–342.
11 K. Pitchaimani, B. C. Sapp, A. Winter, A. Gispanski, T. Nishida and Z. H. Fan, *Lab Chip*, 2009, **9**, 3082–3087.
12 T. Naito, R. Arayanarakool, S. L. Gac, T. Yasui, N. Kaji, M. Tokeshi, A. van den Berg and Y. Baba, *Lab Chip*, 2013, **13**, 452–458.
13 G. Münchow, D. Dadic, F. Doffing, S. Hardt and K.-S. Drese, *Expert Rev. Mol. Diagn.*, 2005, **5**, 613–620.
14 S. Chakraborty, *Lab Chip*, 2005, **5**, 421–430.
15 I. K. Dimov, L. Basabe-Desmonts, J. L. Garcia-Cordero, B. M. Ross, A. J. Ricco and L. P. Lee, *Lab Chip*, 2011, **11**, 845–850.
16 P. Kauffman, E. Fu, B. Lutz and P. Yager, *Lab Chip*, 2010, **10**, 2614–2617.
17 H. Noh and S. T. Phillips, *Anal. Chem.*, 2010, **82**, 8071–8078.

18 E. Fu, B. Lutz, P. Kauffman and P. Yager, *Lab Chip*, 2010, **10**, 918–920.
19 L. Qin, O. Vermesh, Q. Shi and J. R. Heath, *Lab Chip*, 2009, **9**, 2016–2020.
20 W. Wu, K.-T. Kang and N. Y. Lee, *Analyst*, 2011, **136**, 2287–2293.
21 W. Wu, K. T. L. Trinh and N. Y. Lee, *Analyst*, 2012, **137**, 983–990.
22 W. Wu and N. Y. Lee, *Sens. Actuators, B*, 2013, **181**, 756–765.
23 W. Wu and N. Y. Lee, *Anal. Bioanal. Chem.*, 2011, **400**, 2053–2060.
24 W. Wu, K. T. L. Trinh and N. Y. Lee, *Analyst*, 2012, **137**, 2069–2076.
25 C.-W. Tsao and D. L. DeVoe, *Microfluid. Nanofluid.*, 2009, **6**, 1–16.
26 D. J. Beebe, G. A. Mensing and G. M. Walker, *Annu. Rev. Biomed. Eng.*, 2002, **4**, 261–286.
27 H. H. Tran, K. T. L. Trinh and N. Y. Lee, *J. Chromatogr. B: Anal. Technol. Biomed. Life Sci.*, 2013, **936**, 88–94.
28 B. Budowle, R. Chakraborty, A. M. Giusti, A. J. Eisenberg and R. C. Allen, *Am. J. Hum. Genet.*, 1991, **48**, 137–144.
29 R. Roy, *Forensic Sci. Int.*, 1997, **87**, 63–71.
30 J. M. Hayes, B. Budowle and M. Freund, *J. Forensic Sci.*, 1995, **40**, 888–892.
31 N. Y. Lee, M. Yamada and M. Seki, *Anal. Bioanal. Chem.*, 2005, **383**, 776–782.

3.5 Wu *et al.* (2015)

Wenming Wu, Kieu The Loan Trinh and Nae Yoon Lee, "Flow-through polymerase chain reaction inside a seamless 3D helical microreactor fabricated utilizing a silicone tube and a paraffin mold", Analyst, 2015,140, 1416-1420. (SCI indexed, IF = 4.107) Hot article in Analyst (Jan. 2015). **(First author)**

This cooperated project is done with Prof. Nae Yoon Lee of Gachon University in Korea, and Prof. Manz provides sincere encourage and supports for such international cooperative project.

Authorship Contributions

Wenming Wu: participate in research design, conduct experiment, perform data analysis, and write the manuscript

Kieu The Loan Trinh: conduct experiments

Nae Yoon Lee: participate in research design, perform data analysis, and modify the manuscript

This work affirms diffusion pump as an efficient approach in self-activated & inhomogeneous liquid delivery for long-distance microchannel of 3D helical microreactor, while syringe pump as an efficient approach in homogeneous liquid delivery for long-distance microchannel of 3D helical microreactor.

Here, I develop the most simple and portable micro reactor until today, for continuous Polymerase Chain Reaction. The fabrication method, fabrication material and device structure are new trial in structuring microfluidic system. This reactor needs only one heater to realize the complicated reacting conditions in Polymerase Chain Reaction, which is the most important reaction is modern science. This system greatly simplifies the temperature control by utilizing a single heater, and therefore, downsizing the overall size of the device. Target amplicons are

successfully amplified simultaneously with high reproducibility, confirming stable sample injection performance and reliable temperature control inside the microdevice. The proposed schemes could enhance the way for device miniaturization, process simplification, and a significantly reduced cost.

Two kinds of strong pumping are tested in microfabricated 3D spiral device. One is directly through the usage of syringe pump, which can provide stable flow inside the 3D microstructure (Fig. 3, article 5). However, even if syringe pump is the most commonly used way to transport sample in microfludic area today, this system is energy consuming, quite giant and not portable at all. The usage of syringe pump increases a lot of additional space to the micro system. To avoid this shortcoming, diffusion pump is also tried to replace fussy syringe pumping systems frequently used by most micro systems. The special gas permeable property of silicon tube is critical for such kind energy free pumping. Based on earlier experiments, some other non-permeable tubes can't provide such energy free pumping effect if using same operation as silicon tube. So silicon tube instead of other non-permeable tubes is one prerequisite of self-powered diffusion pump. Besides the high elasticity and easiness of purchase, this is another reason why I select silicon tube than other materials for fabricating device here. As a result, an extremely compact 3D micro device with self-powered pumping ability for micro continuous PCR is fabricated (Fig. 5). Different from other self-activated micropumps including capillary pumping, vacuum pumping, Paper-based microfluidic pumping, diffusion pump is strong enough to handle micro continuous PCR without interrupted by high denature temperature, long channel distance as Ill as the gravity of sample flowing up and down the 3D channel.

Volume 140 | Number 5 | 7 March 2015 | Pages 1361–1748

Analyst

www.rsc.org/analyst

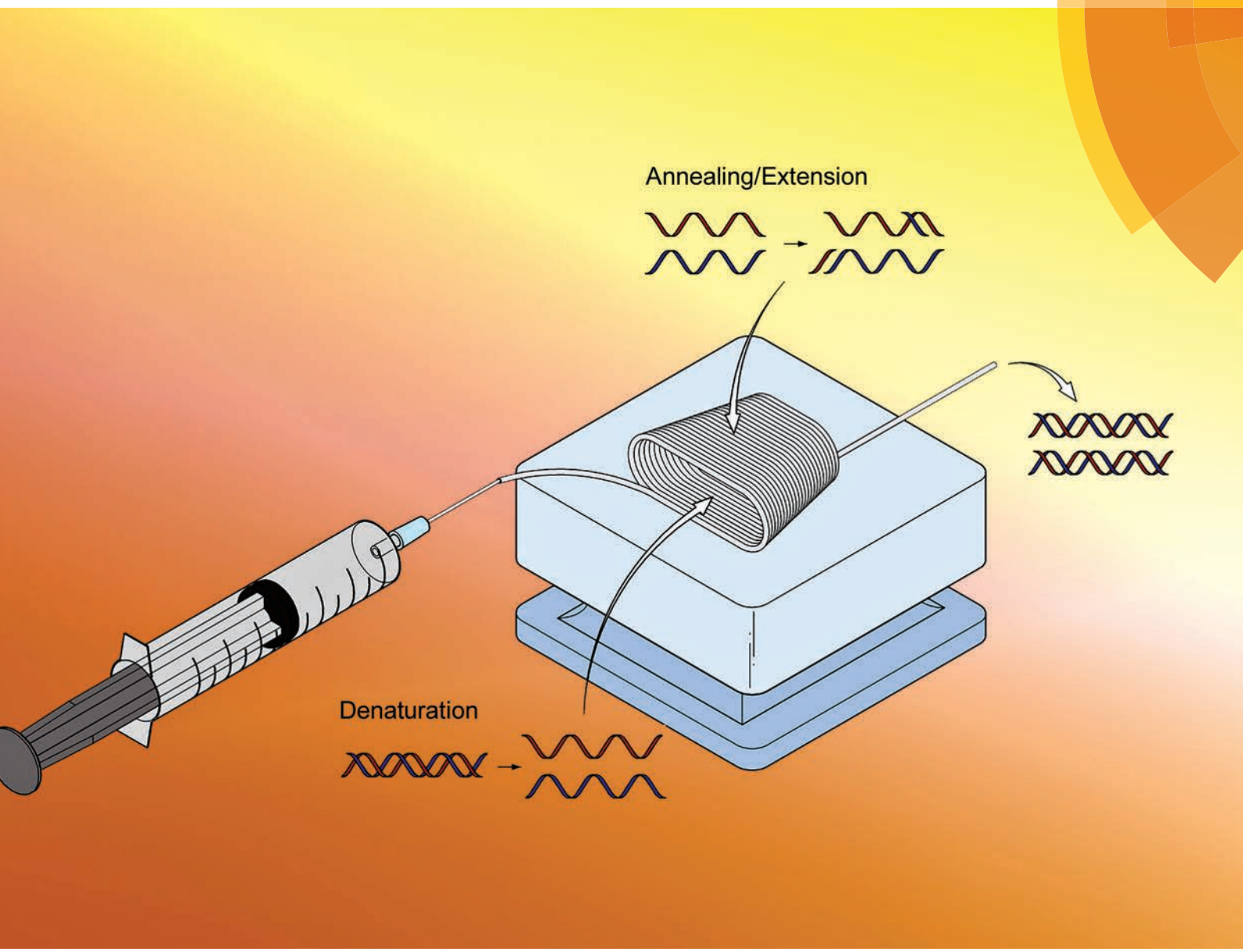

ISSN 0003-2654

ROYAL SOCIETY OF CHEMISTRY

COMMUNICATION
Nae Yoon Lee *et al.*
Flow-through polymerase chain reaction inside a seamless 3D helical microreactor fabricated utilizing a silicone tube and a paraffin mold

Analyst

COMMUNICATION

View Article Online
View Journal | View Issue

Cite this: *Analyst*, 2015, **140**, 1416

Received 12th September 2014,
Accepted 12th December 2014

DOI: 10.1039/c4an01675k

www.rsc.org/analyst

Flow-through polymerase chain reaction inside a seamless 3D helical microreactor fabricated utilizing a silicone tube and a paraffin mold†

Wenming Wu,‡[a] Kieu The Loan Trinh[a] and Nae Yoon Lee*[a,b]

We introduce a new strategy for fabricating a seamless three-dimensional (3D) helical microreactor utilizing a silicone tube and a paraffin mold. With this method, various shapes and sizes of 3D helical microreactors were fabricated, and a complicated and laborious photolithographic process, or 3D printing, was eliminated. With dramatically enhanced portability at a significantly reduced fabrication cost, such a device can be considered to be the simplest microreactor, developed to date, for performing the flow-through polymerase chain reaction (PCR).

Recent developments in micro Total Analysis Systems (μTAS) have provided a powerful experimental platform, which has benefited from the advent of soft lithography and photolithography. These techniques have enabled a dramatic increase in the speed of fabrication of two-dimensional (2D) microchannels and microdevices.[1–3] Compared with 2D systems, three-dimensional (3D) microfluidic systems are superior to many processes such as solution mixing,[4,5] 3D cell culturing and drug screening,[6,7] chemical reactions,[8] cell separation and sorting,[9,10] and controlling double emulsification.[11] Nevertheless, the traditional 3D fabrication process, termed as the "stacking method", is laborious and time consuming.[12–17] Furthermore, 3D helical microchannels are difficult to fabricate using this method. To overcome this problem, Wu *et al.* described a mechanical method for fabricating 3D microfluidic networks,[18] as an alternative to the traditional "stacking method". Although 3D helical microchannels can be fabricated with this method, its shortcoming is that all "joining channels must be done by hand", thus it requires a "certain amount of manual work", as described by the author.

One objective of this study is to find a much easier method to fabricate a 3D helical microchannel. An apparent advantage of the 3D helical microchannel lies in its outstanding superiority, compared with the traditional 2D microchannel, for performing the flow-through polymerase chain reaction (PCR). We find that a single commercial hot plate is sufficient for performing a typical PCR with a 3D helical microchannel, whereas traditional 2D microdevices require multiple heating blocks[19–21] or bulky heating accessories.[22–24] Because of the efficient utilization of space in the vertical direction, the footprint of a 3D helical microreactor can be much smaller than that of traditional 2D microdevices, where the microchannels lie on a planar surface.[25–27] The size of a 3D helical microreactor can also be controlled to fulfill different requirements and purposes, by varying the parameters of the component, in this case, a silicone tube. A thin silicone tube (i.d. 0.3 mm) has a thickness comparable to that of a coin.

The pumping system is an important component of any microdevice. Since pumping is required for efficient actuation of the microreactor, the pumping system is also studied here. Despite the numerous breakthroughs in research achieved so far, most pumping systems applicable for the "lab on a chip", or for microreactors, are bulky.[28–30] In the course of investigations into micropump simplification, capillary pumping,[31,32] vacuum pumping,[33] and paper-based pumping[34–36] have been developed in recent years. Nevertheless, for some processes, such as flow-through PCR, the required length of the microchannel is too long (over 2 m).[37] Therefore, the development of a miniaturized pump that can be coupled with a flow-through PCR microdevice is urgently needed to enhance the portability of the overall microsystem.

We examined two kinds of pumping systems for the operation of the 3D helical microreactors developed in this study. One is the commercially available syringe pump commonly used by many researchers. Despite its widespread application in microfluidic devices, this system is both energy consuming and bulky, which limits its portability. To avoid these shortcomings, we have developed a self-actuated and energy-free portable micropump to couple with the 3D helical microreac-

[a]*Department of BioNano Technology, Gachon University, 1342 Seongnam-daero, Sujeong-gu, Seongnam-si, Gyeonggi-do 461-701, Korea. E-mail: nylee@gachon.ac.kr*
[b]*Gachon Medical Research Institute, Gil Medical Center, Inchon, 405-760, Republic of Korea*

†Electronic supplementary information (ESI) available. See DOI: 10.1039/c4an01675k

‡Current address: Mechatronics department, University of Saarland, Saarbrücken, Germany & KIST Europe GmbH, Campus E7.1, 66123 Saarbrücken, Germany

tor.[38] We find that gas permeability is a critical factor. Based on our experiments, we have found that a gas-impermeable tube cannot offer the driving force for pumping that is available with a gas-permeable silicone tube. Therefore, the use of a gas-permeable tube is a prerequisite to realize self-actuated, energy-free pumping. Since the silicone tube is a gas-permeable duct, the air molecules captured inside the fluidic conduit will diffuse through the wall of the silicone tube to the atmosphere. A large volume of air, at higher than atmospheric pressure, is contained inside the disposable syringe that is connected to the inlet of the silicone tube. Since an incomparably large amount of air is contained in the syringe closer to the inlet, air diffusion rate at the posterior end of the sample plug is slower than that at the anterior end. As a consequence, air diffuses faster at the anterior end than the posterior end of the sample plug, resulting in the formation of a pressure gradient which acts as a driving force for sample propulsion toward the outlet. The speed of the fluid flow, however, eventually slows down because the pressure gradient between the ends of the sample plug gradually decreases as the area of air diffusion at the posterior end of the sample plug increases accordingly. This pumping is strong enough to propel the sample constantly over a long distance, even under the high temperature conditions needed for nucleic acid denaturation, and to overcome gravity, which restricts upward flow inside the 3D microchannel.

It is not easy to fabricate a 3D helical microchannel using traditional processes such as photolithography and replica molding. For this reason, development of an easier fabrication process is needed. One alternative is by the direct rotation of a flexible tube around a mold of predetermined shape and size. Since a silicone tube is flexible and possesses superior gas permeability, it is an ideal choice for fabricating a 3D helical microreactor. Moreover, the surface of silicone resembles that of poly(dimethylsiloxane) (PDMS), currently a popular material for fabricating microdevices. Thus, since the silicone tube offers application with potential as wide ranging as that of PDMS, we selected it as the fabrication material for our 3D helical microreactor. In the final step of the fabrication, the mold is removed to avoid its adverse effects on temperature distribution, such as undesirable heat transfer between the denaturation and annealing/extension regimes. Furthermore, removal of the mold substantially reduces the required distance between the denaturation and annealing/extension regimes, so that the overall footprint of the microreactor can be greatly decreased. Nevertheless, since the tubes are not fixed, the helical structure of the silicone tube can collapse during the mold removal process. This issue is easily resolved by gluing the tubes, using commercially available cyanoacrylate-based instant adhesive, before removing the mold. Fig. 1 shows the overall procedure for fabricating the 3D helical microreactor utilizing a silicone tube.

Fig. 2 shows photos of the various 3D helical structures actually fabricated. Fig. 2a shows the simple fabrication procedure. Based on the shapes of the cross-section, four types of helical structures were created, which includes a homogenous

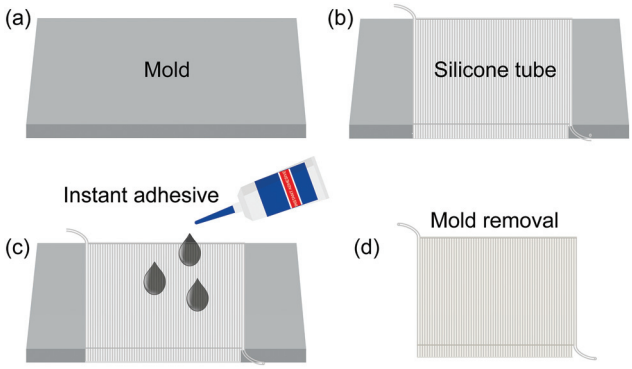

Fig. 1 Schematic illustration for the fabrication of a 3D helical microreactor. (a) Paraffin mold with a predetermined shape. (b) Rotation of the silicone tube around the paraffin mold. (c) Gluing of the silicone tube using cyanoacrylate adhesive. (d) Removal of the silicone tube from the mold.

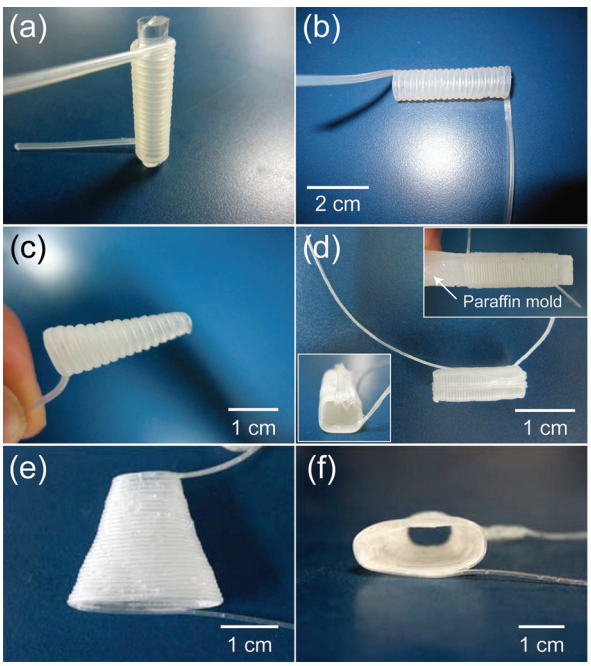

Fig. 2 Various 3D helical microreactors fabricated utilizing silicone tubes. (a) A silicone tube (0.5 mm ID/2.0 mm OD) rotated around a plastic cylindrical mold. (b) A circular silicone tube microreactor obtained from (a). (c) A conical silicone tube (0.5 mm ID/2.0 mm OD) microreactor fabricated using a plastic cylindrical mold. (d) A rectangular silicone tube (0.3 mm ID/0.64 mm OD) microreactor fabricated using a paraffin mold. (e) Top view of a trapezoidal silicone tube (0.51 mm ID/0.94 mm OD) microreactor fabricated using a paraffin mold. (f) Side view of (e) showing the gradient trapezoidal cross-section.

circular cross-section (Fig. 2b), a gradient circular cross-section (Fig. 2c), a homogenous rectangular cross-section (Fig. 2d), and a gradient trapezoidal cross-section (Fig. 2e and f). In addition to the different 3D cross-sections, these helical microreactors have three different tube diameters: 0.5 mm ID/2.0 mm OD (Fig. 2a–c), 0.3 mm ID/0.64 mm OD (Dow Corning)

(Fig. 2d), and 0.51 mm ID/0.94 mm OD (Dow Corning) (Fig. 2e and f). This demonstrates the ease with which 3D helical microreactors of different shapes and sizes can be produced by this method, a task that is always very laborious and time-consuming with traditional methods. When silicone tubes with larger diameters are used (*i.e.* 0.5 mm ID/2.0 mm), it is relatively easy to mechanically remove the silicone tube from the mold without damaging the helical structure (Fig. 2b and c). However, smaller diameter silicone tubes (*i.e.* 0.3 mm ID/0.64 mm OD) can be easily damaged during mechanical separation from the mold. This issue can be easily resolved by using paraffin as a mold material, because it can be melted by mild heating to temperatures as low as 60 °C. Paraffin is also highly advantageous because it can be easily shaped into various structures and sizes using appropriate frames, by pouring the molten material and re-solidifying it. In this study, the mold was melted away at 59 °C in an oven (Fig. 2d–f). Inset in Fig. 2d shows the photo of the paraffin mold used to fabricate a rectangular silicone tube microreactor.

From the four types of 3D helical microreactors fabricated, the rectangular silicone tube microreactor was chosen for performing the flow-through PCR (Fig. 3). The low thermal conductivity of air plays an important role in the dramatic reduction of temperature in the vertical direction of the microreactor. Simply by placing the microreactor on a single hot plate (temperature accuracy: ±0.3 °C) (MSH-20D; Daihan Science, Korea) adjusted to approximately 95.0 ± 0.2 °C (CV = 0.2% (n = 5)), the multiple rows of silicone tubes, glued together and arranged in parallel, which are in direct contact with the hot plate, participate in the denaturation process. The tubes at the top, with the greatest distance from the hot plate, will have a lower temperature, and participate in the annealing/extension process. The height of the microreactor is adjusted according to the annealing temperature.[14] Increasing the height of the microreactor will lower the annealing/extension temperature, and *vice versa*. Therefore, this microreactor can be readily employed to amplify targets requiring different annealing temperatures simply by varying the height. In this way, a single hot plate is sufficient for target amplification, contributing to device portability. Here, the annealing/extension temperature was controlled at 55.7 ± 0.2 °C (CV = 0.3% (n = 8)).

The reaction mixture contained a buffer composed of 0.2 mM dNTPs mixture, 0.075 U μL^{-1} *Taq* polymerase (Promega), 1.5 mg mL^{-1} BSA (Sigma), 1 μM forward and reverse primers, and 0.125 μg μL^{-1} DNA template. Agarose powder (BioShop) was used for agarose gel electrophoresis. The negative control contained everything in the reaction buffer except the DNA template. The primer sequences were as follows: 5′ CCG GCG AAC GTG GCG AGA AAG GAA GGG AAG AAA GC 3′ (forward) and 5′ TCG CCT TGC AGC ACA TCC CCC TTT CGC CAG C 3′ (reverse). A commercially available pGEM-3Zf(+) plasmid vector (Promega) was used as a target. A green-colored buffer solution was used for easy visualization of the sample flow. For performing the flow-through PCR, mineral oil was introduced at a rate of 10 μL min^{-1} using a syringe pump. Next, a 20 μL sample plug was introduced, followed by another plug of the mineral oil. In this way, the sample plug was completely encapsulated by the two plugs of the mineral oil. After the sample entered the microdevice, the flow rate was controlled at 2 μL min^{-1}. A 1 mL disposable plastic syringe was used to introduce the sample into the microreactor. No bubble was generated during the entire amplification process (Fig. 3). Fig. 3a–d show sample flow inside the microreactor under the actual heating condition, and Fig. 3d shows the overall experimental setup for performing the flow-through PCR, employing a rectangular silicone tube (0.3 mm ID/0.64 mm OD) microreactor, the width, length, and height of which were approximately 7.5, 19.2, and 6.5 mm, respectively. The total length of the silicone tube was 84 cm. Denaturation and annealing/extension were performed for 30 s, and a total of 30 thermal cycles were performed.

As shown in Fig. 4, the target (~230 bp) was successfully amplified using the rectangular silicone tube microreactor (lane 1) within 30 min, which corresponded well with the sample flow rate, confirming that the temperature was successfully controlled using a commercially available hot plate, and that the sample flow inside the microreactor was stable. In

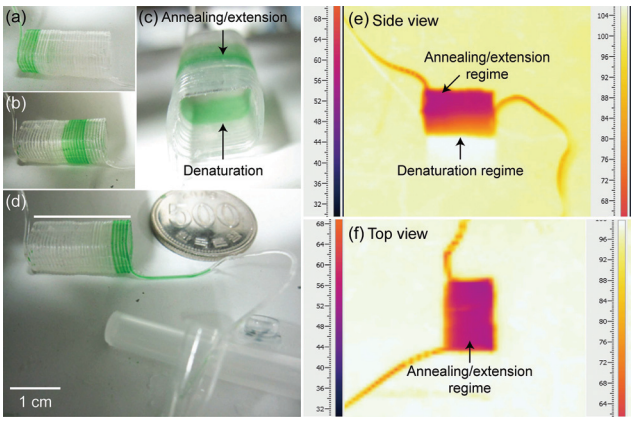

Fig. 3 (a–c) Photos showing sample flow inside the rectangular silicone tube microreactor under the actual heated conditions. (d) A photo showing the overall experimental setup. A syringe pump was used for sample actuation. (e, f) IR camera images showing temperature distribution. (e) Side view. (f) Top view.

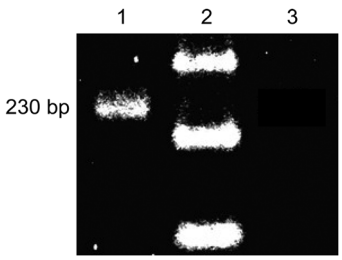

Fig. 4 Result of DNA amplification performed inside a rectangular silicone tube microreactor. Lane 1 shows the target amplicon (~230 bp) obtained using rectangular silicone tube microreactor. Lane 2 shows a 100 bp size marker. Lane 3 is a result of negative control.

comparison, no band appeared for the negative control experiment (lane 3). Lane 2 shows a 100 bp size marker.

Furthermore, we utilized one self-actuated, energy-free micropump to transport the sample inside the microreactor instead of using a syringe pump that relies on external electrical power to actuate the liquid.[28–30] The mechanism of this self-actuated, energy-free micropump is based on the air diffusion through the silicone tubes as described above, and in our previous study.[38] Because the pressure difference diminishes with the progress of the sample, we coupled this micropump, which is basically a disposable plastic syringe, to a microreactor (0.51 mm ID/0.94 mm OD) with a gradient trapezoidal cross-section. The length and height of the microreactor were 28.2 and 7.0 mm, respectively. The widths of the microreactor closer to the inlet and the outlet were 25 and 10 mm, respectively. The total length of the silicone tube was 1.5 m. A total of 30 thermal cycles were performed.

In this way, we intended to equalize the sample residence time for each thermal cycle, and hence, compensate for the decrease in the flow rate since the channels closer to the outlet possess a relatively shorter length than outer channels for the trapezoidal microreactor. The sequences involved in sample actuation using the self-actuated micropump are as follows. First, the outlet of the silicone tube microreactor was clamped to create an air-tight seal. Second, a 25 μL sample plug was drawn into the tip of the syringe, and the piston was pulled up to the end of the 3 mL syringe. Finally, the syringe was connected to the inlet of the silicone tube microreactor, and the piston was pushed forward to the 1.5 mL graduation of the syringe and fixed at this position. In this way, the initial syringe pressure propelling the sample was set to approximately 2 atm. Fig. 5a shows the overall experimental setup for conveniently performing the flow-through PCR with enhanced portability, employing common laboratory commodities. Fig. 5b and c show the results of temperature measurement. The denaturation was performed at 95.3 ± 0.2 °C (CV = 0.3% (n = 5)) for 30 s and annealing/extension was performed at 56.1 ± 0.4 °C (CV = 0.6% (n = 8)) for 30 s. The simplest form of

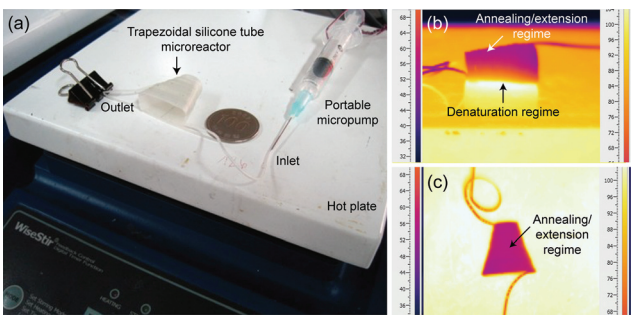

Fig. 5 (a) A photo showing the overall experimental setup for performing the flow-through PCR employing a trapezoidal silicone tube (0.51 mm ID/0.94 mm OD) microreactor coupled to a self-actuated micropump. (b, c) IR camera images showing temperature distribution. (b) Side view. (c) Top view.

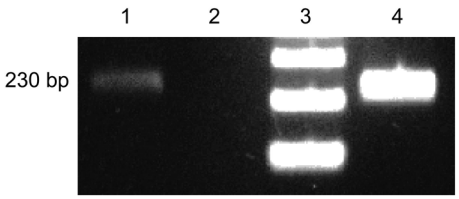

Fig. 6 Result of DNA amplification performed inside a trapezoidal silicone tube microreactor. Lane 1 shows the target amplicon obtained using the microreactor. Lane 2 is a result of negative control. Lane 3 shows a 100 bp size marker. Lane 4 is a result obtained using a thermal cycler.

the flow-through PCR microreactor, as well as the accessories for operation, were readily developed using a commercially available and cost effective silicone tube, a disposable syringe, and a hot plate. This PCR system is an even more simplified version of that introduced in our previous study,[38] in that it requires only one heater and a much smaller microreactor, it dispenses with all other costly fabrication procedures and time consuming operations, and does not require a trained specialist for fabrication, yet promises device portability ensuring potential for wide application. Some examples of previously developed flow-through PCR microdevices are given in Table S1 in the ESI.†

Fig. 6 shows the results for amplification employing the trapezoidal microreactor. The DNA template and PCR reagent were identical with those used inside the rectangular microreactor. The overall running time was 30 min. Lane 1 shows the target amplicon (~230 bp) obtained using the microreactor. No band appeared for negative control experiment (lane 2). Lane 3 shows a 100 bp size marker. Lane 4 is a result obtained using a thermal cycler. Although the intensity of the target amplicon was much brighter when using a thermal cycler, it was still clearly distinguishable when the microreactor was employed, and can be considered as a trade-off with the faster reaction.

In summary, this paper describes a simple approach for fabricating a seamless 3D helical microreactor utilizing a flexible silicone tube, and explores its potential for constructing a miniaturized PCR device. As compared to bulky conventional microfluidic systems, this technique ensures the fabrication of complex 3D structures in an extremely simple way using a paraffin mold and an elastic silicone tube. The method allows flexibility in device shape and channel dimension, while dispensing with laborious fabrication processes such as photolithography. Most beneficial is that all of the components, including the microreactor and operation accessories, can be constructed using commercially available laboratory commodities. Furthermore, bulky external apparatuses, such as a syringe pump and multiple heating blocks, which are inevitably required for flow and temperature control in a typical flow-through PCR, are unnecessary for these microreactors. The strategy introduced could pave the way for device miniaturization and portability at a significantly reduced cost.

Acknowledgements

This research was supported by Basic Science Research Program through the National Research Foundation of Korea (NRF) funded by the Ministry of Science, ICT & Future Planning (2014R1A1A3051319). This work was supported by the GRRC program of Gyeonggi province (GRRC Gachon 2014-A01) and the Public Welfare & Safety Research program through the National Research Foundation of Korea (NRF) funded by the Ministry of Science, ICT and Future Planning (NRF-2012M3A2A1051681).

Notes and references

1 J. C. McDonald, D. C. Duffy, J. R. Anderson, D. T. Chiu, H. Wu, O. J. A. Schueller and G. M. Whitesides, *Electrophoresis*, 2000, **21**, 27.
2 F. Hua, Y. Sun, A. Gaur, M. A. Meitl, L. Bilhaut, L. Rotkina, J. Wang, P. Geil, M. Shim and J. A. Rogers, *Nano Lett.*, 2004, **4**, 2467.
3 A. Tuantranont, T. Lomas, T. Maturos, A. Wisitsora-at, P. Thavarungkul, P. Kanatharana, W. Limbut and S. Loyprasert, *NanoBiotechnology*, 2006, **3**, 143.
4 N. Y. Lee, M. Yamada and M. Seki, *Anal. Bioanal. Chem.*, 2005, **383**, 776.
5 C.-S. Chen, D. N. Breslauer, J. I. Luna, A. Grimes, W.-c. Chin, L. P. Lee and M. Khine, *Lab Chip*, 2008, **8**, 622.
6 B. Ma, G. Zhang, J. Qin and B. Lin, *Lab Chip*, 2009, **9**, 232.
7 T. M. Keenan and A. Folch, *Lab Chip*, 2008, **8**, 34.
8 C. P. Park and D.-P. Kim, *J. Am. Chem. Soc.*, 2010, **132**, 10102.
9 S. C. Hur, A. J. Mach and D. D. Carlo, *Biomicrofluidics*, 2011, **5**, 022206.
10 S. Zheng, H. K. Lin, B. Lu, A. Williams, R. Datar, R. J. Cote and Y.-C. Tai, *Biomed. Microdevices*, 2011, **13**, 203.
11 F.-C. Chang and Y.-C. Su, *J. Micromech. Microeng.*, 2008, **18**, 065018.
12 J. R. Anderson, D. T. Chiu, R. J. Jackman, O. Cherniavskaya, J. C. McDonald, H. Wu, S. H. Whitesides and G. M. Whitesides, *Anal. Chem.*, 2000, **72**, 3158.
13 M. Zhang, J. Wu, L. Wang, K. Xiao and W. Wen, *Lab Chip*, 2010, **10**, 1199.
14 W. Wu and N. Y. Lee, *Anal. Bioanal. Chem.*, 2011, **400**, 2053.
15 D. T. Chiu, E. Pezzoli, H. Wu, A. D. Stroock and G. M. Whitesides, *Proc. Natl. Acad. Sci. U. S. A.*, 2001, **98**, 2961.
16 N. L. Jeon, D. T. Chiu, C. J. Wargo, H. Wu, I. S. Choi, J. R. Anderson and G. M. Whitesides, *Biomed. Microdevices*, 2002, **4**, 117.
17 B.-H. Jo, L. M. V. Lerberghe, K. M. Motsegood and D. J. Beebe, *J. Microelectromech. Syst.*, 2000, **9**, 76.
18 H. Wu, T. W. Odom, D. T. Chiu and G. M. Whitesides, *J. Am. Chem. Soc.*, 2003, **125**, 554.
19 T. Nakayama, H. M. Hiep, S. Furui, Y. Yonezawa, M. Saito, Y. Takamura and E. Tamiya, *Anal. Bioanal. Chem.*, 2010, **396**, 457.
20 Y. Sun, M. V. D. Satyanarayan, N. T. Nguyen and Y. C. Kwok, *Sens. Actuators, B*, 2008, **130**, 836.
21 M. U. Kopp, A. J. de Mello and A. Manz, *Science*, 1998, **280**, 302.
22 D. Pal and V. Venkataraman, *Sens. Actuators, A*, 2002, **102**, 151.
23 B. C. Giordano, J. Ferrance, S. Swedberg, A. F. R. Hühmer and J. P. Landers, *Anal. Biochem.*, 2001, **291**, 124.
24 Y. Tanaka, M. N. Slyadnev, A. Hibara, M. Tokeshi and T. Kitamori, *J. Chromatogr. A*, 2000, **894**, 45.
25 C.-H. Cho, W. Cho, Y. Ahn and S.-Y. Hwang, *J. Micromech. Microeng.*, 2007, **17**, 1810.
26 T. Fukuba, T. Yamamoto, T. Naganuma and T. Fujii, *Chem. Eng. J.*, 2004, **101**, 151.
27 Y. Schaerli, R. C. Wootton, T. Robinson, V. Stein, C. Dunsby, M. A. A. Neil, P. M. W. French, A. J. deMello, C. Abell and F. Hollfelder, *Anal. Chem.*, 2009, **81**, 302.
28 P. Watts and C. Wiles, *Chem. Commun.*, 2007, 443.
29 P. P. Lange, L. J. Gooβen, P. Podmore, T. Underwood and N. Sciammetta, *Chem. Commun.*, 2011, **47**, 3628.
30 V. J. Rico, J. L. Hueso, J. Cotrino, V. Gallardo, B. Sarmiento, J. J. Brey and A. R. González-Elipe, *Chem. Commun.*, 2009, 6192.
31 G. Münchow, D. Dadic, F. Doffing, S. Hardt and K.-S. Drese, *Expert Rev. Mol. Diagn.*, 2005, **5**, 613.
32 S. Chakraborty, *Lab Chip*, 2005, **5**, 421.
33 I. K. Dimov, L. Basabe-Desmonts, J. L. Garcia-Cordero, B. M. Ross, A. J. Ricco and L. P. Lee, *Lab Chip*, 2011, **11**, 845.
34 H. Noh and S. T. Phillips, *Anal. Chem.*, 2010, **82**, 4181.
35 H. Noh and S. T. Phillips, *Anal. Chem.*, 2010, **82**, 8071.
36 E. Fu, B. Lutz, P. Kauffman and P. Yager, *Lab Chip*, 2010, **10**, 918.
37 W. Wu, K.-T. Kang and N. Y. Lee, *Analyst*, 2011, **136**, 2287.
38 W. Wu, K. T. L. Trinh and N. Y. Lee, *Analyst*, 2012, **137**, 983.

3.6 Wu *et al.* (2016)

Wenming Wu and Andreas Manz, "The manufacture of chamber-embedded microdevice from Tilia platyphyllos leaf, and the biocompatibility assay at single cell level", *submitted*. **(First author)**

Authorship Contributions

Wenming Wu: participate in research design, conduct experiments, perform data analysis, and write the manuscript

Andreas Manz: participate in research design and modify the manuscript

This work affirms diffusion pump as an efficient approach in medium injection to leaf-inspired PDMS chip from Tilia platyphyllos, with artificial microchambers integrated into the whole ordered microvascular network.

The analog of blood vessels may become one potential and powerful tool in drug discovery, which should also rely on the fabrication of highly intensive microvascular networks to solve this problem related with drug transportation inside vessel. Previous reports have confirmed that both venations and vessels share similar architectural hierarchy in accordance with Murray's law. Thus, a microchip containing the microvascular networks that mimic natural leaves could be an efficient tool to realize such applications as drug-delivery inside blood circulation system, which can be rapidly and cheaply fabricated in a laboratory setting that I develop. Through diffusion pump, 500μL of cell suspension is transferred to a 2.5 ml sterilized syringe. The cells are then injected into central microchamber of the microchip (microchamber 1 in Fig. 2, article 6). By gradually pushing the syringe, the cell culture medium can slowly flow out of the inlet, outlet, as Ill as microchamber 2, 3, and 4 in Fig. 2. Because of the complicated microchannel

structure, air bubbles may easily form if other pumps are utilized. But the diffusion pump can push away all air bubbles formed during the injection step, and thus, the medium can fill in whole microvasculature, qualified for long term cell culture.

Cite this: DOI: 10.1039/c0xx00000x

www.rsc.org/xxxxxx

The manufacture of chamber-embedded microdevice from Tilia platyphyllos leaf, and the biocompatibility assay at single cell level

Wenming Wu and Andreas Manz*

Received (in XXX, XXX) Xth XXXXXXXXX 20XX, Accepted Xth XXXXXXXXX 20XX

DOI: 10.1039/b000000x

A biomimetic microvascular manufacture methodology to integrate microchambers into leaf-vein replicated vessel-like networks, is introduced in this technology innovation for the first time. The metastasis and deformation of human melanoma cells inside such bioinspired microvasculature are systemically studied, with cytomembrane tension, extracellular communication, microvilli, protonema configuration, and tethers' dynamic analyzed at single cell resolution. After loaded inside the microchambers of the microchip for 72 hours, few tumor cells begin to escape from microchamber into microvascular channels, mimicking cancer metastatic from the organs into vessel. Through another 72 hours monitor on cell mobility inside the microvascular channel, we find the microvasculature can dramatically influence both cell deformability and migration. Tethers' dynamic assay verifies extremely high cellular sensitivity to mechanical stimuli of the tiny-structures on the biomimetic microvascular wall, promising vascular surface-roughness may play important role during cancer metastasis between organs.

Ever since we firstly introduced "micro Total Analysis System" (also termed as "microfluidic system" or "lab on a chip") in 1990,[1] it has exhibited outstanding advantages in a wide range of areas, such as chemical sensing,[2] polymerase chain reaction,[3,4] drug discovery,[5,6] biophysical study,[7] and nanotechnology,[8] etc. The great potential of microfluidic in modeling functional microenvironmental equivalent for various pathophysiological assays also arouses tremendous attention of modern academia. Metabolism of all *in vivo* organs are sustained with continuous nutrient, signaling factor, and waste exchange by highly branched vessels which are mainly consisted with micrometer-scaled capillary microvascular transport networks. Similarly, microfluidic specializes in studies concerning micrometer-scaled channel, and thus can become an ideal platform in remodeling recirculation-based capillary networks for functional microenvironmental equivalent and further pathophysiological assays. Based in this concept, the utilization of microfluidic for recirculation-based organ-functionality, e.g., the so-called "organ on chip" system, has been successfully established during last several years.[9~12] In contrast with traditional cellular assay techniques such as the Boyden chamber assays and the Dunn chamber assays,[13] microfluidic also possesses many significant advantages, e.g., low volume consumption of reagent, low labour requirements, high biocompatibility, easy for real-time monitor, and practical for high-throughput analysis, etc. As a result, extensive microfluidic-based platforms have also been introduced for cell based studies, including cell migration,[14] cell fusion[15] and 3D cell culture,[16] etc.

Despite the brilliant achievements microfluidic engineers has gotten over last two decades, we should admit that microfluidic field remains in its infant[17] and correspondingly, there are lots of problems ahead to solve before microfluidic can finally grow up as a mature subject.[18] For instance, cancer metastasis to distant organs depends on complex transmigration interference with the microvasculature (e.g., vessel or vasa lymphatica), whereas reproducing such an *in vitro* microenvironmental equivalent of *in vivo* microvasculature remains a formidable challenge.[19~22] Because *in vivo* organs are interconnected by vessel which undertakes transport function of signaling molecules or motile cells, such important role of highly biomimetic microvascular networks shouldn't be neglected when modeling *in vitro* platform such as the "human on chip system" or the "tumor extravasation assay system". During last decade, big efforts have been contributed for constructing various types of microfluidic networks,[23~31] consisted of rectangular,[23~28] cylindrical[29~30] or both types[31] of cross-sectional microchannels.

About one century ago, pioneers including Hess and Murray successfully predicated that the optimized diameter relationship between the mother vessel and the daughter vessels, stating that the sum of the cubes of daughter vessels is equal to the third-power of mother vessel.[32~34] This relationship is now generally referred as Murray's law, which is the most successful law in summarizing the overall relationship of *in vivo* vessel until today. Because Murray's law is the most foundational architectural rule of vassal configuration, we should take it into account if we design artificial vessel for corresponding pathophysiological or biomedical study. And some pioneers already considered Murray's law when they designed artificial biomimetic microvascular networks.[35~37] Different from animal vessel, the overall configuration law behind the veinal microvascular networks of natural leaves was unknown for long term during human cognitive history. Only about one decade ago, it's firstly systemically clarified that the microvascular networks of natural vein obeys the same Murray's law as that of natural animal vessel.[38] Over the last decade, more and more evidences indicate that almost all natural vein obey Murray's law.[39] Besides the same overall configuration law that veinal

microvascular networks and vasal microvascular networks obey, veinal microchannels also share high structural consistency with vasal microchannels, e.g., circular cross-section for both cases. Both veinal and vasal microvasculature experienced millions of years' evolution, to best fulfil their same biological transport role essential for creatures survival. Inspired by this post, we evaluate that veinal microvasculature can become potential alterative of vassal microvasculature for recirculation-based biomedical study including "body in chip system" or "tumor metastasis analysis system".

Depending on this concept, we have previously developed a method for direct replication of whole-ordered microvascular networks from natural leaves into microfluidics, wherein a series of engineering characterizations (chemical stability, surface topography, 3D microchannel topology, and injection analysis, etc.) were systemically studied.[40] Herein, we improve this model by integrating microchamber (controllable shape, dimension and depth) into whole-ordered microvascular networks, to demonstrate the extravasation capabilities of human melanoma cells, which is highly life threatening[41] and cause 80% of deaths related to skin cancer.[42] We further rely in professional video processing for accurate and quantitative cellular biophysical analysis in single cell level, including cell microvilli, cell deformation, extracellular communication, cell division, cell mobility, and membranal local shear stress, etc., with improved resolution than most previous cell-based microfluidic platforms.[43-47] We believe the biomimetic microvasculature model here can become an alternative approach of traditional microsystems for tether studies.[48-51]

2 Experimental

2.1 Microchip fabrication

The overall schematic fabrication steps to replicate natural microvascular networks from real leaves into microfluidic chip, as well as to integrate multiple microchambers inside the networks is shown in Fig. 1. Firstly, the upside of fresh leaf is sequentially attached to single-side tape (tesa 57176-00 tesapack ultra-strong tr. 66 m: 50 mm) and double-side tape (tesa double side tape 10 m: 15 mm), which finally adhere onto the petridish (Mit 3 Nocken 391-0247), as shown in Fig. 1a. A 10:1 (w/w) mixture of the PDMS prepolymer and curing agent (SYLGARD 184; Dow Corning) is degased for half hour, and then poured inside the petridish containing the leaf master (Fig. 1b). Then PDMS prepolymer is cured at 45 ℃ for 24 hours, and peeled off from the leaf master (Fig. 1c). Then the PDMS replica is flipped over, and the microstructural surface is punched by commercial puncher (Fig. 2d). The diameter of the puncher determines the diameter of the microchamber, while the height of the PDMS replica in Fig. 1c determines the height of the microchamber in the final microfluidic chip (Fig. 1h). Then the microstructural surface of PDMS is covered with Norland optical resist (NOA 63), flipped over, and attached to one oxygen plasma treated petridish (Fig. 1e). NOA 63 should fill in all the microchambers of the PDMS replica in this step. After an UV exposure for 15min, the photoresist is cured and firmly bonded with the plasma treated petridish, but the PDMS replica can be easily removed, leaving the NOA-Petridish assembly as the master mold for further chip fabrication (Fig. 1f).

A 20:1 (w/w) mixture of the PDMS prepolymer and curing agent is then poured on the NOA master inside the petridish (Fig. 1g). Then PDMS prepolymer is cured at 80 ℃ for 30 min, and peeled off from the NOA master (Fig. 1i). Corresponding through-holes (2 mm) are punched into the PDMS replica at the positions of the inlets, outlets, and microchambers. After a further oxygen plasma treatment together with silicon-based substrates such as glass plate or PDMS sheet, the chip can be firmly bonded as shown in Fig. 1g. For some locations where PDMS and substrate are not tightly contacted, an additional pressure can be exposed for their tight contact, simply done by the finger. The power, the chamber pressure, and the exposure time during plasma treatment (Diener electronic: 0010915) are 70 W, 0.7 Torr, and 30 sec, respectively. Finally silicon tubes (i.d. 1.6 mm, o.d. 2 mm) are inserted into the ports of the inlet, outlet, and microchambers, for the introduction of fluid such as chemical solution or biological medium. After filled with fluorescein solution (1 mg/mL, with 0.01 % Tween80), the microchip is located inside a UV transmitter (VWR Gehoview Mini M: VWRVG\1015). An overall fluorescent image of the microchip patterns (1X magnification) is captured by a commercial CCD camera (Canon ED560D).

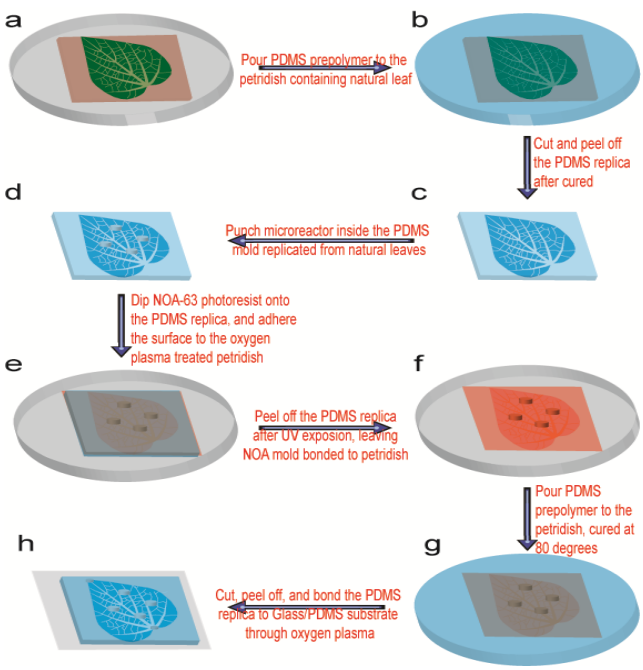

Fig. 1 Schematic fabrication steps of the microchambers integrated biomimetic microvascular networks from natural leaves. (a) The natural leaves adhere to the Petri dish through single-side tape and double-side tape. (b) PDMS pre-polymer is poured into the Petri dish. (c) After cured, PDMS replica is removed. (d) Holes are punched into the PDMS replica. (e) PDMS replica is coated with Norland optical adhesive (NOA63), which is then attached to another petridish followed by an UV exposure. (f) After PDMS replica is detached, the petridish-NOA hybrid master mold is left. (g) PDMS pre-polymer is poured into the Petri dish containing the hybrid template, cured at 80 ℃. (h) PDMS replica is boned with the glass or PDMS substrate through oxygen plasma treatment, with the microvascular channels easily modified by pressing the corresponding locations of the PDMS replica.

2.2 Cell seeding and culture in the microchip

Melanoma cells line (MEL-HO) are used in the experiments for the invasion assay inside the biomimetic microfluidic device. The cells are cultured in standard culture flasks containing RPMI medium (PAN-Biotech), supplemented with 10% fetal bovine serum (PAN-Biotech), 100 units/mL of penicillin, and 100 units/mL of streptomycin. An incubator is utilized to maintain the concentration of humidified CO_2 atmosphere and the incubation temperature to be 5% and 37 ℃, respectively. The culture medium is changed every three days before cells are seeded into the microfluidic device. During the harvest step, 0.05% Trypsin (PAN-Biotech) is used to digest and detach the cells from the culture flask. Density of the cell suspension is counted using the disposable hemocytometer (C-Chip Counter, Digital Bio), which is then centrifuged and adjusted to required concentration for the following microchip seeding. Centrifuged cells are resuspended with 15% FBS supplemented RPMI medium at 7.5×10^5 cells/ml. Cell viability is higher than 90%, based in the test by Trypan Blue Solution, 0.4% (aMRESCO®). Before the seeding of the cell, the microfluidic device is sterilized by autoclave at 121 ℃ for 20 min. Then 15% FBS supplemented RPMI culture medium is flushed into the microdevice, through the silicon tubes of the inlets, outles, and microchambers. Such microdevice is incubated overnight in 5% CO_2 at 37 ℃, to heighten the biological compatibility of the channel inner surface. Afterwards, 500 μL of cell suspension is transferred to a 2.5 ml sterilized syringe. The cells are then injected into central microchamber of the microchip (microchamber 1 in Fig. 2). By gradually pushing the syringe, the cell culture medium can slowly flow out of the inlet, outlet, as well as microchamber 2, 3, and 4 in Fig. 2. Through the sample injection technique here, the cells can be mainly seeded in the four microchambers of the microfluidic device, but cells are almost nonexistent inside the microvascular networks. Then the prepared microfluidic device is kept in an incubator in 5% CO2 at 37 ℃ for 3 days before migration analysis, to allow the cells to attach and grow on the bottom surface of microdevice.

2.3 Monitor of cell dynamic at single cell resolution

The on-stage microincubator is used for the real-time and long-term monitor of cell biophysical performance during migration, with CO_2 concentration and culture temperature stabilized to be 5% and 37 ℃ by a CO_2 controller (Bioscience Tools, CO2-500ML TC-MI) and a heating unit (Bioscience Tools, Temperature Controller TC-1-100-I), respectively. Before CO_2 enters the microincubator, it passes through a DI water bath firstly, to bring adequate atmospheric humidity into the microincubator necessary for healthy growth of cells. After microincubator is turned on, it's firstly maintained running for half hour to stabilize inner atmospheric consistence and temperature condition. Afterwards, the cell seeded microdevice is put inside the microchamber for long term under real-time monitor. Cell deformation and migration in response to the microvascular networks is assessed by inverted optical microscope (ZEISS Axiovert S 100) under the control of imaging software (ProgRes® CapturePro 2.8.8), with images taken at a fixed time interval of 1 frame/min. The images are captured by a commercial CCD camera (ProgRes® MF^{cool}), with a microscopic magnification of 100X and 320X, respectively. The 100X magnification can show the overall cell extravasation from microchamber into the biomimetic microvascular channels, while the 320X magnification can show more distinct biophysical details of single cell within a specific position of microchannel.

Because the border of microchannel is not obviously distinct with the rest of microstructure in original tracking video, we utilize Adobe Premiere to add black bordering line to the microchannel to heighten the channel display. Besides, Adobe Premiere is also utilized to add a series of other parameters to original video, including time code, text caption, scale bars, and indication arrows, etc., which can increase video readability. To visually display the overall cell behavior during a long term, the modified video is finally accelerated to 480X broadcast speed by Adobe Premiere. Concerned frames are also exported directly by Adobe Premiere, for further figure arrangement. As a result, compressive and dynamic cellular physiological details (e.g., microvilli, protonema, deformation, migration, extracellular communication, division, and cytomembrane shear stress, etc.) are distinguished concerning all the cells within the microscopic area,

3 Results and Discussion

3.1 Microchip characterization

There are one inlet, one outlet and four microchambers in the microchip here. As shown in Fig. 2a, the microvascular network of biomimetic microchip is the same with the vein of natural leaf, but with additional microchambers integrated into the microvascular networks. To more distinctly exhibit the structural details of the microchannels, both high resolution fluorescent microscopic image (emitting light 470nm, absorption light 530 nm) and high resolution optical microscopic images of the microvascular networks are taken at a magnification of 100X. As shown in Fig. 2b~f, the fluorescein solution can fill into the microvascular networks without any leakage, indicating a successful structural replication from leaf to microfluidic system. Furthermore, because the channel surface of natural biological vasculature is not highly smooth but a little rough, the inner surface of the microchannels fabricated here is a little coarse correspondingly, as shown in Fig. 2g~i. In contrast, in the case of the microchannels fabricated by most traditional techniques such as photolithograpy and laser ablation, their inner surface remains highly smooth under the same microscopic magnification times. This promises an obvious difference in microstructural surface between the microchannels fabricated by traditional methods and the microchannels fabricated here.

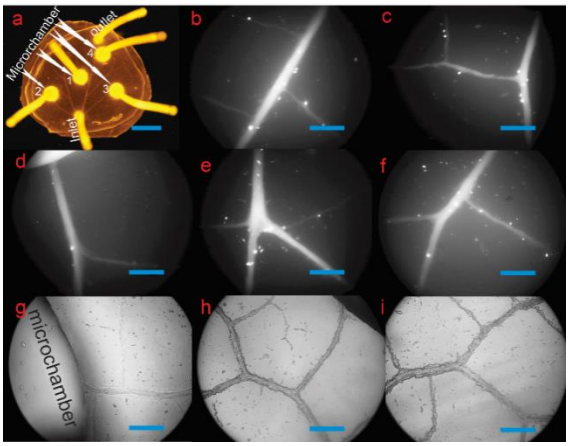

Fig. 2 Characterization of the biomimetic microvasculature model. (a) The overall fluorescent image of the microsystem filled with fluorescein. (b) ~ (f) High resolution fluorescent microscopic image of the microvascular networks at the magnification of 100X. (g) ~ (i) High resolution optical microscopic images of the microvascular networks at the magnification of 100X. Scale bar in (a), 1 cm; scale bars in (b) ~ (i), 200 μm.

3.2 Overall cell migration inside microvascular channel

Overall migration of cells inside the microvascular channel is displayed in Fig. 3，captured by optical microscope at 320X. The tumor cells are originally only seeded inside the microchamber and nonsexist inside the microvascular channel. After three days culture inside incubator, most cells remain restricted inside the border of microchamber, but few cells begin to extravasate from the microchamber into the microvascular channel. As shown in Fig. 3a, there is only one cell successfully extravasates from the microchamber into the microchannel in the third day. At its posterior site, the following cell is struggling to escape from the microchamber into the microchannel. If this following cell can finally escape form the microchamber, then it should overcome the tension drag from the interconnected cells inside the microchamber (for this point, detailed clarification will be illustrated in later section). It's noticeably that the configuration of the cells in different areas of the microvascular system is distinctly different. Most cells inside the microchamber are close-packed, with a spindle configuration. However, the cell located between the microchamber and microchannel has an elliptoid configuration instead of spindle shape. On the other hand, the cell located inside the microchannel has a similar spindle configuration as those inside the microchambers, but it's much longer and narrower.

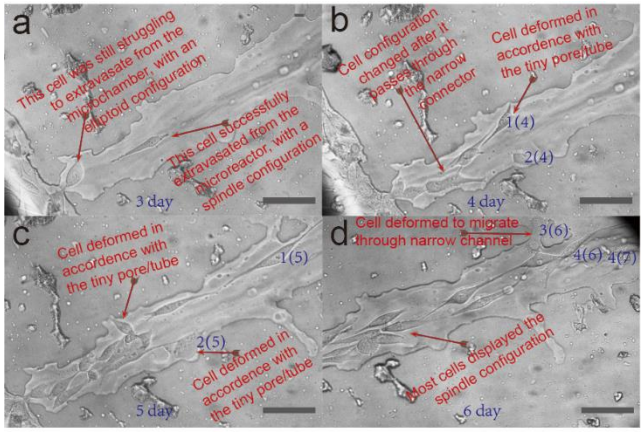

Fig. 3 Tissue-like anatomic microvascular networks for cell extravasation analysis. (a) Cell configuration inside the microvascular channel after three days culture. (b) The optical microscopic result of cell migration inside the microvascular channel after four days of cell culture. (c) The optical microscopic result of cell migration inside the microvascular channel after five days of cell culture. (d) The optical microscopic result of cell migration inside the microvascular channel after six days of cell culture. Scale bars, 100 μm.

Fig. 3b~d shows the optical imaging result of cell migration inside the microvascular channel, after four, five and six days of cell culture inside the microchamber. The distance between the frontier cell and the microchamber border becomes farer and farer as the time passes, promising a sustained cell migration behavior after the tumor cells successfully extravasate from their originally loaded microchamber, as shown in Fig. 3a. The distance between the frontier cell and the micoreactor border at the third, the fourth, the fifth and the sixth day is measured to be 237 μm, 320 μm, 665 μm, 753 μm, respectively. Correspondingly, the daily migration velocity from the third day can be calculated to be 83 μm/day, 338 μm/day, and 210 μm/day, respectively. As a result, the cell migration velocity is highest between the fourth day and the fifth day, but is lowest between the third day and the fourth day, which reveal dramatic varies of daily migration velocity along the biomimetic microchannel as the time passes.

As compared with the microchannels containing highly smooth inner surface which are fabricated by traditional techniques, this is one obvious difference because the overall migration velocity is much more stable as the time passes inside traditional microchannels.[52,53] Such dramatic overall velocity variability inside the biomimetic microvascular channel, as we hypothesized here, is caused by its rough inner surface.

It's noticeably that some tiny pores/tubes are located on the inner surface of microvascular channel, which may dramatically affect the cell behavior during its migration process. For easier recognition, several cells are labeled as cell 1(4), 2(4), 1(5), 2(5), 3(6), 4(6) and 4(7), as shown in Fig. 3b~d. During the cell migration process, it's found that the two frontier cells: 1(4) and 2(4), deform in accordance with thy tiny pore located on the inner surface of the microchannel, and thus, their orientation aren't in parallel with the microchannel during this time interval. As a result, the overall migration velocity along with the microchannel decreases to only 83 μm/day. Between the fourth day and the fifth day, cell 1(4) changes to cell 1(5). Depending on our hypothesis, because there is no tiny pore to activate the deformation of this cell,

it can keep migrating with cell orientation and migration direction in parallel with the microchannel, and thus it migrates much faster (338 μm within one day) than previous day. On the other hand, cell 2(4) can only move a much smaller distance during the same time interval. This is because there is another pore located on the inner surface which activate the cell 2(4) deformed to cell 2(5). Because the overall migration distance is determined by cell 1(4) and cell 1(5), which is 338 μm, the migration velocity is measured to be as high 338 μm/day. As for the cell migration between the fourth day and the fifth day, it's noticeably that there is another tiny tube located on the microvascular channel, which activates the cell inside the microchannel to deform to cell 3(6) and thus influence the cell migration along the microchanel. So the overall migration velocity decreases from 338 μm/day to 210 μm/day. Nevertheless, there are other frontier cells like 4(6) and 4(7), with their direction in parallel with the microchannel. This makes its overall migration velocity higher than velocity between the third day and the fourth day. The cells can finally detach from the tiny pores after it fail to pass through, as shown in the case of cell 1(4), 2(4), and 2(5) in Fig. 3b~d . In contrast, the cells can pass through the tiny tube, as shown in the case of cell 4(5) in Fig. 3d.

3.3 Overall cell deformation inside microvascular network

It's found that large amount of melanoma cells try to deform their shapes in coincident with tiny structures of microvascular channels, revealing strong interference of the tiny microvascular structures on the behavior of human melanoma cells inside the network. There are large amounts of tiny pores/tubes on the inner surface of the biomimetic microvascular networks, as shown in Fig. 4. All these tiny pores/tubes are different in their shapes, with dimensional variance ranging from several micrometers to tens of micrometers. After the cells are seeded and cultured inside the microchambers for several days, the tumor cells begin to extravasate from the microchambers into the microvascular networks. In the meanwhile, the tiny pores/tubes on the inner surface tend to influence the cell behavior by activating the cells to deform in consistent with their shapes and dimensions. For instance, the tiny pore in Fig. 4a looks like a converted shoe, which activates the tumor cell to deform to rare shoe-like configuration, with three feelers extruding towards three different directions at 120 °intersection angle. In contrast, a shoe-like configuration here is impossible to come out in traditional culture flask based system, and most cells display a spindle configuration if cultured inside flask, petridish or traditional microchip which have smooth inner channel surface (data not show). Similarly, the cell in Fig. 4b displays a mushroom-like configuration, with an umbellate cover and an elliptic root embedded inside the tiny pore, which is also very rare compared with the cells cultured inside traditional devices. In Fig. 4c, there are two tiny pores located on the channel surface. One pore looks like a bullet, while the other looks like an equilateral triangle. As a result, the two cells deform in consistent with these two kinds of pore shapes, correspondingly. All cells in Fig. 4a~c have finished the whole deformation process stimulated by the tiny pores. In contrast, the cells in Fig. 4d~f are still trying to deform into the same shape as the tiny pores. There are two cells in Fig. 4d. The configuration of the bottom cell has deformed partially in consistent with the tiny pore. On the other hand, the upside cell has orientated its direction in accordance with the tiny pore, for following deformation in response to the tiny pore. In Fig. 4e, the cell is still trying to deform and migrate into the tiny pore. In Fig. 4d, the cell has already migrated into the tiny pore. Nevertheless, it still needs more time to deform more in consistent with the tiny pore

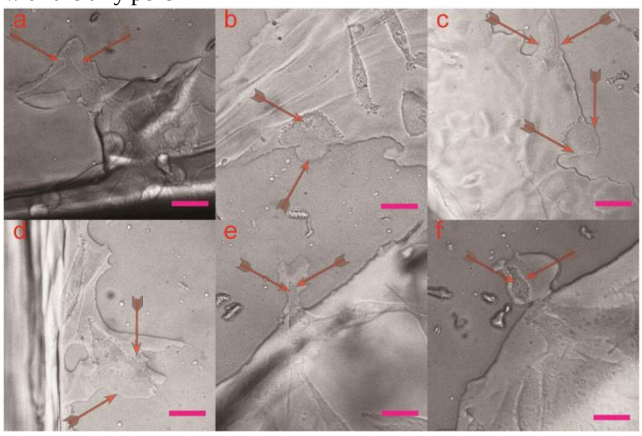

Fig. 4 Cell deformation inside leaves aspired biomimetic microvascular networks. (a) The shoe-like deformational configuration of cell. (b) The mushroom-like deformational configuration of cell. (c) The bullet-like and equilateral-triangle-like deformational configurations of cell. (g) ~ (i) Tumour cells are still undergoing deformation process in accordance with the shapes as the different tiny pores. Scale bars, 50 μm.

Because of the text limit, we only show several representative results (Fig. 4) to demonstrate cell deformation in response with the tiny pores of the microvascular networks. Nevertheless, cell deformation widely exists all through the microvascular networks (ESI 1), especially in the locations with tiny pores/tubes. This promises it's a general rule that the tiny pores/tubes of the microvascular networks can dramatically activate the deformation of tumor cells during cell extravasation.

3.4 Tethers' dynamic assay at single cell resolution

Through previous results, it's clearly seen that tumor cells display obviously high deformability inside this venial-inspired biomimetic microvascular networks, but are dramatically unstable concerning migration velocity. To explain the mechanism behind these phenomena, we depend on a video processing model for live monitor of cellular dynamic inside the microvascular networks, at single cell resolution. Through this model, we prove that tethers-mediated deformation mechanism is the reason why melanoma cells can so easily deform in accordance with tiny pores/tubes inside the microvascular networks. Furthermore, we find tethers can be intensively activated by both cell division and cell motion.

3.4.1 Tethers' activation by tiny microvascular structure

After six days of cell culture inside the microfluidic device (Fig. 3), the microchip is put inside the microincubator, with the video recorded by optical phage contrast microscope at 320X. The focused area is the same as that in Fig. 3. The time code starts from the moment (00:00:00) when the video begins to be recoded (144 h after cells loaded inside the microchip).

Various configurations of the tethers of tumor cells are shown in Fig. 5. Easily seen, cell tethers look like tiny ropes extended outside of the cell. The tethers of the cell display obvious

hyperactivity. As shown in Fig. 5, the tether direction, tether length and tether shape of both cell A and B are of big variance from time to time. In contrast, the main body of cell doesn't reveal any changes at all during the same period. Such hyperactivity of tethers can ensure melanoma cell to sense all signals from different directions of the microvasculature. Because of this, the cell doesn't leave out any signals from the stimulant in all directions around, and can finally moves from its original position as indicated in Fig. 5a~e, to one tiny pore on its top left of the channel surface, as shown in Fig. 5f~i. After the cell moves to the target position in Fig. 5f~i, new cell tethers grow out to sense other signals for further movement. Because the cell fails to pass through the tiny pore, it finally detaches from the tiny pore and returns back to the microchannel, as shown in Fig. 5j. Time lapsed tether formation of cell B is indicated in Fig. 5k~t, displaying similar hyperactivity as cell A.

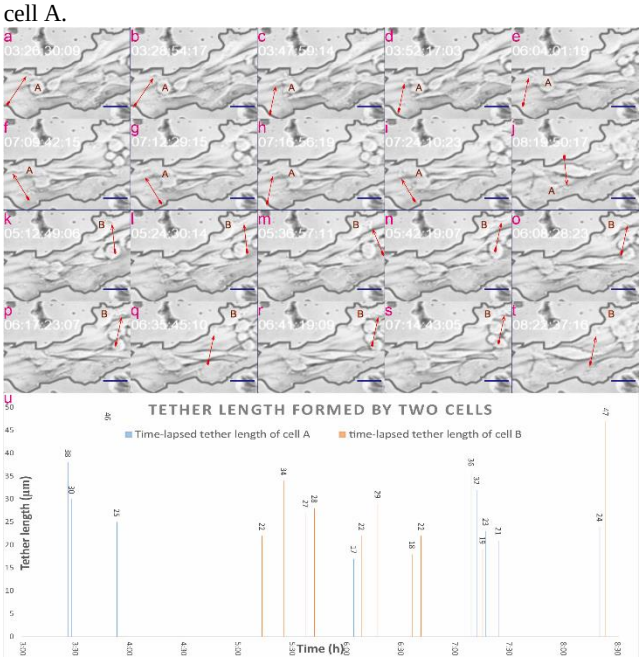

Fig. 5 Tethers' activation by tiny microvascular structure. (a) ~ (g) Tether variability of cell A. (k) ~ (t) Tether variability of cell B. The red arrows indicate the formation of tethers. Time codes displayed in each frame indicate the time when the frame is captured. (u) Tether formation and the hyperactive dynamic inside the biomimetic microvasculature: length of tethers formed by two independent melanoma cells inside the venially inspired microvascular networks. Scale bars, 50 μm.

The length of tether length of cell A and cell B is also calculated, as shown in Fig. 5u, covering timing period from 3: 00 to 8: 00 (h), with average tether length of cell A and cell B estimated to be 29 μm and 27 μm from ten spots. The standard derivation (STDEV) of tether length formed by cell A and cell B are 8.87 and 8.67, while variation coefficient (CV) are 30.7% and 33.2%, respectively. Depending on the video processing technique introduced here, a visual display of the dynamic behavior of cell tethers is provided in the supplementary material (ESI 2).

3.4.2 Tethers' activation by cell motion

Inhomogeneous migration velocity exists not only between different cells, but also within same cell across different time-periods. As indicated in Fig. 6, the total migration distance of three different cells: cell 1, 2 and 3 during 2.5 hours of monitor period are 9.64 μm, 115.67 μm and 174.07 μm, with average migration velocity to be 3.85 μm/h, 46.27 μm/h and 69.27 μm/h, respectively. Besides, time-lapsed migration velocity displays big variance within same cell, wherein it's highest between 6:30~6:45 for cell 3 but 8:00 ~ 8:14 for cell 2.

Based in Fig. 6, the migration velocity of cell 2 during 8:00~8:15 can reach 104.93 μm/h, which is 2.3 times of the average migration velocity of the monitor period between 5:45 and 8:15. This phenomenon also support our aforementioned hypothesis that the tiny pore of the microvasculature can strongly activate the formation of cell tethers, and further activate the cell deformation and migration. This is the reason why cell 1 reveals much lower migration activity compared with cell 2 and cell 3, too. The location of cell 1 is almost in the center of micro channel, and thus lack stimulation signal from the channel surface to activate high amounts of cell tethers on its membrane.

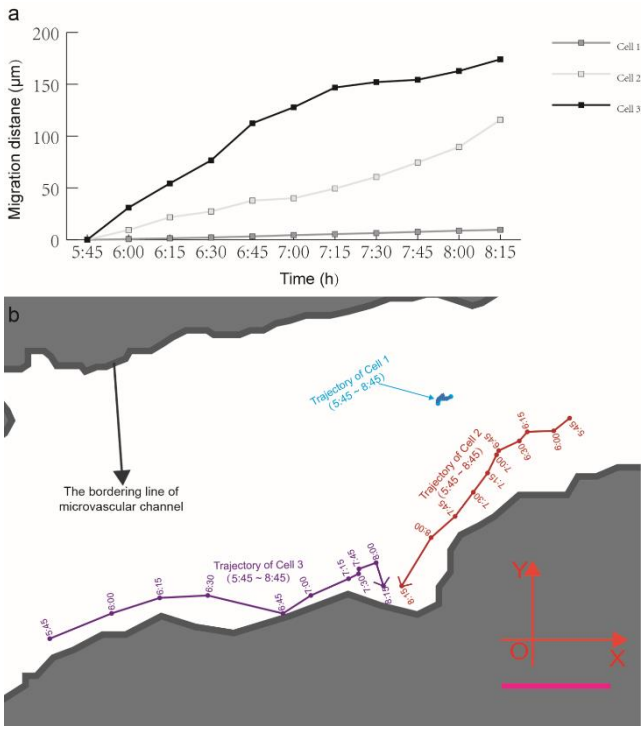

Fig. 6 Quantitative analysis of time-lapsed cell trajectory and migration distance at single cell level. a) Time-lapsed migration distance of three cells inside the microvascular channel. b) Time-lapsed migration trajectory of three cells inside the microvascular channel. The blue, red and purple curve represent the trajectory of cell 1, 2 and 3 inside the microvascular channel with an internal of 15 mins, during the recording period from 5:45 to 8: 15 (ESI 3). Scale bar, 50 μm.

Based in dynamic monitor of three corresponding tumor cells, we also confirm that when the cell begins to migrate, the cell tethers become extremely active. On the contrary, when the cell stays still, its tethers are inactivate. As shown in Fig. 7, no tethers exist in cell 1 during the whole monitoring period. As a result, cell 1 stays in same position during whole monitoring process. On the contrary, tethers form in cell 2. Because of this, cell 2 migrates towards one tiny pore of the channel surface. Cell tethers also grow out in cell 3 and correspondingly, cell 3 also migrates towards the same tiny pore along channel surface. The tethers are located in the left bottom of cell 2, but are located in the right site of cell 3.

Correspondingly, cell 2 migrate to the direction of bottom left, while cell 3 migrate to the right direction. Based in the relationship of migration routine and the location of the tethers, we can conclude that melanoma cell migrates to the same direction as the location of cell tethers inside biomimetic microvascular channel. There are less tethers on cell 2 as it is a little farer away from the tiny pore as shown in Fig. 7b~c. On the contrary, as it migrates closer and closer to the tiny pore, its tethers dramatically increase, as shown in Fig. 7d~f. As a result, migration velocity of cell 2 increases as time passes.

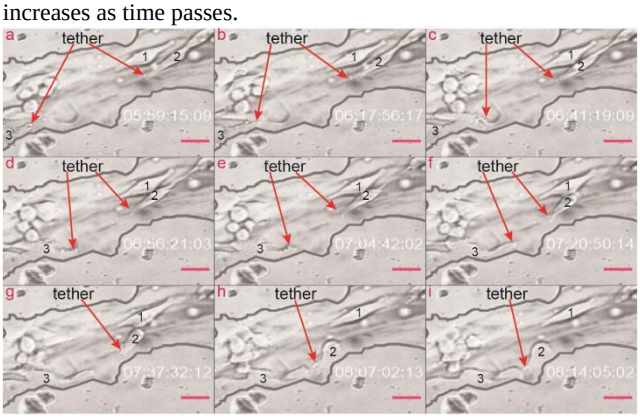

Fig. 7 Tethers' activation by cell motion. (a) ~ (i) Cell 2 and cell 3 migrate to the same direction as their tethers' location, while cell 1 doesn't migrate to any directions due to the lack of tethers. The red arrows indicate the formation of tethers. Time codes displayed in each frame indicate the time when the frame is captured. Scale bars, 50 μm.

Besides, cell tethers are dramatically activated in the locations closer to the tiny pores (Fig. 7g~i) than the locations farer away from the tiny pores (Fig. 7a~j). Because of such stimulating effect of microvascular pores on tethers formation, migration velocity of the two pores-activated cells (Cell 2 and cell 3) is much higher than observed overall daily migration velocity along the microvascular channel direction, as aforementioned in "section 3.2". Cell 3 reveal highest migration velocity within all the three cells in concern, since cell 3 always migrate along the biomimetic microvascular channel during the whole monitor period. Dramatically varied migration velocity of tumor cells inside biomimetic microvascular channel as illustrated in previous sections, can be reckoned to be virtually determined by the interaction between the tiny pores/tubes and the cell tethers.

3.4.3 Tethers' activation by cell division

It's also surprisingly found that, cell division can also activate the formation of tether inside biomimetic microvascular networks. Fig. 8 shows several daughter cells dividing from mother cells, noted as 1-1, 1-2; 2-1, 2-2; 3-1, 3-2; and 4-1, 4-2; respectively. Easily seen, all daughter cells have tethers grown out on the counterpart locations of cytomembrane along the cell body, as indicated by the red arrows. This can ensure the daughter cells can migrate into two contrary directions after division, to heighten the extravasation efficiency of tumor cells through microvasculature.

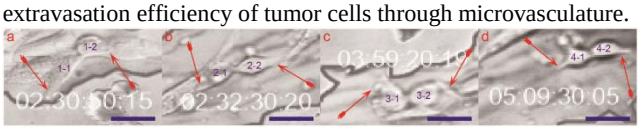

Fig. 8 Tethers' activation by cell division inside the microvascular channels. (a) ~ (d) Four pairs of daughter cells just divided from four different mother cells. The red arrows indicate the formation of tethers. Time codes displayed in each frame indicate the moment when the video begin to be recorded. Scale bars, 50 μm.

Cell 2 in Fig. 7 is the same cell as cell 2-1 in Fig. 8. Even if the original position of cell 2 is similar to cell 1 as shown in Fig. 7, cell 2 just divides from another cell, which is also one factor activating tether as illustrated here. As a result, cell 2 grows out more cell tethers than cell 1, and correspondingly displays for higher cell activity as shown in Fig. 7a~f. More details concerning related cells are also provided in the supplementary material (ESI 3).

3.5 Comprehensive cellular dynamic at single cell resolution

Through long-term monitor of cell dynamic inside biomimetic microvasculature followed by professional video processing, various cellular biophysical properties can be accurately analyzed at single cell resolution, including dynamic cytomembrane tension, extracellular communication, cell mobility, microvilli, and protonema configuration, etc.

3.5.1 Cytomembrane force

Cytomembrane dynamic interference between the cell and microchannel neck reveals a complicated and time-consuming process when tumor cell escapes from the microchamber into microvascular channel. The tumor cell may struggle several times to conquer the resistance force from microchannel, before it finally can extravasate into the microvascular channel. As shown in Fig. S2 (ESI 1), it takes two times of cytomembrane contractive motion and lasts for about one hour, before the concerned tumor cell finally extravasates into the microvascular channel. The cell has a stretched spindle shape originally, as shown in Fig. S2a~b. To escape from the channel neck, the cell membrane begins to contract, as shown in Fig. S2c~g. Nevertheless, this cell fail to escape from the tiny channel at the first time, and thus the cytomemebrane begins to extend, as shown in Fig. S2g~i. Afterwards, the cytomembrane contracts again (Fig. S2j~k). Finally this cell escapes from the tiny channel as shown in Fig. S2n. During this period, the prolonged cell tether brakes with the channel neck, which then becomes shorter and shorter, and finally merges with the cell membrane, as indicated by red arrows in Fig. S2j~n. Herein tether's braking force between the cytomembrane and the microchannel neck is calculated to be 35.5×10^{-12} *N* (ESI 1), based in a model Dai *et al* raised[54] known as phenomenological computing approach,[55] wherein the same human melanoma lines M2[54] as proposed here were systemically discussed.

3.5.2 Extracellular communication

Communication between metastatic tumor cells can also be accurately analyzed inside the biomimetic microvasculature. Fig. S3 (ESI 1) shows the extracellular communication between two tumor cells (indicated as cell A and cell B) within a period of seven hours. When cell A tries to pass through the tiny tube (Fig. S3a~b), there is a prolonged tether interconnected with cell B, as indicated by the red arrow. Through this interconnection, cell A and B build a communicational signal. As a result, after cell A passes through the tiny tube (Fig. S3c), it can't further move to upper location, but

is restricted in a small area for about three hours, as shown in Fig. S3c~f. In the meanwhile, this extracellular communication guide the cell B to migrate towards to the same tiny tube, as shown in Fig. S3d~g. From this phenomenon, we can conclude that tumor cells that already pass through the tiny tubes of microvascular networks can guide the following tumor cells to pass through the same tiny pores through such kind of extracellular communication, which can dramatically heighten the overall extravasation efficiency of tumor cells inside microvascular networks.

3.5.3 Protonemata configuration

Fig. S4 (ESI 1) shows the division details of two independent cells inside the biomimetic microvasculature. White intermediate filament firstly comes out in the center of the cell (Fig. S4b, j). After about ten minutes, the filament divides to two separate protonemata (Fig. S4c, k), and begin to move towards two counter-polar-positions of both cell bodies during the next four minutes (Fig. S4d, i, m). Finally, the protonemata totally move to the polar-positions with invaginated cytomembrane formed in the center of cell body, as shown in Fig. S4e, n. Independent cytomembrane comes out along the cellular nvagination during the next period taking around seven minutes (Fig. S4g, q), and finally separate one cell into two cells (Fig. S4h, r).

4 Conclusion

Herein we establish a method to fabricate biomimetic microfluidic microvasculature directly replicated from natural leaves, with desired microchambers integrated inside the networks. These microvascular networks allow for high-resolution and real-time observation of spatial-temporal single-cell dynamic, cell-cell communication, cell-microvasculature interactions and cell population property, etc. In contrast with existing in vitro "organ on chip model" or "LOC-based cell extravasation model", our model offers advantages in the following aspects: (1) the vessel like microvascular networks obeying Murray's law,[38~39] (2) professional video processing of real-time microscopic imaging for accurate characterization of single-cell biophysical properties, (cell deformation, cell migration, extracellular communication, cell division, and local shear stress of cytomembrane), (3) the verification of a "cell-tethers-mediated-mechanism" for cell deformation and migration inside the biomimetic vessel-like microvasculature model.

Human melanoma cells maintain dramatically high physiological activity after one week culture inside the biomimetic microchip, promising our model an ideal methodology for long term cell handing and analysis. We find that herein the biomimetic microvascular model can dramatically heighten tumor deformability but significantly labilize migration velocity, implicating mechanical stimuli enhanced cell adaption to microvasculature during transmigration. Through 72 hours assay of the cell migration inside one microchannel, the daily migration velocity can be calculated to be 83 μm/day, 338 μm/day, and 210 μm/day, respectively, indicating a velocity difference as much as four-times under same environmental condition. Compared with traditional systems, there are large amount of tiny-pores (outlets are closed) and tiny-tubes (outlets are open) located on the inner microvascular surface of biomimetic model here. We find that both the tiny-pores and the tiny-tubes can efficiently influence cell deformation, and decrease the overall cell migration velocity correspondingly. The difference is that for the case of tiny-pores, the cells always return back to the microchannel after they fail to migrate through; while for the case of tiny-tubes, the cells can migrate through, and even guide the following cells to motion towards the same tiny-tubes via extracellular communication. The physiological significance of this phenomenon is that the tumor cells can easily pass through any permeable tubes located on the vascular walls and thus invade to other organs, which can explain the high adjustability of tumor cells during their extravasation process through the *in vivo* microvascular systems.

Relying in professional video processing of cell activities, it's confirmed that large amounts of cell tethers grow out from the cytomembrane. These cell tethers are highly active and motional, just like the claws of some animals (e.g., actiniae) which extend out from their body and always try to grasp the signals from all directions around. Both the cell migration and the cell deformation occur in the same direction where cell tethers grow out. Furthermore, the tiny structures on the walls of biomimetic microvascular networks can efficiently stimulate the coming out of the cell tethers of the tumor cells, which finally explain the high cell deformability and unstable motion velocity during tumor metastasis, and thus, verifies the intrinsic enhanced accommodation of tumor cells to microvascular networks depends on extremely high tethers sensitivity to the mechanical stimuli from the tiny-structures on the microvascular wall, further revealing the "cell-tethers-mediated mechanism" as the reason for the hyperactive cellular biophysical behaviors inside biomimetic microvasculature. Tethers dynamic at single cell level is also quantified, with pore activated tether as long as 47 μm concerning two tumor cells during a monitor period of over eight hours.

One big difference between our system and other on-chip cell extravasation systems is that, there is no additional attractant reagent added in our system to form a chemical gradient all through the microvasculature. So the dynamic behavior of cells in our model are not initiated by cell chemotaxis, but initiated by the mechanical stimuli of the biomimetic microvascular network itself. The deformation and migration results implicate that, such kind of mechanical cell-stimulating cue is very strong, even comparable with chemotaxis stimuli. Depending on the video processing model raised here, we find the cell migration velocity can be activated as high as104.93 μm/h as cell position is very close to the tiny pores, more than 2.5 times of its average migration velocity farer to tiny pores. As a result, we evaluate the mechanical stimuli can play a comparable role as chemical cell-stimulating cue influencing tumor cell metastasis through folded microvascular channel like arteriosclerosis vessel, and thus may lead to new anticancer target for corresponding drug development.

Depending the original work as illustrated here, we evaluate wide range of research can be aroused, especially in the development of vessel-like microvascular networks for modeling functional microenvironmental equivalent and corresponding *in vitro* pathophysiological assays. Our method provides promising platforms to study cell division, proliferation, interactions, survival, migration, cytomembrane force, morphogenesis and differentiation under microvascular environments. Our future work includes the con-culture of different kinds of mammalian cells inside the multiple microchambers of the biomimetic system,

to achieve a "nature-inspired-microvasculature interconnected microfluidic organs-on-chip system" for further clinic and biomedical application.

Graphical abstract

It's verified by recent studies that, microvascular networks of leaf vein and animal vessel obey the same overall configuration rule: Murray's law. Inspired by this post, we innovate a biomimetic methodology to replicate veinal microvasculature from natural leaf into Lab-on-a-chip system, which can be further utilized as biomimetic animal vessel, as well as vessel-derived downstream applications.

Notes and references

1 A. Manz, N. Graber, H. Widmer, *Sens. Actuators B*. 1990, **1**, 244.
2 D. J. Harrison, K. Fluri, K. Seiler, Z. Fan, C. S. Effenhauser, A. Manz, *Science* 1993, **261**, 895.
3 M. U. Kopp, A. J. De Mello, A. Manz, *Science* 1998, **280**, 1046.
4 W. Wu, K. T. L. Trinh and N. Y. Lee, *RSC Adv.*, 2015, **5**, 12071.
5 P. S. Dittrich, A. Manz, *Nat Rev Drug Discov*. 2006, **5**, 210.
6 P. Neužil, S. Giselbrecht, K. Länge, T. J. Huang, A. Manz, N*at Rev Drug Discov*. 2012, **11**, 620.
7 E. Lucchetta, J. H. Lee, L. A. Fu, N. H. Patel, R. F. Ismagilov. *Nature* 2005, **434**, 1134.
9 M. Baker, *Nature* 2011, **471**, 661.
10 D. Huh, B. D. Matthews, A. Mammoto, M. Montoya-Zavala, *Science* 2010, **328**, 1662.
11 N. W. Choi, M. Cabodi, B. Held, J. P. Gleghorn, L. J. Bonassar, *Nat. Mater*. 2007, **6**, 908.
12 S. N. Bhatia, D. E. Ingber, *Nat. Biotech.* 2014, **32**, 760.
13 J. Ladewig, P. Koch, O. Brüstle, *Nat. Neuro.* 2014, **17**, 24.
14 Y. Luo, M. S. Shoichet, *Nat. Mater*. 2004, **3**, 249.
15 A. M. Skelley, O. Kirak, H. Suh, R. Jaenisch, J. Voldman, *Nat. Methods* 2009, **6**, 147. 16 Y. Shin, S. Han, J. S. Jeon, K. Yamamoto, I. K. Zervantonakis, *Nat. Protoc.* 2012, **7**, 1247.
17 G. M. Whitesides, *Nature* 2006, **442**, 368.
18 A. L. Fulton, D. J. Beebe, *Nature* 2014, **507**, 181.
19 X. Y. Wang, Y. Pei, M. Xie, Z. H. Jin, Y. S. Xiao, Y. Wang, *Lab Chip*. 2015, **15**, 1178.
20 A. Hasan, A. Paul, N. E. Vrana, X. Zhao, A. Memic, *Biomater*. 2014, **35**, 7308.
21 E. C. Novosel, C. Kleinhans, P. J. Kluger, *Advanced drug delivery reviews*, 2011, **63**, 300.
22 K. Schimek, M. Busek, S. Brincker, B. Groth, S. Hoffmann, *Lab Chip*. 2013, **13**, 3588.
23 W. Wu, J Wu, J. H. Kima and N. Y. Lee, *Lab Chip*, 2015, **15**, 2819-2825.
24 J. P. Morgan, P. F. Delnero, Y. Zheng, S. S. Verbridge, *Nat. Protoc.* 2013, **8**, 1820.
25 D. Huh, H. J. Kim, J. P. Fraser, D. E. Shea, M. Khan, *Nat. protoc.* 2013, **8**, 2135.
26 J. He, M. Mao, Y. Liu, J. Shao, Z. Jin, D. Li, *Advan. Health. Mater.* 2013, **2**, 1108.
27 H. J. Koo, O. D. Velev, *SCIENTIFIC REPORTS* 2013, **3**, 2357.
28 Q. Zhang, T. Liu, J. Qin, *Lab Chip*. 2012, **12**, 2837.
29 J. S. Miller, K. R. Stevens, M. T. Yang, B. M. Baker, *Nat. Mater.* 2012, **11**, 768.
30 W. Wu, K. T. L. Trinh and N. Y. Lee, *Analyst*, 2015, **140**, 1416.
31 W. Wu and N.Y. Lee, Sens. Actuators B, 2013, **181**, 756.
32 W. R. Hess, *Archiv für Anatomie und Physiologie: Physiologische Abtheilung* 1914, **1/2**, 1.
33 C. D. Murray, *Proc. Natl. Acad. Sci. USA*, 1926, **12**, 207.
34 C. D. Murray, *J. Gen. Physiol*. 1926, **9**, 835.
35 W. Wu, C. J. Hansen, A. M. Aragón, P. H. Geubelle, S. R. White, R. White, A. Lewis, *Soft Mat.* 2010, **6**, 739.
36 D. R. Emerson, K. Cieślicki, X. Gu, R. W. Barber, *Lab Chip*. 2006, 6, 447.37 R. W. Barber, K. Cieslicki, D. R. Emerson, *Design and Nature III: Comparing Design in Nature with Science and Engineering*, WIT Press, England 2006.
38 K. A. McCulloh, J. S. Sperry, F. R. Adler, *Nature* 2003, **421**, 939.
39 C. A. Price, S. J. C. Knox, T. J. Brodribb, *PLoS ONE* 2013, **8**, e85420.
40 W. Wu, R. M. Guijt, Y. E. Silina, M. Koch and A. Manz, *RSC Adv.*, 2016, **6**, DOI: RA-COM-12-2015-025890.
41 R. P. C. Wong, P. Ng, S. Dedhar, G. Li, *Molecular cancer therapeutics*, 2007, **6**, 1692.
42 A. F. Jerant, J. T. Johnson, C. Sheridan, T. J. Caffrey, *Am Fam Physician*. 2000, **62**, 357.
43 C. Zheng, Z. Yu, Y. Zhou, L. Tao, Y. Pang, T. Chen, *Lab Chip*. 2012, **12**, 3063.
44 M. Mehling, T. Frank, C. Albayrak, S. Tay, *Lab Chip*. 2015, **15**, 1276.
45 M. Chanasakulniyom, A. Glidle, J. M. Cooper, *Lab Chip*. 2015, **15**, 208.
46 N. Gopalakrishnan, R. Hannam, G. P. Casoni, D. Barriet, *Lab Chip*. 2015, **15**, 1481.
47 D. Gallego-Perez, N. Higuita-Castro, L. Denning, *Lab Chip*. 2012, **12**, 4424.
48 P. Sundd, E. Gutierrez, E. K. Koltsova, Y. Kuwano, *Nature* 2012, **488**, 399.
49 J. Diao, R. Liu, Y. Rong, M. Zhao, J. Zhang, Y. Lai, Q Zhou, *Nature* 2015, 563.
50 O. M. de Brito, L. Scorrano, *Nature* 2008, **456**, 605.
51 A. R. Houk, A. Jilkine, C. O. Mejean, R. Boltyanskiy, *Cell* 2012, **148**, 175.
52 K. Funamoto, I. K. Zervantonakis, Y. Liu, C. J. Ochs, C. Kim,

Lab on a Chip, 2012, **12**, 4855.
53 C. H. Yeh, S. H. Tsai, L. W. Wu, Y. C. Lin, *Lab chip*. 2011, **11**, 2583.
54 J. Dai, M. P. Sheetz, *Biophysical Journal* 1999, **77**, 3363.
55 S. A. Nowak, T. Chou, *Physical biology*, 2010, **7**, 026002.

4 Conclusions

In this thesis, we utilize three pumping systems: syringe pump (article 1, 2, 5), capillary pump (article 1) and diffusion pump (article 3 ~ 6) to transport liquid inside various microdevices. These pumps are successfully applied for different downstream applications, including POC diagnosis potential, microdroplet formation, multiphage flow, anticorrosive assay, impermeability confirmation, biomimetic self-pumped liquid transport of plant, Polymerase Chain Reaction, and medium injection for cellular dynamic monitor.

Compared with other external-power driven pumps requiring additional manufacture steps, e.g., electroosmotic Micropumps, magnetohydrodynamic (MHD) micropumps, electrokinetic micropumps, bubble' micropumps, electrophoresis micropumps, and piezoelectric pump, etc., syringe pump is one kind of ready-made commercial pump without any costly fabrication process. As a result, we firstly apply Syringe pump to transport fluidic inside different microdevices.

The first microdevice is Y-structure PDMS chip fabricated from multilayer-tape lithography, with a channel width of 500 μm and channel height of 150 μm. Through controlling flow rate of ink and oil at 50 μL/h and 250 μL/h, respectively, we find ink-droplets are successfully dispersed and formed inside continuous oil phage of the chip. But after the flow rate of ink and oil is adjusted to be 100 μL/h and 150 μL/h, respectively, multi-phase (oil-ink-oil) flow forms inside the chip. Thus we conclude syringe pump can be utilized for efficient multi-phase flow control inside microchannel containing grooved-shaped sidewall instead of smooth channel-wall. The second microdevice is PDMS–PVC microdevcie with a thick and short serpentine microchannel whose width, depth, and total length are 2 mm, 200 μm, and 115mm, respectively. It's well known that PDMS can change shape after contacted with small organic molecule like tetrahydrofuran (THF), leading to possible leakage if the bonding is not robust. To confirm the anticorrosion of PDMS–PVC to THF (colored with black for better visualization), syringe pump is used to transport THF to the microchannel at a flow rate of 1 mL/min for 25 min, and there is no leakage or swelling found during this period. Although noticeable swelling of PDMS takes place after THF is introduced into the microchip by syringe pump for up to 8h, still no leakage occurs, affirming syringe pump as an efficient approach for liquid injection in anticorrosive assay and leakage test. The third microdevice is novel 3D helical & rectangular silicone tube (0.3 mm ID/0.64 mm OD) microreactor, wherein the width, length, and height of are approximately 7.5, 19.2, and 6.5

mm, respectively. The total length of the silicone tube is 84 cm. Syringe pump is firstly utilized to transport mineral oil inside the microreactor at a rate of 10 μL/min. After oil is filled inside the whole microreactor, a 20μL PCR sample plug is introduced, followed by another plug of the mineral oil at 2 μL/min, making the sample plug completely encapsulated by the two plugs of the mineral oil. After the PCR sample flows out the microreactor, DNA (pGEM-3Zf + plasmid vector) is successfully amplified, affirming syringe pump as an efficient approach for stable liquid transport inside 3D device for PCR.

Although above studies confirm that syringe pump can be efficient access in fluidic control for wide range of downstream applications, nevertheless, size of pumping system is quite giant, much bigger than total size of microdevice, and thus, impossible to be integrated into the microdevice. Besides, external energy is required and consumed for supporting and maintaining its pumping power. As a result, syringe pump is inconvenient to transport liquid wherein portable and compact all-in-one microfluidic setup is an issue, conflicting with the concept of fabricating portable micro Total Analysis Systems (μTAS) for convenient operation.

In order to solve aforementioned defects of syringe pump, many groups have been developing self-activated pumping systems without any external-power consumption, displaying great advantages such as easiness of fabrication and integration. Of all these self-activated pumping systems, capillary-force-driven micropump is one most widely adopted type, and has been applied to many areas due to its successful solvability in the giant size problem of so-called “lab on a chip” systems for convenient and portable processing inside microfluidic.

As a result, we further analyze self-activated capillary pump for programmable velocity control that can be utilized for potential POC diagnosis. Through modifying microchannel-height of 2.5D microchip, it’s found the autonomous sample flow rate of 55 mm long microchannels are 0.1 μL/s, 0.21 μL/s and 0.39 μL/s when multilevel height are 200 μm, 300 μm, and 400 μm, respectively. After the microchannel height changes to 100 μm, 250 μm and 300 μm, the autonomous sample flow rate changed to 0.03 μL/s, 0.15 μL/s and 0.28 μL/s, correspondingly. Further mathematical modeling verifies that autonomous capillary flow rate increases as the multilevel microchannel of 2.5D microchip is heightened, in accordance with experimental results. So we conclude microchannel height can efficiently affect transport velocity of capillary pump for further POC diagnosis.

Nevertheless, although different self-powered micropumps have been introduced for autonomous liquid transport in vacuumized PDMS chip,[43] paper chip,[44] and capillary channel,[40-42] these pumps have fatal weaknesses that restrict them of wide applications. For example, all these self-powered micropumps have strict requirement on the consisting materials of microdevices, and can't be widely utilized to universal microfludic chips consisting of any material, like PTFE or PMMA. Besides, all of them are actually weak pumping systems. It's difficult for them to motivate sample flowing over long distance. The spontaneous capillary flow can also be easily interrupted by various barriers, such as gravity effect of 3D microdevice or high processing temperature inside microfluidic. For some reaction like micro continuous PCR, the required microchannel length is too long (over 2 meters) for these self-powered micropump to handle. Besides, denaturing temperature of polymerase chain reaction is 95 degree, also diffucult for them to motivate sample, and as a result, all aforementioned self-powered micropumps can only be applied to some limited areas.

In order to solve these defects, not only we analyze the performance of syringe pump and capillary pump for liquid transport as aforementioned, but also in the thesis here, we pay big attention in studying new kind of self-powered pump: the diffusion pump. Altogether four types of microdevcies (3D/2D microdevices of PDMS-glass/PDMS, PMMA-PMMA and silicone tube with obvious difference in microstructural topology) are fabricated to analyze the performance of diffusion pump in the thesis here.

The first microdevice is PMMA-PMMA microchip containing serpentine microchannel with original width, depth, and length set at 200 μm, 50 μm deep and 1.25 m for a total of 25 cycles (5cm length for each cycle). A thick-walled silicone tube (i.d. 0.2 mm, o.d. 2 mm) is inserted into the inlet port and thin walled silicone tube (i.d. 1 mm, o.d. 2 mm) is inserted into the outlet port, glued using PDMS prepolymer. Self-automated flow is analyzed by varying three parameters: the lengths of the outlet silicone tubes, the depth of the PMMA microchannel, and the total length of the microchannel. The total running times are 21, 31, and 50 min, respectively, which correspond to an average residence times of approximately 49, 72, and 119 s per cycle, respectively, when the lengths of the outlet silicone tubes are 3, 2, and 1 cm. When the width of the microchannel and the length of the outlet silicone tube are fixed at 200 μm and 3 cm, residence times of each cycle is measured to be 28, 49, and 63 s, respectively, if the depths of the microchannel were varied at 20, 50, and 100 μm, respectively. When the microchannel width, microchannel depth and the length of the

outlet silicone tube are 200, 80 μm, and 3 cm, respectively, the average residence times are measured approximately 49, 48, and 53 s, respectively, if the total channel lengths of microchannel is 1.25 m (25 cycles), 2.25 m (45 cycles), and 2.75 m (55 cycles). Further mathematical modeling verifies that autonomous flow rate increases as the lengths of the outlet silicon tubes increase, decreases as the microchannel width/height increases, but of no obvious relationship with microchannel length, in accordance with experimental results, approving that appropriate flow rate can be gained by adjusting these three parameters. The second microdevice is seamless 3D helical & trapezoidal silicone tube (0.51 mm ID/0.94 mm OD) microreactor, wherein the length and height are approximately 28.2 and 7.0 mm, respectively. The widths of the microreactor closer to the inlet and the outlet are 25 and 10 mm, respectively. The total length of the silicone tube is 1.5 m. Diffusion pump is utilized for self-automated sample flow through this microreactor, without the usage of mineral oil that's inevitable when using aforementioned syringe pump. The successful amplification result affirm diffusion pump as an endurable approach for liquid transport inside 3D device, while efficiently suppressing air bubbles under high temperature as well.

Aforementioned two microdevices have similar microstructural topology: one-directional segmented-linear microchannel connecting only one inlet and one outlet. In contrast, the next two microdevices are leaf-inspired microchips consisted of very complicated microvascular networks interconnecting multiple inlets and outlets, of obvious difference in microstructural topology with previous microsystems.

The third microdevice is leaf-inspired PDMS chip with whole ordered microvascular network. Altogether three kinds inspired biomimetic microchips with whole ordered micronetwork replicated from Tilia platyphyllos, Aegopodium podagraia and Carpinus betulus, are utilized flow self-automated flow analysis. The biomimetic microchip from Carpinus betulus has 2-order microvascular bifurcating structures, with one 4.7 cm long first-ordered microchannel and sixteen parallel second-ordered micochannels. The average flowing rate in first-ordered microchannel and second-ordered microchannel are measured to be 0.00357 cm/sec and 0.00745 cm/sec, respectively. The biomimetic microchip from Aegopodium podagraia has 2-order microvascular bifurcating structures. Noticeably, the first-ordered microchannel in the center of PDMS leaf is 4.3 cm in length, much longer than another four first-ordered microchannels with average length of 2.5 cm. The flow rate of five first ordered microchannel is measured to be 0.0153 cm/sec, 0.0161 cm/sec, 0.0148 cm/sec, 0.0164 cm/sec and 0.0156 cm/sec, respectively. Average flow rate of second-

ordered microchannels is calculated to be 0.0109 cm/sec. The biomimetic microchip from Tilia platyphyllos has 3-order microvascular bifurcating structures. The first-ordered microchannel in the center of PDMS leaf is 4.2 cm in length, while average length of other first-ordered microchannels is 2.55 cm. The average flow rate in all first-ordered microchannels is calculated to be 0.0447 cm/sec; and the average flow rate in second-ordered microchannels is calculated to be 0.0222 cm/sec. It's also surprisingly found here, the self-powered flow in leaf-inspired microvascular channel obeys sorptivity rule, which is mostly found in capillary absorption. The fourth microdevice is one leaf-inspired PDMS chip from Tilia platyphyllos, but additional artificial microchambers are integrated into the whole ordered microvascular network for potential biomedical engineering. Through diffusion pumps, cell culture medium is successfully injected into the whole microvasculature, qualified for long term cell culture. Because of the complicated microchannel structure, air bubbles may easily form if other pumps are utilized. But the diffusion pump can push away all air bubbles formed during the injection step, and thus, the medium can fill in whole microvasculature.

In contrast with self-powered autonomous flow inside simple topological microstructure connecting one inlet and one outlet, self-powered flowing performance through PDMS leaves is much more complicated due to two reasons. Firstly, it's found that surface of microchannel replicated from leaves is very rough, because microcosmic structure such as stomata, dytoderm and micropillars in natural leaves are all replicated to PDMS replica. Besides, PDMS leaves are consisted of complex microvascular networks interconnecting multiple inlets and outlets, which is much more complicated in geometrical topology than aforementioned microdevices wherein only one inlet and one outlet is connected by single-directional segmented microchannel. But diffusion micropump also displays excellent performance for liquid transport inside various PDMS microchips fabricated from real leaves. Self-powered flow inside PDMS leaves and real leaves share similar properties. Firstly, overall geometry of microvascular networks wherein self-powered flow occurs are the same in real leaf and PDMS leaf. Secondly, self-powered flow are activated by gas molecules' diffusion in both leaves: in real leaf it is vapor-molecules' diffusion from leaf into atmosphere; while in PDMS leaf it is air-molecules' diffusion from leaf into atmosphere. Thirdly, the hydrodynamic potential at the posterior end of real leaf and PDMS leaf are reckoned to be constant, but the hydrodynamic potential at real & PDMS leaves are

reckoned to be reduced because gas-molecules' diffusion is reckoned to happen only in real & PDMS leaves but negligible in stipe and syringe.

Our main purpose is to analyze the hydraulic flow throughout all bifurcating channels ranging from highest to lowest ordered networks which is the same as real leaves, as well as how overall leaf-inspired microvasculature influence gas-diffusion. As a result, we only explore whole-ordered veinal network to analyze how microvascular networks interfere self-powered flow, while ignoring subset morphology such as xylem, phloem, cellular exoskeleton and chlorenchyma in real leaves, etc. Average flow rate through first-ordered microchannels and second-ordered microchannels are calculated to be 0.00745 cm/sec and 0.00357 cm/sec in Carpinus betulus replicated PDMS leaf, 0.0157 cm/sec and 0.0109 cm/sec in Aegopodium podagraia replicated PDMS leaf, and 0.0447 cm/sec and 0.0222 cm/sec in Tilia platyphyllos replicated PDMS leaf. So average flow rate in first-ordered microchannels is 2.08, 1.43, and 2.17 times of second ordered microchannels for biomimetic microchips replicated from Carpinus betulus, Tilia platyphyllos and Aegopodium podagraia, respectively. As a result, we can conclude overall geometrical microvascular configuration in leaves displays higher hydraulic conductivity in first ordered microchannels than second-ordered microchannels, to ensure higher water transport capacity in higher-ordered microchannels than lower-ordered microchannels. The realization of self-powered autonomous flow inside PDMS leaves (cross-linked microvascular networks interconnecting multiple inlets and outlets) not only can widen the applicant range of such self-powered diffusion micropump from one-dimensional microchannel to multi-dimensional microvasculature, but also can heighten our understanding on how natural microvascular configuration regulates self-powered flow that's widely exist in all natural leaves.

From aforementioned discussion, we can see syringe pump can accurately control flow rate in different microdevcies, but it's too giant in size and indispensable to external-energy supply as well. Capillary pump can transport fluidic free of power consumption, but can only be applied to limited microdevices. Diffusion micropump doesn't require any fabrication step when applied for liquid transport inside microdevice, making the final micro-device so portable that matches well with the microchip's disposable concept for various downstream applications. Through systemic flowing analysis inside different microdevices, it's verified that diffusion micropump not only can provide stable flow over long distance, but also can easily (just by changing the microdevice's dimension and

operational parameter) provide much wider range of flow rate than existed self-powered micropumps, like capillary pump. When we apply diffusion micropump for micro continuous PCR inside PMMA chip, it verifies diffusion pump can automate stable flow through long channel over 2 meters and endure high denaturing temperature of 95 degrees. Not like other self-powered micropumps, the usage of diffusion micropump to PMMA chip promises it can be applied to any materials (PTFE, PC, PET, etc) without limitations. We also make comparison between diffusion micropump and traditional syringe pump in their performance, which also reveals diffusion micropump has better performance in high temperature: when using syringe pump, a lot of bubbles come out from the microchannel, which even totally break the liquid flow; however, when using diffusion micropump, few bubbles come out from the device. Because the flow is so stable without any microbubbles' formation, the PCR amplification is highly efficient here.

In brief summary, the technological development during last ten years has made it quite cheap, easy and quick to fabricate microdevice nowadays. As a result, the concept of disposable microchip for clinical detection, biological analysis, and disease diagnosis, etc., has become possible and been more and more valued. But disposable microdevices should be supported by other accessories to finally realize their applicant function. Necessary accessories always include micropumps, microheaters, microvalves or micromixers, etc. Only in the case when the disposable microdevice matches well with its accessories can the disposable microdevice realizes its most valuable significance. In other words, not only the easily fabricated microdevice should be cheap or disposable, its accessories (i.e., various kinds of micropumps such as electroosmotic micropumps, magnetohydrodynamic micropumps, electrokinetic micropumps, electrophoresis micropumps, etc.) should also be easily fabricated, cheap, portable and even disposable. Form this viewpoint, diffusion pump may play important role as self-integrated micropump for liquid transport inside microchip.

5 References

(1) Van Lintel HTG, van de Pol FCM, Bouwstra S. Sens Actuators. 1988, 15, 153–167.
(2) Smits JG. Sens Actuators A 1990, 21-23, 203–206.
(3) Wu, W.; Trinh, K. T. L.; Lee, N. Y. Analyst. 2012, 136, 2069-2076.
(4) Wu, W.; Kang, K.-T.; Lee, N. Y. Analyst. 2011, 136, 2287-2293.
(5) Wu, W.; Lee, N. Y. Anal. Bioanal. Chem. 2011, 400, 2053-2060.
(6) Liu J, Enzelberger M, Quake S. Eletrophoresis. 2002, 23, 1531 –1536.
(7) Yang, M.; Sun, S.; Bruck, H.; Kostov Y.; Rasooly, A. Lab Chip. 2010, 10, 2534-2540.
(8) Johnston, I.D.; Tracey, M.C.; Davis, J.B.; Tan, C.K.L. J. Micromech. Microeng. 2005, 15, 1831–1839.
(9) Johnston, I.D.; Tracey, M.C.; Davis, J.B.; Tan, C.K.L. Lab Chip. 2005, 5, 318–325.
(10) Prakash, R.; Kaler, K. Microfluid Nanofluid. 2007, 3, 177–87.
(11) Wang, S.S., Huang, X.Y., Yang, C. Microfluid. Nanofluid. 2010, 8, 549–555.
(12) Laser DJ, Santiago JG. Micromechanics Microengineering. 2004, 14, 35–64.
(13) Unger, M.A.; Chou, H-P; Thorsen, T.; Scherer, A.; Quake, SR. Science. 2000, 288, 113–116.
(14) Kim, J.; Baek, J.; Lee, K.; Park, Y.; Sun, K.; Lee, T.; Lee, S. Lab Chip. 2006, 6, 1091–1094.
(15) Lai, H.; Folch, A. Lab Chip. 2011, 11, 336–342.
(16) Futai, N.; Gu, W.; Takayama, S. Adv. Mater. 2004, 16, 1320–1323.
(17) McKnight, T.E.; Culbertson, C.T.; Jacobson, S.C.; Ramsey, J.M. Anal. Chem. 2001, 73, 4045–4049.
(18) Debesset, S.; Hayden, C.J.; Dalton, C.; Eijkel, J.C.; Manz, A. Lab Chip. 2004, 4, 396–400.
(19) García-Sánchez, P.； Ramos, A.; Green, N. G.; Morgan， H. Langmuir. 2008, 24, 9361–9369.
(20) Yuan, Q.; Wu , J. Biomedical Microdevices. 2013, 15, 125–133.
(21) Gagnon, Z.; Mazur, J.; Chang, H. C. Lab Chip. 2010, 10, 718–726.
(22) Bowen, A. L.; Martin. R. S. Electrophoresis. 2010, 31, 2534–2540.
(23) Karlinsey, J. M. Analytica Chimica Acta. 2012. 725, 1–13.
(24) Lopes, F. S.; Coelho, H. G.; Gutz, I. G. Electrophoresis. 2011, 32, 939–946.
(25) Pollack, M.G.; Fair, R.B.; Shenderov, A.D. Appl. Phys. Lett. 2000, 77, 1725-1726.
(26) Chatterjee, D.; Amiroudine, S. Biomed Microdevices. 2011, 13, 147–157.
(27) Rivero, M.; Cuevas, S. Sensors and Actuators B. 2012, 167, 884– 892.
(28) Weston, M. C.; Gerner, M. D.; Fritsch, I. Anal. Chem. 2010, 82, 3411–3418
(29) Pitchaimai, K.; Sapp, B. C.; Winter, A.; Gispanski, A.; Nishida T.; Fan, Z. H. Lab Chip. 2009, 9, 3082–3087.
(30) Liu, RH.; Yang, J.; Lenigk, R.; Bonanno, J.; Grodzinski, P. Anal Chem. 2004, 76, 1824–1831.
(31) Naito, T.; Arayanarakool, R.; Gac, S.; Yasui, L. T.; Kaji, N.; Tokeshi, M.; Berg, A.; Baba, Yoshinobu. Lab Chip. 2013, 13, 452–458.
(32) Chan, S. C.; Liu, C. H. Sens Actuators A. 2010, 163, 501–509.
(33) Lui, C.; Stelick, S.; Cady, N.; Batt, C. Lab Chip. 2010, 10, 74–79.
(34) Chiu, S.H.; Liu, C. H. Lab Chip. 2009, 9, 1524–1533.
(35) Bohm, S.; Timmer, B.; Olthuis, W.; Bergveld, P. J. Micromech. Microeng. 2000, 10, 498–504.
(36) Nguyen, N. T. Microfluidics and Nanofluidics. 2012, 12, 1–16.
(37) Assadsangabi, B.; Mohamed Ali M.S.; Takahata, K. Sensors and Actuators A. 2012,173, 219–226.

(38) Dijkink, R.J.; van der Dennen, J.P.; Ohl, C.D.; Prosperetti, A. J. Micromech. Microeng. 2006, 16, 1653–1659.
(39) Tovar, A.R.; Lee, A.P. Lab Chip. 2009, 9, 41–43.
(40) Chakraborty S. Lab Chip. 2005, 5, 421–430.
(41) Münchow, G.; Dadic, D.; Doffing, F.; Hardt, S.; Drese, K. S. Expert Rev Mol Diagn. 2005, 5, 613–620.
(42) Ren, H.; Xu, S.; Wu, S.T. Lab Chip. 2013, 13, 100–105.
(43) Dimov, I.K. ; Desmonts, L.; Garcia-Cordero, B. J. L.; Ross, B. M.; Ricco, A. J. ; Lee, L. P. Lab Chip, 2011, 11, 845–850.
(44) Kauffman, P.; Fu, E.; Lutz, B.; Yager, P. Lab Chip. 2010, 10, 2614-2617.
(45) Whitesides, G. M. Lab Chip, 2013, 13, 11-13.
(46) Whitesides, G. M. NATURE, 2006, 442, 368–373.
(47) Gamboa A.R.; Morris C.J.; Forster, F. Proc. ASME Int. Mechanical Engineering Congress and Exposition (Washington, DC). 2003.
(48) Wu, W.; Trinh, K. T. L.; Lee, N. Y. Analyst, 2012, 137, 4, 983-990.
(49) Wu, W.; Lee, N. Y. Sensors and Actuators B: Chemical, 2013, 181, 756– 765.
(50) Canny, M. American Scientist, 1998, 86, 152-159.
(51) Wheeler, T.D. and Stroock, A.D., Nature, 2008, 455, 208-212.

Wenming Wu

Background: Chemistry, Chemical engineering, Biomimetic, Biochemistry, Lab on a chip, Nano engineering, Cellular engineering, Molecular biology, Microorganism

Area: Microfluidic, Polymerase Chain Reaction, Monocyte/Macrophage, Silane coupling reagent, Tumor migration, Capillary electrophoresis, 2.5D & 3D Micro-manufacture methodology, Organ on a chip, Drug screening, Endothelium vascularization, Optical imaging, Self-powered sample transport

EDUCATION & Working Experience:

- **2014. 03 ~ now:** Mechatronics department, University of Saarland, Germany. Researcher & PhD
- **2013. 11 ~ now:** Korea Institute of Science and Technology Europe. Researcher (Employee)
- **2012. 09 ~ 2013. 09:** College of BioNano Technology, Gachon University, Korea. Postgraduate Researcher
- **2012. 09 ~ 2013. 06:** Bioconvergence research center, Seoul National University. Full-time Researcher
- **2011. 10 ~ 2012. 09:** Gachon Bionano Research Institute (GBRI), Korea. Researcher (Employee)
- **2010. 10 ~ 2011. 10:** Korea Research Institute of Bioscience and Biotechnology. Researcher (Employee)
- **2008. 10 ~ 2010. 10:** College of Bionanotechnology, Kyungwon University, Korea. Master degree of engineering
- **2003. 08 ~ 2008. 07:** College of chemistry and chemical engineering, Shandong University, China. Bachelor degree of engineering (Parallel First Bachelor Degrees)
- **2003. 08 ~ 2008. 07:** College of chemistry and chemical engineering, Shandong University, China. Bachelor degree of Science (Parallel First Bachelor Degrees)

Special Training Experience：

- **30. 01. 2015:** Training on micro-technological industrialization, Agilent Company (Europe)
- **07. 2012 - 08. 2012:** Intensified training on Pneumatic Micro-pump Technique, Bio-matrix group of Ewha Women University, Korea
- **11. 07. 2011 - 16. 07. 2011:** Intensified training on comprehensive Biological Technique, Korea Research Institute of Bioscience and Biotechnology (KRIBB), Korea
- **06. 2008 - 07. 2008:** Intensified training on organic synthesis, “school of chemical biology & biotechnology” of Peking University, China

Current Contact Information

Office Tel: +49-(0)681 / 9382 - 227
Fax: +49-(0)681 / 9382 – 240

KIST Europe
Campus E 7 1
D-66123 Saarbruecken
Germany